Prospects of Observing Gravitational Lensing of Continuous Gravitational Waves

A Thesis

Submitted to the

Tata Institute of Fundamental Research, Mumbai

for the degree of Doctor of Philosophy

in Subject Board of Physics

by

Aditya Kumar Sharma

International Centre for Theoretical Sciences

Tata Institute of Fundamental Research

Bengaluru 560089, India
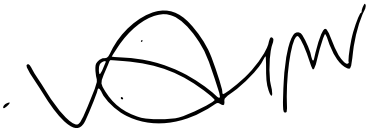
July 2025

Declaration

This thesis is a presentation of my original research work. Wherever contributions of others are involved, every effort is made to indicate this clearly, with due reference to the literature, and acknowledgment of collaborative research and discussions. The work was done under the guidance of Professor Parameswaran Ajith at the International Centre for Theoretical Sciences, Tata Institute of Fundamental Research (ICTS-TIFR), Bangalore.

22 July 2025

Aditya Kumar Sharma

In my capacity as the formal supervisor of the record of the candidate's thesis, I certify that the above statements are true to the best of my knowledge.

22 July 2025

Parameswaran Ajith

Acknowledgments

Of all the days LIGO could have chosen to announce the discovery of gravitational waves, it chose February 11, 2016 — my birthday! So let me begin by thanking LIGO. As a first year undergraduate student, I remember coming across several news articles writing about this elusive thing scientists had finally discovered. Back then, I had no idea I'd one day end up being so connected to this very "elusive" thing. Thanks to the wonderful people I met during my PhD journey, I did. The list is long, but it definitely begins with my advisor, Ajith. I cannot thank him enough for being so incredibly patient with me throughout these years, and more importantly for being an amazing human being. Right from the first day when I went to his office and he told me about this "cocktail of gravitational waves", to my final day packing up at ICTS, Ajith has been nothing but kind and supportive. So, thank you, Ajith!

I consider myself incredibly fortunate to have been a part of the Astrophysical Relativity group at ICTS. It is hard to overstate the importance of the role each and every member of the group has played in my journey. The mentorship I received from the senior members when I joined the group deserves a special mention. I'm to grateful to Ajit Mehta, Gayathri, Rahul, Haris, Sumit, Shasvath, and Apratim for all their guidance when I was a toddler. I'm also thankful to my fellow AstroRel graduate students for creating a scientifically stimulating and fun environment — Soummyadip, Aditya Vijaykumar, Srashti, Uddeepta, Mukesh, Souvik, Ankur, Kaustubh, Akash Maurya, Alorika, Chandru, Vinay, Santhiya, and Irshad. Thanks for all the engaging discussions over lunch, meetings, and lunch meetings. I speak for the group when I say Bala has been an inspiration to all of us. Thank you, Bala, for your calming presence in all our group meetings, and for your encouraging words. I also want to thank Prayush for all the useful insights he provided whenever I turned up to him with questions.

Along my academic journey, I have had the opportunity to collaborate with many exceptional individuals. I am immensely thankful to all my scientific collaborators — Soummyadip Basak, Shasvath J. Kapadia, Gopalkrishna Prabhu, R Prasad, Otto Hannuksela, Samson Leong, Justin Janquart, Paul Martens, Rodrigo Tenorio, David Keitel, Alicia Sintes, Alicia Calafat, Karl Wette — and, of course Ajith. Although, we haven't formally collaborated on any projects, one person I've especially enjoyed discussing gravitational waves, and life in general, with is Aditya Vijaykumar. Thanks a lot, Vee — you're an absolute gem.

I am truly grateful to Alicia Sintes and David Keitel for hosting me at the University of the Balearic Islands in 2022, and for the many intriguing conversations on continuous waves. I acknowledge the TIFR-Leading Edge Travel Grant for funding this visit. I also thank Rodrigo Tenorio for all his help with continuous wave tools. I have also benefited incredibly from engaging in discussions with the LIGO collaboration members. I want to thank everyone in this wonderful collaboration for sharing so many insights on gravitational waves, whether over weekly calls or through email conversations.

I'm also indebted to the Australian National University for the ANU-FRT grant, which gave me the opportunity to spend three months at the Centre for Gravitational Astrophysics. Working with Bram and Lilli, and learning about gravitational wave detectors from them, was a remarkable experience. I thank them — and the entire CGA group — for their warmth, and for making my stay there enjoyable. I thank Jay Poria for going out of his way to ensure my stay in Canberra was comfortable, and for making the trip to Sydney incredibly fun.

ICTS has become a memorable part of my life, thanks to the many wonderful individuals I have had the fortune of meeting there. Showing up at ICTS was a joy everyday because of these friends — Junaid, Divya, Omkar, Tuneer, Srashti, Vee, Saikat, Jitu, Chandra, Saurav, Saumav, Basu, Priyadarshi — thank you all so much. To my fierce rivals on the badminton court and the football ground — Mahaveer, Basu, Saikat, Sugan, Nirnoy, Anup, Uddeepta, Bhanu, Rahul, Pushkal, Ganga, Mukesh, Chandan — thanks for all the camaraderie, and yes, even the occasional heated moments. I want to thank my seniors — Rahul, Mukesh, Pushkal, Ganga, Sumith, and Chandan — who made me feel at home in my first year at ICTS. I reserve special thanks for some people who I have connected on

a very personal level over these years. Thanks Rahul for turning from a senior to a very dear friend. Thanks Siddhartha, for the many dinners and the many shayari sessions at your place. I look forward to more of them. You are by far the most talented yet humble person I have met. A special thanks again to Vee, but this time on a more personal note. Talking to you has always helped in moments of self doubt. Also, thanks for patiently bearing with my rants, and engaging in all the gossips. And thanks to Rahul, Siddhartha and Vee collectively for the phenomenon called Jashn-e-rivaz. Thanks Divya, Junaid, Jitu, Srashti, and Omkar for being my go-to people whenever I needed to talk. Thanks also to my friends from undergrad who kept in touch over these years, and often dropped a text asking, "How are you?". Especially thanks Ida for always being there — whether over a call or texts — and for patiently listening to me whine about anything and everything.

I thank the administrative and technical staff at ICTS who work tirelessly behind the scenes to ensure flawless operations in the institute. I'm especially thankful to Madhulika, Basavaraj, Suresh, Jeeva, Veena, Nidhi, Ramya, Sunitha, Raju, Prashanth for their exceptional support, often going above and beyond to help out. I thank Hemanth, Irshad, and Srinivas for taking care of the computational facilities. I'm also very thankful to the cafeteria staff — Balaji, Prasanna, Naga.

This next vote of thanks is the most important one in this acknowledgment. My academic journey has been made possible because of the countless sacrifices made by my mother, Sudha, over the years. Being raised by her and three elder sisters has shaped my outlook on life. I don't know the right adjective to express my gratitude to them, but a mere "thank you" feels hopelessly inadequate. Maa, I consider myself blessed to be your son. To my sisters — Jaya, Andri, and Aparna — thank you for always loving and supporting me. This thesis, written in the memory of my beloved father, is dedicated to Maa.

List of Figures

11

List of Tables

Contents

Abstract

The observation of gravitational waves from the merger of two black holes by the Advanced LIGO detector in 2015 was a groundbreaking validation of Einstein's theory of General Relativity. Since then, the LIGO-Virgo-KAGRA collaboration has detected several such compact binary coalescence events. Beyond these transient sources, other gravitational wave candidates also hold significant astrophysical potential. Among the most promising are spinning, non-axisymmetric neutron stars in our Galaxy, which emit long-lived, nearly monochromatic gravitational waves. Some of these neutron stars may reside behind the galactic supermassive black hole, Sgr A*, resulting in strong gravitational lensing of their continuous waves. Using various astrophysically motivated spatial distributions for the Galactic neutron stars, we assess the probability of such lensing events. Furthermore, we study the detectability of such lensed continuous gravitational waves with third-generation detectors. These detections can serve as novel probes of the Galactic Center's properties, including independent measurement of the mass of Sgr A*. We demonstrate how future observations of lensed continuous waves can be used to infer the mass of Sgr A*, and estimate the precision of this measurement. Under favorable conditions, we find that this method can be at par with the current electromagnetic observation measurements.

Chapter 1

Introduction

1.1 Gravitational Waves

For centuries, gravitation was understood to be a force between masses, governed by Newton's inverse-square law of gravitation. A major perspective change occurred with Einstein's theory of General Relativity (GR) in 1915, which depicted gravitation as the curvature of spacetime caused by the concentration of mass and energy [11]. In the Einstein formalism, the spacetime geometry was described by the field equations:

$$R_{\mu\nu} - \frac{1}{2}R\,g_{\mu\nu} = \frac{8\pi G_N}{c^4}T_{\mu\nu}. \tag{1.1}$$

Here, $R_{\mu\nu}$ and R are the Ricci tensor and Ricci scalar constructed out of the metric $g_{\mu\nu}$ [1] and describe the curvature of the spacetime. G_N, c are the Gravitational constant and speed of light respectively. The stress energy tensor, $T_{\mu\nu}$, as evident from eqn 1.1, determine the spacetime curvature encapsulating how matter and energy effect geometry. To famously quote John Wheeler describing these equations, *"Space-time tells matter how to move; matter tells space-time how to curve"*.

This paradigm shift wasn't merely theoretical, but had major observational implications right from the outset. Einstein had himself proposed a few practical tests of his theory in subsequent works. For example, GR could explain the anomalous perihelion precession of Mercury's orbit [12, 13], accounting for an excess orbital precession of 43 arcseconds per century previously observed [14, 15]. Additionally, Einstein had accurately predicted

---

[1]and their derivatives.

the apparent shift in star's position behind the sun to be twice than that of Newton's estimation. It was soon confirmed by Eddington during the solar eclipse of 1919 [16]. The gravitational redshifting of light, a corollary of GR's principle of equivalence, was experimentally demonstrated by Pound and Rebka Jr. in 1959 by measuring the frequency variation of gamma rays due to Earth's gravitational field [17, 18].

1.1.1 Linearizing Einstein Field Equations

Another major prediction of GR was the existence of gravitational waves (GWs) – ripples in spacetime caused by time-varying quadrupole and higher moments of the matter distribution [19]. A straightforward understanding of emergence of GWs in GR can be drawn from linearizing the Einstein field equations around a Minkowskian (flat) metric:

$$g_{\mu\nu} \equiv \eta_{\mu\nu} + h_{\mu\nu}, \quad \text{where} \quad |h_{\mu\nu}| \ll 1. \tag{1.2}$$

For 4-dimensional spacetime, the symmetric metric perturbation, $h_{\mu\nu}$, has 10 independent components. Since GR is invariant under diffeomorphic transformations, this allows us to reduce these degrees of freedom by 4 with a suitable gauge choice, akin to a choice of coordinates.

Constructing the Ricci tensor and scalar out of the metric to linear order in $h_{\mu\nu}$ in the Lorentz gauge [2], and plugging it in the Einstein equations yields:

$$\Box \bar{h}_{\mu\nu} = -\frac{16\pi G_N}{c^4} T_{\mu\nu}, \tag{1.3}$$

where $h = \eta^{\mu\nu} h_{\mu\nu}$ denotes the trace, $\bar{h}_{\mu\nu} = h_{\mu\nu} - \frac{1}{2}\eta_{\mu\nu}h$ is the trace reversed metric and $\Box \equiv -\frac{1}{c^2}\partial_t^2 + \nabla^2$ is the d'Alembertian operator.

1.1.2 Vacuum Solutions and Transverse-Traceless Gauge

To study the propagation of metric perturbations away from the sources, we use $T_{\mu\nu} = 0$, reducing equation (1.3) to:

$$\Box \bar{h}_{\mu\nu} = 0. \tag{1.4}$$

---

[2]The gauge choice used here is $\partial_\mu \bar{h}^{\mu\nu} = 0$. Since these are four constraints put on the 10 independent components of the symmetric metric, $h_{\mu\nu}$, in Lorentz gauge, the metric has only 6 independent degrees of freedom. We refer the reader to sections 1.2 to 1.4 of [20] for the complete derivation.

Here, one can further gauge fix 4 residual degrees of freedom corresponding with choice, $x^\mu \to x^\mu + \xi^\mu$, as long as $\Box \xi^\mu = 0$. Exploiting this, we can set the trace of $h_{\mu\nu}$ i.e. $h = 0$, also implying $\bar{h}_{\mu\nu} = h_{\mu\nu}$, and $h_{0i} = 0$ where $i = 1, 2, 3$ are the spatial indices. The Lorentz gauge condition, $\partial_\mu \bar{h}^{\mu\nu} = 0$, along with $h_{0i} = 0$ gives $\partial_0 h_{00} = 0$. Since we are only interested in the time-dependent part when dealing with GWs, we can just set h_{00} to 0. This choice is called the transverse traceless (TT) gauge. In summary, the gauge freedom in GR allows the choice of $h_{0\mu} = 0$ and $\partial_i h_{ij} = 0$. The equation of motion for $h_{\mu\nu}^{TT}$ in the TT gauge then is:

$$\Box h_{\mu\nu}^{TT} = 0, \tag{1.5}$$

where $h_{\mu\nu}^{TT}$ has only two independent degrees of freedom as described above. This is the familiar wave equation. Its solutions, GWs, can be written as plane waves or a superposition of plane waves of different frequencies traveling at the speed of light:

$$h_{ij}^{TT} = A_{ij} e^{i(\mathbf{k}.\mathbf{x} - \omega t/c)}. \tag{1.6}$$

Here, $\mathbf{k} \equiv |\mathbf{k}|\hat{n}$ is the wave-vector, $\mathbf{x}$ is the position vector, $\omega = c|\mathbf{k}|$ is the angular frequency, and $\hat{n}$ denotes the direction of propagation. The gauge choice, $\partial_i h_{ij} = 0$, for plane waves implies $\hat{n}_i A_{ij} e^{i(\mathbf{k}.\mathbf{x} - \omega t/c)} = 0$, revealing the transverse nature of GWs. For the propagation along a definite z-direction, the metric solutions take the symmetric tracefree form:

$$h(t) = \begin{pmatrix} h_+ & h_\times & 0 \\ h_\times & -h_+ & 0 \\ 0 & 0 & 0 \end{pmatrix} \cos(\omega(t - z/c)). \tag{1.7}$$

The two degrees of freedom, h_+ and $h_\times$, are called the "plus" and the "cross" polarisations respectively. As these are transverse metric perturbations to spacetime, they cause stretching and squeezing of proper distances along the orthogonal directions to the direction of propagation.

For example, let us consider two test particles at $(t, 0, 0, 0)$ and $(t, L, 0, 0)$. For a + polarized GW along the z-direction, the proper distance between the two events, D_{xx}, to
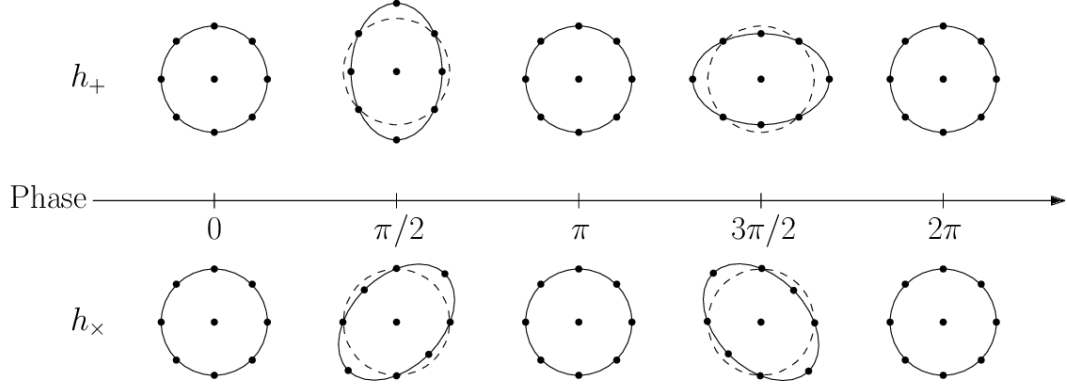
Figure 1.1: Effect of GW polarisations on a ring of test particles (exaggerated). Figure taken from [1].

linear order in $|h_+|$ is:

$$
\begin{aligned}
D_{xx} &= \int_0^L dx \sqrt{g_{11}} \\
&= \sqrt{1 + h_+ \cos(\omega t)} \int_0^L dx \\
&= L(1 + \frac{h_+}{2} \cos(\omega t)).
\end{aligned}
\tag{1.8}
$$

Similarly, along the y-direction, the proper distance is:

$$
D_{yy} = L(1 - \frac{h_+}{2} \cos(\omega t)).
\tag{1.9}
$$

Notably, the two orthogonal direction change proper distances out of phase, and hence there is effectively a differential arm length change along x and y axes. Figure 1.1 demonstrates how a ring of test particles respond to the two polarization modes of GWs. These free particles, by definition remain at rest indefinitely. What essentially changes by GWs passing through is the proper distance, with a relative change of the order of the GW strain, i.e. $\frac{\Delta L}{L} \sim h$. The two vertical panels of the schematic are visualizations of the effect each of the two polarization modes have on the proper distance between the test particles placed on a ring. We will discuss how this feature makes direct detection of GWs possible in the section 1.2.

1.1.3   Einstein Quadrupole Formula

The above exercise demonstrates the existence of planar GWs away from the source. Now we want to see how the source dynamics affect the amplitude of the emitted wave. In order to do so, one needs to solve the Einstein's field equation in Lorentz Gauge (see Eq. 1.3).

$$\Box \bar{h}_{\mu\nu} = -\frac{16\pi G_N}{c^4} T_{\mu\nu}. \tag{1.10}$$

We can use the Green's function, $G(x - x')$, of the d'Alembertian operator in this case, which satisfies:

$$\Box G(x - x') = \delta^4(x - x'), \tag{1.11}$$

such that the trace reversed strain in the Lorentz gauge is

$$\bar{h}_{\mu\nu}(x) = -\frac{16\pi G_N}{c^4} \int d^4x' \, G(x - x') \, T_{\mu\nu}(x'). \tag{1.12}$$

By imposing the boundary condition that no external radiation enters the system[3], the Green's function takes the form:

$$G(x - x') = -\frac{1}{4\pi |\vec{x} - \vec{x'}|} \delta(ct - |\vec{x} - \vec{x'}| - ct'). \tag{1.13}$$

Here, $\vec{x}$ and $\vec{x'}$ are the spatial position vectors. Plugging this in Eq. 1.12 and integrating over the time coordinate, $x^{0'}$, gives

$$\bar{h}_{\mu\nu}(x) = \frac{4G_N}{c^4} \int d^3\vec{x'} \, \frac{1}{|\vec{x} - \vec{x'}|} T_{\mu\nu}\left(t - \frac{|\vec{x} - \vec{x'}|}{c}, \vec{x'}\right). \tag{1.14}$$

To evaluate the strain at a distance r far from the source of size R (i.e., $r \gg R$), we approximate $|\vec{x} - \vec{x'}| \approx r$. Under this assumption, Eq. 1.15 simplifies to:

$$\bar{h}_{\mu\nu}(x) = \frac{4G_N}{c^4 r} \int d^3\vec{x'} \, T_{\mu\nu}\left(t - \frac{r}{c}, \vec{x'}\right). \tag{1.15}$$

Remember that away from the source, one has the freedom to work in the TT Gauge, where only the spatial components of the strain are non-zero and purely transverse. We

---

[3]This is known as the Kirchhoff-Sommerfeld boundary condition.

will adapt this in two ways. First we evaluate the spatial components of the metric in the Lorentz Gauge using the conservation of stress-energy momentum and next we project this strain onto the plane orthogonal to the propagation direction. The conservation law for the stress-energy momentum tensor, $T^{\mu\nu}$ in flat space is: [4]

$$\partial_\mu T^{\mu\nu} = 0, \tag{1.16}$$

where $\partial_\mu \equiv \frac{\partial}{\partial x^\mu}$ denotes the partial derivative with respect to the coordinate x^μ. From the conservation law, the spatial components of the stress-energy tensor, T^{ij} can be expressed in terms of the time-time component as follows:

$$T^{ij}(t - \frac{r}{c}, \vec{x'}) = \frac{1}{2c^2} \partial_t^2 (x'^i x'^j T^{00}(t - \frac{r}{c}, \vec{x'})) \tag{1.17}$$

Using the perfect fluid model for GW source, one can further use:

$$T^{\mu\nu}(t, \vec{x}) = \rho(t, \vec{x}) u^\mu u^\nu, \tag{1.18}$$

where $u = (c, \vec{v})$ is the four velocity.

Using Eqns. 1.17 and 1.18 in 1.15, we end up with:

$$\bar{h}_{ij}(x) = \frac{2G_N}{c^4 r} \partial_t^2 M_{ij} \left(t - \frac{r}{c} \right),$$
$$M_{ij} \left(t - \frac{r}{c} \right) = \int d^3 \vec{x'} x'^i x'^j \rho \left(t - \frac{r}{c}, \vec{x'} \right) \tag{1.19}$$

M_{ij} is the mass-quadrupole moment of the source. To express this in the TT Gauge, we use the orthogonal projection operator, $P_{ij} = \delta_{ij} - \hat{n}_i \hat{n}_j$, where $\hat{n}$ is the unit vector along the propagation direction. Since the strain in a rank-2 tensor, a rank two TT projection operation $\lambda_{ij,kl}$ can be constructed from P_{ij}, where

$$\lambda_{ij,kl} = P_{ik} P_{jl} - \frac{1}{2} P_{ij} P_{kl} \tag{1.20}$$

---

[4]This follows from the choice of the Lorentz gauge condition, $\partial_\mu h^{\mu\nu} = 0$.

The TT Gauge metric strain is:

$$h_{ij}^{TT}(x) = \lambda_{ij,kl}\,\bar{h}_{kl}(x)$$

$$\Longrightarrow h_{ij}^{TT}(x) = \frac{2G_N}{c^4 r}\partial_t^2 Q_{ij}\left(t - \frac{r}{c}\right), \text{ where} \tag{1.21}$$

Q_{ij} is the TT component of the mass quadrupole expressed as:

$$Q_{ij}(t - \frac{r}{c}) = \int d^3\vec{x}'(x'^i x'^j - \frac{1}{3}r^2\delta_{ij})\rho(t - \frac{r}{c}, \vec{x}') \tag{1.22}$$

Eq. 1.21 reveals that to leading order an accelerating mass-quadrupole moment is essential for GW emission. This is famously known as the Einstein Quadrupole formula [19].

1.2 GW Detections

The small coefficient in the Einstein quadrupole formula (See Eq. 1.21), $\frac{2G_N}{c^4} \sim \mathcal{O}(10^{-44})$ in SI units, is suggestive that GW strain amplitudes are incredibly weak and therefore induce a minuscule change in distances as they pass through, making detections difficult. While we will discuss different GW sources in Section 1.3, but to illustrate the weakness: a vanilla event from the merger of two black holes (BHs) of $30 M_\odot$ at a distance of 400 Mpc away from Earth would cause a typical metric perturbation of 10^{-21}, and therefore a corresponding arm length change of 10^{-18} m in a km long arm. Despite this, there have been numerous attempts at observing the effect of GW propagation.

1.2.1 Resonant Bar Detectors

The first attempt at detecting these distortions was by Weber, who designed resonant bar detectors consisting of large cylindrical metal bars [21]. These were made of aluminum, designed to oscillate in response to passing GWs. If the GW frequency matched the resonant frequency of the detector, the oscillations were amplified due to resonance. In 1969, Weber claimed coincident detections from two facilities located at Argonne National Laboratory and the University of Maryland, suggesting an astrophysical origin [22], only to be later discarded by the wider scientific community. Since Weber's work, many more resonant bar detectors have been developed [23], such as ALLEGRO in the United
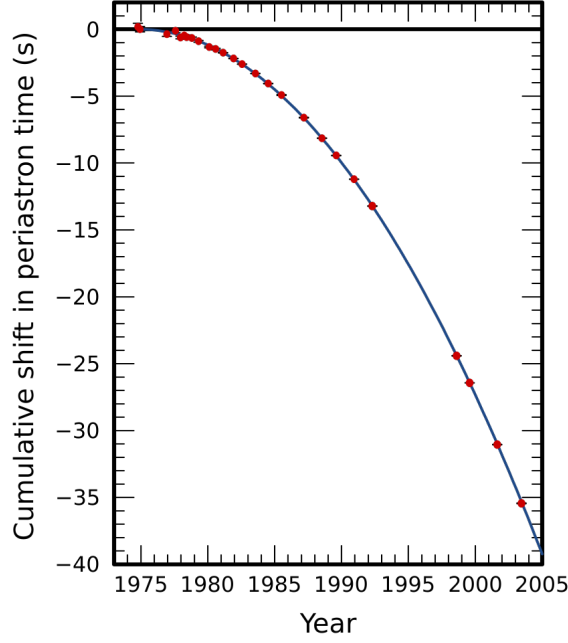
Figure 1.2: Evidence of orbital decay in the Hulse and Taylor binary pulsar, PSR 1913+16 over three decades of observation since detection. Figure taken from [2].

States [24], NIOBE in Australia, and European projects like AURIGA, EXPLORER, NAUTILUS [25, 26]. However, these detectors have significant limitations, such as extremely narrow bandwidth or poor noise sensitivity compared to the current state of art interferometric detectors. It is also worth mentioning here that a future space mission Lunar Gravitational Wave Antenna is in planning phase to use moon as an astronomical resonant bar using an array of inertial sensors on its surface to measure the Moon's vibrations caused by GWs [27].

1.2.2 The Binary Pulsar PSR $1913 + 16$

Arguably the first significant breakthrough at detection, albeit indirect, was the orbital shrinkage and corresponding increase in orbital frequency in the binary pulsar PSR 1913+ 16 discovered by Hulse and Taylor in 1974 [28]. The orbital decay in this binary system could be attributed to the energy lost through the emission of GWs [29]. Red markers in figure 1.2 show the change in periastron time of the eccentric orbit of PSR1913 + 16 observed over three decades since its discovery, and the solid blue curve is the GR prediction of decay from gravitational radiation, illustrating how the orbital dynamics is driven by GW emission [2].
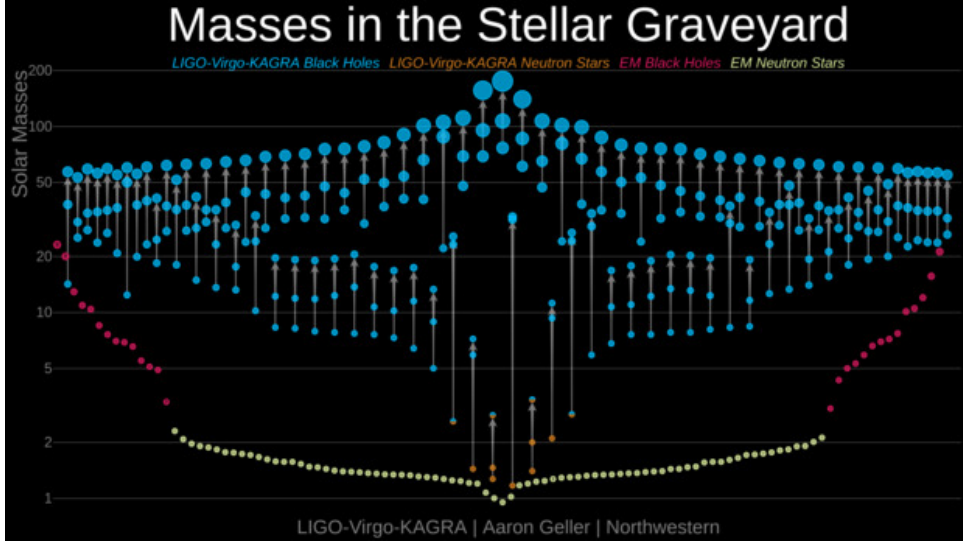
Figure 1.3: The blue (BHs) and orange (NSs) points represent masses of the compact objects discovered by the LVK collaboration until O3 run. The y-axis denotes the mass of the component compact objects. The x-positions are merely for artistic effect. For comparison, the masses of the NSs (in yellow) and BHs (in red) from electromagnetic observations are also depicted. (Credit: LVK / Aaron Geller / Northwestern)

1.2.3 LIGO-Virgo-KAGRA Detections

A pivotal point in GW astronomy was on 14 September 2015 when the two Laser Interferometer Gravitational Wave Observatory (LIGO) [3] detectors in the US observed GW from the merger of two BHs of roughly 30 solar masses each [30]. Since then, the LIGO-Virgo-KAGRA (LVK) [3, 31, 32] collaboration has detected around 90 transient GW signals during their first three observing runs [33, 34], most of which are consistent with GWs produced by coalescing binary BHs (BBHs). GWs from merging binary neutron stars (BNSs) [35, 36] and neutron star-black hole (NSBH) binaries [37] have also been observed. The stellar graveyard, figure 1.3, shows the masses of all the events detected by LVK until the third observing run, and how they already explore territories unchartered by Electromagnetic observations. The ongoing fourth observing run has added and continues to add such compact binary coalescence (CBC) events to the already rich catalog [38]. With future upgrades to the detectors, improvements in noise sensitivity will allow even fainter sources to be detected, increasing the reach. Additionally, the planned LIGO-India observatory will expand the global GW detector network, improving sky localization and enabling better parameter estimation of astrophysical sources [39].

These detections are made using highly sensitive Michelson interferometers that record
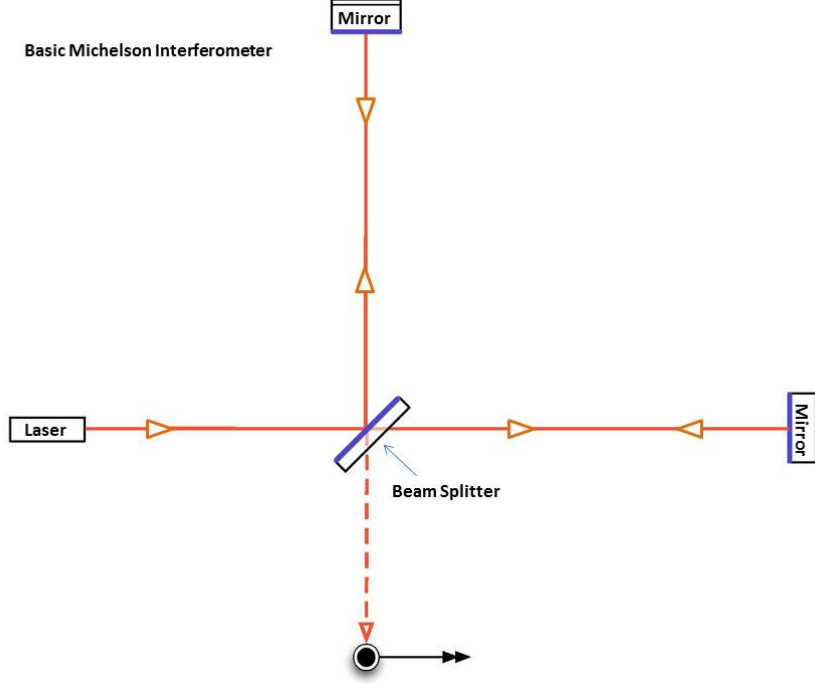
Figure 1.4: The Michelson interferometer layout used in current ground-based interferometers. (Credit: Caltech/MIT/LIGO Lab)

the minute changes produced by passing GWs. As depicted in schematic 1.4, the current ground-based interferometers consist of two very long arms arranged in an L-shaped configuration. A laser beam is split using a beam splitter to maintain coherence and travels along the two arms. The light then bounces off test masses (mirrors) placed at the ends of the arms and travels back to the beam splitter, where the beams interfere depending on the phase shift. A photodiode at the output records the resulting interference.

In the natural state, the arm lengths are adjusted to cause destructive interference at the beam splitter after the round trip. However, when GWs pass through the detector, they cause differential changes in the lengths of the two arms. This change produces a phase shift between the two beams, resulting in non-destructive interference measured at the photodiode. This is recorded as the photodiode voltage, and eventually translated to the relative arm length change through calibration techniques [40–42].

1.2.4   GW strain time series

As an example, in section 1.1 we discussed how free particles respond to GW passing orthogonal to the plane of the particles. However, in the more general case, GWs could
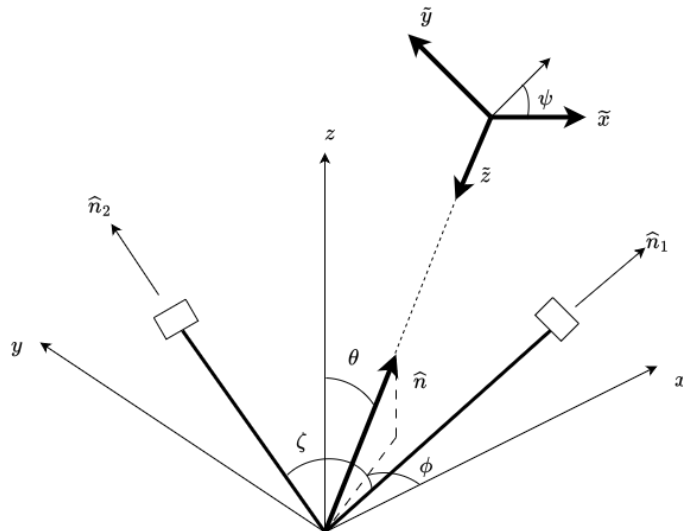
Figure 1.5: Orientation of the detector frame coordinate system to the source frame coordinates. $\hat{n}$ is the direction of the source from the detector and is given by the spherical polar angles θ and ϕ. ψ denotes the polarization angle of the source. The $\sim$ coordinates are attached to the source while the ones without $\sim$ are in the detector frame. $\hat{n}_1$ and $\hat{n}_2$ are the two arms of the detector placed symmetrically in the $x - y$ plane with an opening angle of ζ. For current detectors with orthogonal arms, $\hat{n}_1$ and $\hat{n}_2$ coincides with the x and y axes at the detector respectively.

originate from any direction in the sky. In that case, the strain in the detector proper frame is no longer of the form in Eq. 1.7. Our treatment follows from [43] to understand the response of the detector to GW originating from the sky location, $\hat{n}$. In the coordinate attached to the source, we choose the $\tilde{z}$-axis to align with the direction of propagation and the spatial strain tensor takes the form:

$$\tilde{H}(t) = \begin{pmatrix} h_+(t) & h_\times(t) & 0 \\ h_\times(t) & -h_+(t) & 0 \\ 0 & 0 & 0 \end{pmatrix} \tag{1.23}$$

We will use $\sim$ to denote strain and coordinates in the source frame. The strain tensor in the detector frame can be obtained via a similarity transformation using the orthogonal transformation matrix, $M(t)$, which rotates the source frame onto the detector frame.

$$H(t) = M(t) \cdot \tilde{H}(t) \cdot M(t)^T \tag{1.24}$$

Let us try to now derive the form of the transformation matrix, $M(t)$, which is essential

to write the strain tensor in the Cartesian frame attached to the detector. Any general rotation in 3 dimensions can be achieved by a set of three Euler-Rotations about the Z-Y-Z axes. From the fig. 1.5, the three Euler angles of rotation for the Z-Y-Z rotations are ψ, $\pi - \theta$ and $-\phi$ respectively, where ψ, ϕ, θ are the polarization, azimuthal and spherical polar angles respectively. The orthogonal transformation matrix, M, is thus given by:

$$M = R(\hat{z}, -\phi) \cdot R(\hat{y}, \pi - \theta) \cdot R(\hat{z}, \psi)$$

$$= \begin{pmatrix} \cos\phi & \sin\phi & 0 \\ -\sin\phi & \cos\phi & 0 \\ 0 & 0 & 1 \end{pmatrix} \cdot \begin{pmatrix} \cos(\pi - \theta) & 0 & \sin(\pi - \theta) \\ 0 & 1 & 0 \\ -\sin(\pi - \theta) & 0 & \cos(\pi - \theta) \end{pmatrix} \cdot \begin{pmatrix} \cos\psi & -\sin\psi & 0 \\ \sin\psi & \cos\psi & 0 \\ 0 & 0 & 1 \end{pmatrix}$$

$$= \begin{pmatrix} -\cos\phi\cos\theta\cos\psi + \sin\phi\sin\psi & \cos\phi\cos\theta\sin\psi + \sin\phi\cos\psi & \cos\phi\sin\theta \\ \sin\phi\cos\theta\cos\psi + \cos\phi\sin\psi & -\sin\phi\cos\theta\sin\psi + \cos\phi\cos\psi & -\sin\phi\sin\theta \\ -\sin\theta\cos\psi & \sin\theta\sin\psi & -\cos\theta \end{pmatrix}$$

$$\tag{1.25}$$

A detector placed symmetrically in the $x - y$ plane with opening angle ζ has arms along:

$$\hat{n}_1 = \begin{bmatrix} cos(\frac{\pi}{4} - \frac{\zeta}{2}) \\ sin(\frac{\pi}{4} - \frac{\zeta}{2}) \\ 0 \end{bmatrix} \quad \text{and} \quad \hat{n}_2 = \begin{bmatrix} sin(\frac{\pi}{4} - \frac{\zeta}{2}) \\ cos(\frac{\pi}{4} - \frac{\zeta}{2}) \\ 0 \end{bmatrix}$$

The GW scalar strain measured in the detector is given by the difference of the projection of the detector frame strain tensor along the two arms [43]:

$$h \equiv \frac{\Delta L}{L} = \frac{1}{2}\hat{n}_1^T \cdot H \cdot \hat{n}_1 - \frac{1}{2}\hat{n}_2^T \cdot H \cdot \hat{n}_2 \tag{1.26}$$

Using the rotation matrix derived in Eq. 1.25 and the detector frame strain tensor (Eq. 1.24), the scalar strain (Eq. 1.26) takes the form:

$$h(t) = F_+(t; \theta, \phi, \psi, \zeta)h_+(t) + F_\times(t; \theta, \phi, \psi, \zeta)h_\times(t), \tag{1.27}$$

where,

$$F_+(\theta, \phi, \psi, \zeta) = \sin\zeta \left[\frac{1}{2}(1 + \cos^2\theta)\cos(2\phi)\cos(2\psi) - \cos\theta\sin(2\phi)\sin(2\psi) \right], \qquad (1.28)$$

$$F_X(\theta, \phi, \psi, \zeta) = \sin\zeta \left[\frac{1}{2}(1 + \cos^2\theta)\cos(2\phi)\sin(2\psi) + \cos\theta\sin(2\phi)\cos(2\psi) \right]. \qquad (1.29)$$

$F_+(\theta, \phi, \psi, \zeta)$ and $F_\times(\theta, \phi, \psi, \zeta)$ are called the antenna pattern functions, and characterize the response of the interferometers to GWs originating from the different positions in the sky at any given point of time. The time dependence of the antenna pattern function is implicit here because in the frame attached to the detector, the angular position of the source (θ, ϕ) changes due to the detector motion. To explicitly denote the time dependence, Jaranowski-Krolak-Schutz [43] express this antenna pattern function in the ecliptic coordinates attached to the Solar System Barycenter(SSB) where the sky angles are given by the right ascension (α) and declination(δ).

$$F_+(t) = \sin\zeta \left[a(t)\cos(2\psi) + b(t)\sin(2\psi) \right] \qquad (1.30)$$

$$F_\times(t) = \sin\zeta \left[b(t)\cos(2\psi) - a(t)\sin(2\psi) \right], \qquad (1.31)$$

$a(t)$ and $b(t)$ can be read from Eq. (12) and (13) of [43], and explicitly indicate the daily and yearly variation for a source at $\hat{n}$ due to the detectors motion. The time dependence of the antenna pattern function is usually ignored for short duration signals, but should be accounted for in order to search for signals in longer stretches of the data. The above exercise encapsulates the form that the scalar output at a detector assumes in the presence of a GW signal, with the key Eq. being 1.27.

1.2.5   Noise affecting GW detectors

While these detectors are capable of measuring very small arm length changes – several orders smaller than the size of an atomic nuclei – there exists several scientific and engineering challenges. The major are the terrestrial noise sources that can pollute strain output of the detectors and even at times mimic GWs. These noise sources span a broadband of frequencies where the astrophysical sources emit actual GW signals. Much like GW strain output, $h(t)$, the noise also has its time series strain, $n(t)$. The signal in the

detector is a linear superposition of noise and GW strain.

$$s(t) = n(t) + h(t) \tag{1.32}$$

Under the Gaussianity and stationary approximation of the noise, the performance of the detector is quantified entirely using the noise power spectral density (PSD), $S_n(f_{\mathrm{GW}})$

$$\langle \tilde{n}(f)\tilde{n}^*(f') \rangle = \frac{1}{2}\delta(f - f')S_n(f). \tag{1.33}$$

Here $\tilde{n}(f)$ is the Fourier transform of the noise time series $n(t)$ and $\tilde{n}^*(f)$ denotes its complex conjugate. $\langle \cdot \rangle$ indicates an ensemble average, which, by the assumption of ergodicity, can be replaced by a time average over different noise samples.. Also, since the noise time series is real, $\tilde{n}(-f) = \tilde{n}^*(f)$, implying $S_n(f) = S_n(-f)$. We can therefore represent the noise budget using a one-sided PSD. A lower PSD means better performance and less noise contamination. The PSD has contribution from several fundamental and technical noise sources. Figure 1.6 shows the individual and cumulative contribution from various noise sources to the Advance LIGO amplitude spectral density (ASD), $\sqrt{S_n(f)}$. We discuss some of these fundamental noise sources below:

Seismic and Newtonian Noise

Seismic noise arises from the persistent and variable ground vibrations of the Earth. These could be due to earthquakes, wind, oceanic movements, human activity, etc. and affect the noise PSD between 0.1–10 Hz [44]. It couples to the GW detectors through the suspension systems that hold the test masses in place. Thus, use of advanced isolation systems helps tackle the effect of seismic noise. Below 10 Hz, another major contribution to the PSD comes from the Newtonian noise. They exist due to the local variation of gravitational potential from moving masses near the detector, atmospheric pressure gradients, etc. Since Newtonian noise couples to the test masses via gravity, it is difficult to shield against. Active noise cancellation currently employed by LIGO monitor a noise source through dedicated sensors and apply linear filters to subtract the correlated noise. For future ground based detectors, excavating cavities near detector test mass to reduce local density fluctuations are also proposed strategies to reduce Newtonian noise.

Thermal Noise

These are mid-frequency noise (tens to hundreds of Hz) arising from the Brownian motion of atoms in interferometric components, such as suspension fibers and mirror coatings [45, 46]. Mirror coating suffer mechanical dissipation due to thermal fluctuations, while there are energy damping losses to the suspension fibers at their attachment points. Low-loss optical coating, use of high purity substrate such as fused silica and cryogenic cooling (proposed for future detectors) helps to significantly lower this noise.

Quantum Noise

Quantum noise results from the quantum nature of the light used in the interferometer and has two major components: radiation pressure noise at low frequency and shot noise at high frequency [47]. Radiation pressure noise results from the quantum uncertainty in the momentum transfer of photons striking the mirror, leading to fluctuations in its position. This leads to phase uncertainty in the light arriving at the output photodiode. At high frequency, the dominant noise contribution comes from shot noise due to Poisson fluctuation in the number of photons arriving at the photodiode, resulting in amplitude uncertainty. Use of high power LASER reduces the shot noise in detectors, but simultaneously increases the radiation pressure noise due to the Heisenberg uncertainty principle. To mitigate this, squeezed states of light are used in the interferometer to reduce either the phase or the amplitude uncertainty at the expense of other [48]. Future generation of detectors also plan to use frequency-dependent squeezing to reduce the shot noise and radiation pressure noise in their dominant frequency ranges [49].

Transient Glitches

Transient glitches arise from occasional short-duration terrestrial aberrations that mimic GW signals. These can affect any frequency range depending on the origin, such as seismic activities, power line fluctuations, local pressure gradients, instrumental malfunction, etc. They appear in the detector as either blips (very short and sharp spike), chirps (increasing frequency with time) or as narrow band noise lines. Glitch subtraction techniques that relies on modeling and removing these [50], citizen science projects such as Gravity Spy [51], tracking the auxiliary channels in the interferometer [52] are methods used to deal
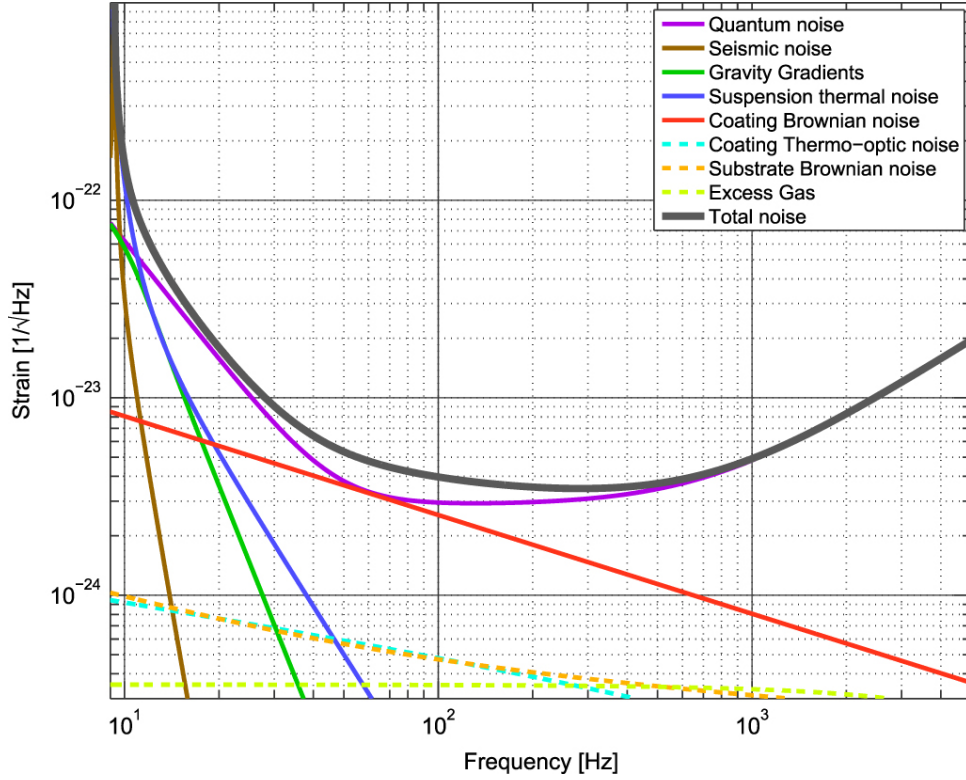
Figure 1.6: The noise budget for the high power mode of Advanced LIGO. Figure credit: Reference [3].

with these noise artifacts.

1.2.6 Future generation of GW detectors

In addition to continuous upgrades to current detectors, there are also plans to build future generation of GW detectors with two primary objectives: (a) Improve sensitivity by lowering the noise budget (b) Expand the detection bandwidth to detect new classes of GW sources that don't populate the current detector bandwidth. These future generations of detectors include:

Einstein Telescope

The Einstein Telescope (ET) [53–55] is a planned third-generation underground detector with triangular configuration of 10 km arms. Being underground will provide it significant cushion against the low frequency seismic noise extending its sensitivity down to 1 Hz, compared to the 10 Hz limit of current detectors. To minimize thermal noise and enhance mid-frequency sensitivity, ET will also employ cryogenic cooling facilities for the mirrors. Additionally, to suppress high-frequency quantum noise, it will utilize quantum-squeezed

high-power lasers. With better performance across the frequency bandwidth, ET promises to be around 10 times more sensitive than the current GW detectors.

Cosmic Explorer

The Cosmic Explorers (CEs) [56] are essentially an upgraded and larger version of current Advanced LIGO detectors. At present, the plan includes to build two such interferometers with respective arm lengths of 40 and 20 kms in the United States. In addition to this, further advancements in mirror coating, quantum noise suppression and seismic isolation for CE will enable broader frequency range of detection, along with improved noise sensitivity as compared to current facilities.

Laser Interferometer Space Antenna

Laser Interferometer Space Antenna (LISA) [57] is a space mission planned to be launched in 2030′s by the European Space Agency in collaboration with National Aeronautics and Space Administration. This will make use of LASER interferometry between free falling test masses in an equilateral triangle configuration of around 2.5 million kms in length. Free from terrestrial noise sources, such as seismic noise, LISA will operate in the milli-hertz range making it a complementary mission to ground-based interferometers. The detection frequencies of LISA will be populated by supermassive and intermediate mass BH binaries, galactic white dwarf binaries and extreme mass ratio inspirals, as well as cosmological sources from early universe [58]. Additionally, LISA will be able to observe the early inspiral phases of sources detectable by the contemporary ground based detectors like ET and CE, providing early warnings for multimessenger follow-ups. Plans for similar space missions like TianQin [59] by China and DECIGO [60] by Japan are also in place.

1.3 Sources of GWs

In the previous section, we discussed how GWs are generated by accelerating mass quadrupole and how they interact with interferometric detectors. In principle, any mass quadrupole acceleration produces GWs. But those produced by terrestrial activities are insignificant to be detected. We need energetic astrophysical processes to produce

observable GWs. These processes typically fall into four categories: Compact Binary Coalescences (CBCs), Bursts, Stochastic GW Background (SGWB) and Continuous GWs (CWs). In this section, we discuss these astrophysical sources and the relevant data analysis tools that will come in handy in later chapters. [5]

1.3.1 Compact Binary Coalescences

Compact objects in binaries, such as NSs and BHs, that have orbital separation so as to merge within the age of the universe produce GWs detectable by the current and future GW observatories. The binary loses energy and angular momentum through the emission of GWs during their *inspiral* phase, driving their orbits to shrink. The GW signal from CBCs during inspiral exhibit characteristic "chirp" where both their GW frequencies (which are tied to their orbital frequency) and GW amplitude increase as they come closer. Eventually, the components plunge toward each other in what is called the *merger* phase. If the remnant is a BH, it undergoes a *ringdown* phase, emitting the asymmetries as quasi normal GW modes and finally settles in a stable configuration.

For the current ground based detectors operating between $10 - 2000$ Hz, these transients spend around a fraction of a second to a few seconds within the detector band, depending on the nature and mass of the binary components. Lighter BHs or NSs that are only tens of kms in radii achieve very close orbital separation allowing their GW frequencies to sweep through the entire bandwidth. These could therefore be a several seconds long in duration. Heavier BH binaries on the other hand, merge at larger orbital separation, creating shorter transients. Mass solely isn't decisive. For instance, white dwarf binaries with components of the length-scale of few thousand kms would come in contact and therefore merge well before their GW emission frequencies reach the sensitivity range of current detectors.

Although CBCs fall under the category of "well understood" class of signals, modeling their GW waveform is a complicated task. The two-body problem in GR, unlike Newtonian gravity doesn't have closed form analytical solutions. One needs to rely on either perturbative methods, such as post-Newtonian (PN) expansion [61–64] or numerical relativity (NR) solutions [65–67] to extract the orbital dynamics and the GW waveforms.

---

[5]While we briefly introduce CBCs, Bursts and SGWBs in this section, we will dedicate the next section to provide detailed summary of CWs as they form the central theme of this thesis

PN expansion in velocity v/c is a reasonable approximation for the early inspiral phase when the binary components are well separated and their velocities are non-relativistic. But as the objects come close, their velocities become relativistic, i.e. $v/c \sim 1$, causing the perturbation series to break down. For this merger phase, one has to rely on full NR simulations to model the signal, which are computationally expensive. After the merger, the remnant radiates the unstable asymmetry as quasi-normal modes [68]. This ringdown phase is well modeled by BH perturbation theory (BHPT) [68]. And eventually, in order to construct computationally feasible and accurate waveform, phenomenological methods to stitch the waveform together from PN, NR and BHPT [69], and effective one body formalism [70] have been a successful strategies.

One major challenge when searching for GW strain in the detector output is that the signal time series is buried deep within the noise, i.e. $|h(t)| \ll |n(t)|$, making it a classic needle in a haystack problem. However, precise knowledge of the waveform enables cross-correlation of the data to these modeled waveforms to dig the faint signal. The optimal strategy to look for signals in Gaussian noise is the match-filtering technique [71,72]. The output is a noise weighted inner product of the data with the known templates that GR predicts:

$$\langle s|h(\vec{\theta})\rangle = 4\,\mathrm{Re}\int_{f_{min}}^{f_{max}} \frac{\tilde{s}^*(f)\tilde{h}(f;\vec{\theta})}{S_n(f)}\,df. \qquad (1.34)$$

Here,

- $\tilde{s}(f)$ and $\tilde{h}(f;\vec{\theta})$ are the Fourier transforms of the data and template, respectively.

- $\vec{\theta}$ is the parameter value at which waveform $\tilde{h}(f;\vec{\theta})$ is evaluated, e.g. component masses, spins, etc.

- $S_n(f)$ is the one-sided PSD of the detector noise.

- The asterisk (*) denotes complex conjugation.

The detection statistics, match filter signal-to-noise ratio (SNR), ρ, is then defined as:

$$\rho = \frac{\langle s|h\rangle}{\sqrt{\langle h|h\rangle}}. \qquad (1.35)$$

However, even in presence of a signal, a-priori we don't know the signal parameters themselves. Searches therefore rely on creating template banks across the parameter space of

interest [73–75]. The data is match-filtered against theoretical templates $h(\vec{\theta})$ where $\vec{\theta} \in$ template bank. The maximum output SNR is compared against a predefined threshold value to generate event triggers.

A GW trigger from searches recover the maximum SNR and the corresponding best fit template. The more refined inference of the source properties traditionally make use of Bayesian Parameter Estimation (PE) techniques [76–78]. The posterior probability distribution on the source property given data s, $p(\vec{\theta}|s)$, is constructed using Bayes' theorem.

$$p(\vec{\theta}|s, H) = \frac{\mathcal{L}(s|\vec{\theta}, H)\pi(\vec{\theta}|H)}{\mathcal{Z}(s|H)} \tag{1.36}$$

where:

- H is the hypothesis: here that a GW signal is present and the signal model is defined precisely by the templates used.

- $p(\vec{\theta}|s, H)$ is the **posterior distribution**, i.e. probability of the parameters $\vec{\theta}$ given the data s.

- $\mathcal{L}(s|\vec{\theta}, H)$ is the **likelihood function**, which essentially is the probability distribution of the data given parameters $\vec{\theta}$.

- $\pi(\vec{\theta}|H)$ is the **prior distribution**, based on astrophysical knowledge or constraints on $\vec{\theta}$.

- $\mathcal{Z}(s|H)$ is the **evidence** (or marginal likelihood), given by:

$$\mathcal{Z}(s|H) = \int \mathcal{L}(s|\vec{\theta}, H)\pi(\vec{\theta}|H)d\vec{\theta}. \tag{1.37}$$

The likelihood function of $\vec{\theta}$ is constructed by demanding that if the signal template, $h(\vec{\theta})$ is removed from the data, s, the stationary noise should follow a Gaussian distribution, therefore:

$$\mathcal{L}(s|\vec{\theta}) \propto \exp\left(-\frac{1}{2}\langle s - h(\vec{\theta})|s - h(\vec{\theta})\rangle\right), \tag{1.38}$$

where the inner product is defined in Eq.1.34. The parameters are described by 15(17) dimensional space in case of BBHs (BNSs), such as intrinsic parameters like component masses, spins (also tidal defomability in case of NSs), and extrinsic parameters such as inclination, polarization angle, distances, etc. To effectively sample the high dimensional parameter space, stochastic sampling methods such as nested sampling are employed [79]. A bunch of random walkers are initialized following the prior distributions, and at each step the walkers aim to maximize the likelihood function. Eventually, the histogram of the sampled parameters after convergence represent the posterior distribution.

1.3.2 Bursts

These are short-duration, broadband transients that could arise from catastrophic astrophysical events, such as core-collapse supernovae, post-merger remnants of BNS mergers, and pulsar glitches. Core-collapse supernovae, for instance, generate GWs due to the asymmetric motion of mass accompanying the explosion [80, 81]. BNS mergers, on the other hand, could lead to hypermassive (and therefore unstable) NS remnants [82], which eventually collapse into BHs, producing GWs in the process [83].

Unlike CBCs, however, little is known about the signal model for such events due to the chaotic, nonlinear physics such as turbulent fluid instabilities, neutrino transport, etc. essential to describing them [84]. While the match-filtering techniques discussed in the previous section prove to be optimal for well-modeled signals buried in Gaussian noise, they are an unviable strategy for burst searches. To mitigate the reliance on waveform templates for bursts, the usual strategy involves a time-frequency analysis searching for excess coincident power in multiple detectors [85, 86]. Assuming that terrestrial noise across detectors are uncorrelated, a multiple-detector search suppresses the effects of glitches in individual detectors that could mimic such short, unmodeled transients.

1.3.3 Stochastic GW Background

SGWB can arise from a cocktail of several astrophysical and cosmological processes. Early universe phenomena like inflation, phase transition, cosmic strings may have left GW imprints, much like the cosmic microwave background [87]. Additionally, an astrophysical foreground of CBCs that are too weak or distant to be individually detected and resolved can contribute to the SGWB [88, 89]. In individual detectors, they would deposit excess

power in the frequency bins, resembling terrestrial noise sources which dominate the PSD. This makes it essential to cross correlate strain time series from multiple detectors to pick up SGWB contribution, with the assumption that noise is uncorrelated [90]. While, LVK hasn't detected SGWB, the Pulsar Timing Array collaboration has presented some evidence for GW background in the nano-hertz band by monitoring the variation in pulse arrival time from known millisecond pulsars [89, 91, 92].

1.4 Continuous GWs

CWs are signals that last in the detector bandwidth for a very long duration. While there isn't a clear demarcation on how long, a useful criteria is that the temporal dependence of antenna pattern function (see Eq. 1.30) becomes important for these, whereas they can be approximated to be constant for transients. The specific nature of astrophysical sources that could give rise to such signals depend on the detector's frequency bandwidth. For example, GWs from very early inspirals of stellar mass binaries will spend much longer duration in the LISA band making them CW sources for that detector, whereas they spend only up to a few seconds and appear as transients in current Earth based observatories. In this section, we focus exclusively on CW sources for present and upcoming ground-based facilities, excluding early inspirals of CBCs from our discussion. For our case, the most promising source of CWs are rapidly spinning non-axisymmetric NSs within our galaxy. Therefore, we provide brief summary of NS physics, CW emission mechanisms, signal model and the implications of current CW searches on NS properties in this section.

1.4.1 Neutron Stars

Originally proposed by Baade and Zwicky, NSs are the stellar graves of massive stars. When massive stars run out of lighter elements to fuel fusion and counteract gravity, they collapse under their own gravitational field, leading to a core-collapse supernova [93, 94]. With the infall of matter within a confined core, the high density achieved results in rapid neutronization by an inverse beta decay process that converts protons and electrons to neutrons and neutrinos. For progenitor stars roughly in the mass range of $6 - 15 M_\odot$, the resultant neutron degeneracy pressure, due to the Pauli exclusion principle, can prevent

further collapse of the remnant core [93, 95].

Heavier progenitors lead to a core that can't be sustained through neutron degeneracy pressure and collapse to BHs, while lighter progenitors will settle to an iron-rich white dwarf core supported by electron degeneracy pressure. Remnant NSs remain in a stable state for masses less than the Tolman–Oppenheimer–Volkoff mass limit, estimated to be in the range of $2.2-2.9M_\odot$ depending on the equation of state [96]. The heaviest observed NS is PSR J0952 − 0607, with a mass of $2.35 \pm 0.17M_\odot$ [97]. The infalling outer layer of the progenitor bounces off the stiff NS core and is energized by the outgoing neutrinos, resulting in an explosion. The ejecta eventually settles as the supernova remnant nebula. Even for a fraction of angular momentum and energy retained by the progenitor core, the young remnant NS can have extreme properties, like high temperature, rotation frequency, and magnetic fields (in extreme cases leading to magnetars with magnetic field strengths greater than 10^{14} G). The remnant, however, rapidly cools through neutrino and thermal emission [98], and spins down through different channels, like pulsar wind, magnetic dipole emission, GW emission, etc. See section 2.1.2 in [99] for detailed discussion on NS spin down phenomenology.

NSs have been observed across the electromagnetic spectrum. For example, young hot NSs emit thermal radiation from their surface across infrared to X-ray band [100]. Non-thermal emissions have also been observed, such as from isolated magnetized pulsars in the radio band, X-ray emission in low-mass X-ray binaries through Roche-lobe overflow, and radio and gamma-ray emission from recycled old millisecond pulsars which have been spun up over time through accretion from a binary companion. To date, approximately 3,300 NSs have been observed by electromagnetic observations, primarily as radio pulsars, with some also detected through X-ray and Gamma-ray observations [8, 101].

1.4.2 GW radiation

In this section, we explore the mechanisms responsible for CW emission from NSs. There are three principle channels for such emissions:

- Mass quadrupole emission.

- Mass-current quadrupole emission.

- Free Precession.

Mass quadrupole emission

Among the aforementioned, the most widely studied CW emission mechanism for NSs is the non-axisymmetric mass distribution, akin to the presence of mountain on the otherwise spherical configuration [43, 102]. According to the Einstein quadrupole radiation formula (Eq. 1.21), the typical GW strain amplitude for NS spinning with frequency, $f_\star$, moment of inertia I about its rotation axis, at a distance r from the detector is given by:

$$h_0 = \frac{16\pi G_N}{c^4} \frac{I \epsilon f_\star^2}{r}, \tag{1.39}$$

where ellipticity ϵ quantifies the degree of mass asymmetry [6]:

$$\epsilon = \frac{I_{xx} - I_{yy}}{I}. \tag{1.40}$$

I_{xx} and I_{yy} are the moment of inertia along the two principal axes orthogonal to the rotation axis. This is commonly known as the triaxial ellipsoid model for NSs. NSs exhibiting such mass deformability emit quasi-monochromatic GWs at twice the rotation frequency of the star, i.e., $f_{\mathrm{GW}} = 2f$.

However, both the maximum degree of asymmetry theoretically allowed for NSs and their likely values from various physical processes remain uncertain. For conventional NSs, the estimate of maximum ellipticity sustained is given by [102] as:

$$\epsilon \leq 5 \times 10^{-7} \left(\frac{\sigma}{10^{-2}} \right), \tag{1.41}$$

where σ is the breaking strain. σ could in principle be as high as 10^{-1} for pure crystalline structures [103]. [104] suggests a maximum ellipticity limit of $\epsilon_{\max} = 7.4 \times 10^{-6}$. For more exotic composition, the theoretically allowed limits are higher due to higher shear modulus. For example, stars with solid strange matter core can withstand a maximum ellipticity up to 10^{-4} [105], while a hybrid star with quark core can sustain $\epsilon \sim 10^{-5}$ [106, 107]. More recent estimates, [108], show that these compositions could sustain ellipticities of $10^{-3}(10^{-1})$ for hybrid (purely quark) cores.

A more pressing question is what physical processes drive mass asymmetry in NSs. For younger NSs, it could be a result of the residual asymmetries from the core collapse

---

[6]This is not to be confused with the ellipticity of the binary orbits for CBCs

supernova [109]. Magnetized NSs on the other hand can have $\epsilon \sim 10^{-6}$ if the magnetic dipole moment is not aligned with the rotation axis [110]. For older NSs with a history of accretion from a binary companion, the accreted mass may lead to mass asymmetry. Furthermore, in the presence of magnetic field, the accreted matter is funneled to "hot-spots" on the NS surface, creating a magnetically confined mountain where ϵ can achieve values close to the breaking limit [111]. Regardless of the mass asymmetry mechanism, higher ellipticities are essential to detectable GWs from rotating NSs.

Substituting the constants in Eq. 1.39, the strain is:

$$h_0 \approx 4.4 \times 10^{-26} \left(\frac{I}{10^{38}\,kg\,m^2} \right) \left(\frac{\epsilon}{10^{-6}} \right) \left(\frac{f_\star}{100Hz} \right)^2 \left(\frac{1kpc}{r} \right). \qquad (1.42)$$

Evidently, even for Galactic source the strain is orders below the typical CBC strain. The saving grace is that these signals would last in the detector band for long duration. This is due to low spin-down of NSs. For example, if we consider NSs losing energy and momentum only through gravitational mass-quadrupole radiation, the spin down rate is:

$$\dot{f}_{GW} = \frac{-32\pi^4 G}{5c^5} I\epsilon^2 f_{GW}^5. \qquad (1.43)$$

For a kHz GW source with $\epsilon = 10^{-6}$, the spin-down magnitude is $\mathcal{O}(10^{-9}s^{-2})$. In practice, the rotation energy of the NS can be lost through additional channels such as pulsar wind, magnetic dipole etc. further increasing the spin-down rate. Nevertheless, despite these losses, NSs can remain within the detector's sensitivity band for long periods, making them promising candidates for CW detection. It is also useful to highlight that the frequency evolution is a distinguishing feature of different CW emission channels. For mass-quadrupole radiation, $\dot{f}_{GW} = Kf_{GW}^n$, where the braking index n is 5, as evident from Eq. 1.43.

Mass-Current Quadrupole Emission

Rotating NSs can have dynamical instability due to crustal fluid counter-rotating with respect to the rotating frame of the star. If the star emits GW due to initial non-axisymmetric mass current modes, the back-reaction from the gravitational radiation can amplify these oscillation modes rather than dampen them, commonly known as the Chandrashekhar-Friedmann-Schutz instability [112]. Such toroidal fluid oscillations in

rotating stars, known as "r-modes", however are dampened dominantly by the shear viscosity at lower temperature and by bulk viscosity at high temperature [113] [7]. The presence of stellar magnetic field also counteracts r-modes, since gravitational back-reaction alone cannot efficiently counteract the magnetic energy to sustain the instability [114]. Therefore, the time-scale for radiation cannot be certainly established. For example, in newborn NSs these modes could decay over the time-scale of months, while for actively accreting system these could last for thousands of years [115, 116]. Regardless of these uncertainties, r-mode oscillations are expected to be CW emitters at GW frequency of about $\frac{4}{3}f_\star$ for these newborn or accreting NSs. The strain amplitude and spin-down due to r-mode oscillation is given by [117] as:

$$h_0 = \sqrt{\frac{512\pi^7}{5}} \frac{G_N}{c^5 r} f_{\mathrm{GW}}^3 \alpha M R^3 \tilde{J}, \tag{1.44}$$

$$\dot{f}_{\mathrm{GW}} = -\frac{4096\pi^7}{225} \frac{G_N}{c^7} \frac{M^2 R^6 \tilde{J}}{I} \alpha^2 f_{\mathrm{GW}}^7, \tag{1.45}$$

where α is the dimensionless r-mode amplitude, M and R are the mass and radius of the star respectively, and $\tilde{J}$ is the dimensionless functional of the stellar equation of state (see [117] for details). The braking index of $n = 7$ for r-mode radiation is evident in Eq. 1.45.

Free Precession

NSs with rotation axis misaligned with the principal moment of inertia axis are freely precessing systems [118, 119]. In this case, the stars emit GWs at close to the rotation frequency and its higher harmonic at twice the rotation frequency [120]. The expansion parameter is the wobble (misalignment) angle (θ_w) of the two axes, with typical strain of the order:

$$h_0 \sim 10^{-27} \left(\frac{\theta_w}{0.1\ \mathrm{rad}}\right) \left(\frac{1\ \mathrm{kpc}}{r}\right) \left(\frac{f_\star}{500\ \mathrm{Hz}}\right)^2, \tag{1.46}$$

---

[7]Other unstable modes such as fundamental(f)-mode and pressure(p)-mode are also excited for higher rotation rates close to the breaking limit.

1.4.3 Signal Morphology

Throughout the thesis, we will deal with just the mass quadrupole radiation from NSs. But irrespective of the emission channel, one feature common to CWs is their weakness and quasi-monochromatic nature. This section is therefore generic to all the above mentioned mechanisms. For simplicity however, we adapt the triaxial phase model form of $f_{\rm GW} = 2f_\star$.[8] We will further just consider NSs which are isolated or in wide binaries such that the revolution around the binary barycenter is negligible. Since we are interested to learn about the phase evolution at the detector, we will start with writing the waveform at the source, then evaluate the time when the wavefront reaches the SSB, and finally the time when it reaches the detector.

In the frame attached to the NS, the GW frequency can be Taylor expanded, i.e.

$$f_{\rm GW}(t_{\rm NS}) = \sum_{k=0}^{k_{\rm max}} f_{\rm GW}^{(k)} \frac{t_{\rm NS}^k}{k!}, \qquad (1.47)$$

where the the superscript k denotes the k-th instantaneous time derivative at reference time of $t_{\rm NS} = 0$. The GW phase at NSs, $\phi(t)$ can be evaluated by the time integral of the frequency Taylor series, and therefore:

$$\phi(t_{\rm NS}) = 2\pi \sum_{k=0}^{k_{\rm max}} f_{\rm GW}^{(k)} \frac{t_{\rm NS}^{k+1}}{(k+1)!} \qquad (1.48)$$

To evaluate the time at the SSB for the arrival of the same wavefront, we can get away with just including the distance from the isolated NSs to SSB. [9]

For an isolated, non-relativistic source at a distance r, the time at which the same wavefront reaches the SSB is given by: [10]:

$$t_{\rm SSB} = t_{\rm NS} + \frac{r}{c} \qquad (1.49)$$

---

[8]For any other emission mechanism the following discussion holds with the understanding of $f_{\rm GW} = Cf_*$ where $C = \frac{4}{3}, 1$ and 2 for r-modes and the dual harmonics of free precession, respectively.

[9]We neglect the time shift due to binary motion of the source such as the Rømer, Einstein and Shapiro delays since they are either 0 or negligible for isolated sources. See section 2.2 in [121] where these terms are included.

[10]There are possibilities of additional redshift/blueshift due to radial motion of the star, but those can be accounted for by just re-parameterizing the Taylor-expansion coefficients of frequency at the SSB and doesn't alter the signal model itself.

Since $\frac{r}{c}$ is a constant, we can define a time shift t_0, allowing us to use t_{SSB} and t_{NS} interchangeably.

Next, we convert this to the time at which this phase is measured at the detector. For a standard celestial sphere reference frame at the SSB, the sky location ($\hat{n}$) for the source is related to the right ascension (α) and the declination (β) angles as:

$$\hat{n} = (\cos\alpha \cos\delta, \sin\alpha \cos\delta, \sin\delta) \tag{1.50}$$

With this choice, the time of arrival of the same wavefront at the SSB and the detector is related by:

$$t_{\mathrm{SSB}} = t_{\mathrm{det}} + \Delta_{\mathrm{R}_\odot}(t_{\mathrm{det}}) + \Delta_{\mathrm{E}_\odot}(t_{\mathrm{det}}) - \Delta_{\mathrm{S}_\odot}(t_{\mathrm{det}}), \tag{1.51}$$

where:

- **Rømer Delay**: $\Delta_{\mathrm{R}_\odot} = \frac{\vec{r}(t_{\mathrm{det}})\cdot\hat{n}}{c}$ accounts for the propagation delay from the SSB to the detector. Here $\vec{r}(t_{\mathrm{det}})$ denotes the position vector of the detector with respect to the SSB.

- **Einstein and Shapiro Delays**: $\Delta_{\mathrm{E}_\odot}$ and $\Delta_{\mathrm{S}_\odot}$ account for gravitational time dilation effects due to celestial bodies in the Solar System.

From the expressions 1.49 and 1.51, we have:

$$t_{\mathrm{NS}} = t_{\mathrm{det}} - t_0 + \Delta_{\mathrm{R}_\odot}(t_{\mathrm{det}}) + \Delta_{\mathrm{E}_\odot}(t_{\mathrm{det}}) - \Delta_{\mathrm{S}_\odot}(t_{\mathrm{det}}) \tag{1.52}$$

The phase at the detector at time t_{det} is therefore equal to the phase emitted at the source at time $t_{\mathrm{NS}}(t_{\mathrm{det}})$.

$$\phi(t_{\mathrm{det}}; \vec{\lambda}) = 2\pi \sum_{k=0}^{k_{\mathrm{max}}} f_{\mathrm{GW}}^{(k)} \frac{t_{\mathrm{NS}}(t_{\mathrm{det}})^{k+1}}{(k+1)!} \tag{1.53}$$

$\vec{\lambda}$ is introduced here to denote all the phase parameters; which in case of isolated sources ar $\{f_{\mathrm{GW}}^{(k)}, \alpha, \delta\}$, where $k \in \{0, 1, 2, ...k_{max}\}$.

The strain measured at the detector then can be expressed as a linear combination of

the antenna pattern function $(F_+, F_\times)$ and the two polarisations $(h_+, h_\times)$. We will here consider the special case of a non-precessing triaxial NS to write the strain scalar at the detector.

$$h(t; \vec{\mathcal{A}}, \vec{\lambda}) = F_+(t; \alpha, \delta, \psi) A_+ \, \cos(\phi_0 + \phi(t; \vec{\lambda})) + F_\times(t; \alpha, \delta, \psi) A_\times \, \sin(\phi_0 + \phi(t; \vec{\lambda})).$$
$$(1.54)$$

$\vec{\mathcal{A}}$ is the amplitude parameters vector $\{h_0, \iota, \psi, \phi_0\}$ [11]. Here the two polarization amplitudes $(A_+, A_\times)$ are related to the typical strain (Eq. 1.39) and the inclination angle, ι, between the spin axis of the source and the line of sight direction $\hat{n}$:

$$A_+ = \frac{1}{2} h_0 (1 + \cos^2\iota)$$
$$A_\times = h_0 \, \cos\iota \qquad\qquad (1.55)$$

The strain expressed in Eq. 1.54 has a few salients feature that are worth noting here. In the detector frame, the amplitude of the signal is modulated by the time dependent antenna pattern functions, a feature unique to long lasting signal.

Furthermore, since the phase at the detector has Solar System Rømer delay of the form $\Delta_{R_\odot} = \frac{\vec{r}(t_{\text{det}}) \cdot \hat{n}}{c}$, it is Doppler modulated, mainly due to two reasons.

- At the timescale of a day, the position vector of the detector, $\vec{r}(t_{\text{det}})$, changes periodically due to rotation of the Earth around its own axis.

- At longer timescales, $\vec{r}(t_{\text{det}})$ changes due to the revolution of Earth around the SSB.

The discussion above highlights the key features of CW signals, emphasizing their quasi-monochromatic nature, phase evolution, and amplitude modulation due to detector motion. Despite their intrinsic weakness, CW signals allow for coherent integration over extended periods due to slow variation in their frequency. However, this also necessitates precise modeling of phase evolution and Doppler shifts to maintain phase coherence. In the next section, we present different searches tailored for CW signals and the current status of observation.

---

[11] Notice that the reference phase ϕ_0 is conventionally treated as an amplitude parameter since it can be factored out of the phase that appears in Eq. 1.54

1.4.4 Status of current CW searches

CW searches typically have to cover phase parameter space of $\{f_{\text{GW}}^{(k)}, \alpha, \delta\}$ [12], while the amplitude parameters can be analytically maximized over [43, 122]. At first glance, since the dimensionality of the parameter space is less than CBC and the signal model is simpler, it might create an illusion to the reader that this shouldn't be a problem. However, since CWs are intrinsically weak, one needs to integrate over longer period to gain any significant detection statistics. Such long integration would also come at the cost of fine sampled Doppler parameters exploding the number of "templates" one needs to search for. The optimal match-filtering technique for all the phase parameters wouldn't be feasible given computational limitations. One trade-off made is to compromise search sensitivity, or in other words compute sub-optimal detection statistics, in order to search for wide parameter space. Generally, the strain time-series is divided into smaller chunks. The optimal/coherent statistics are evaluated for each chunk individually and then incoherently summed across the entire search duration. This also forms the basis for categorizing different CW searches, based on prior understanding of the desired search parameters. The different searches by the LVK and other CW groups are:

(a) Upper limit on strain from directed search towards the Galactic Center in O3 run of LVK at confidence level of 95%

(b) Corresponding 95% upper limit on ellipticity ϵ assuming a distance of 8 kpc. The shaded region correspond to the range of moment of Inertia $1 - 5 \times 10^{38}$kg.m^2
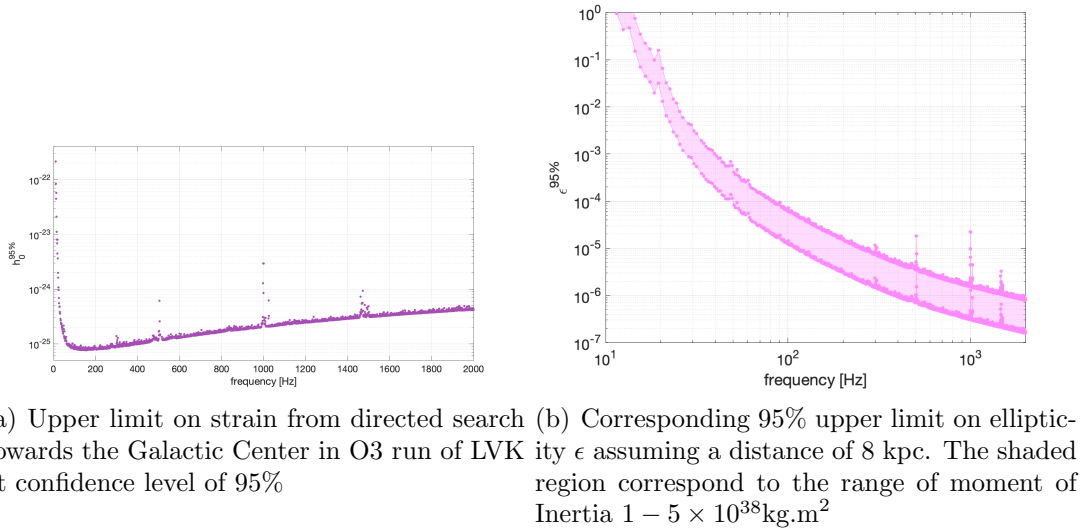
Figure 1.7: Strain upper limit plots, taken from [4]

---

[12]Additionally binary orbit parameters for NSs orbiting a companion

Targeted searches towards known pulsars

For pulsars, whose frequency, spin-downs and sky location are already known from electromagnetic observation, the GW search parameter is then just one template [123, 124]. In this case, it is possible to do a fully match-filtering search over the entire observation period with the assumption that CW signals are phase locked with electromagnetic emission.

Narrow-band searches

These searches also traditionally target known pulsars, but relaxes the assumption of phase locking between electromagnetic signal and the GW counterpart [125]. While the sky position is fixed towards the target, they cover a small width around the known spin parameters $\{f_{\mathrm{GW}}^{(k)}\}$ for robustness.

Directed searches

Certain hot-spots in the sky, such as the Galactic Center which can host multiple unobserved NSs [4], low mass X-Ray Binaries such as Scorpius-X1 with unknown spin [126–128], Globular Clusters [129], or central compact objects, likely NSs, born in core collapse supernova [130–133] make for interesting regions to look for CWs. Therefore, a widely used approach is to fix the sky location to these sources and search across the spin parameters.

All Sky Searches

These are completely blind searches over the entire parameter space $\{f_{\mathrm{GW}}^{(k)}, \alpha, \delta\}$ for isolated NSs and additional binary orbital parameters for NSs with companions [134–136]. As pointed earlier, to establish such large breadth of search parameters, these need to compromise on search sensitivity.

We have only broadly classified searches above without detailing the different search algorithms employed. We suggest the reader to refer to cited articles to learn about searches in detail.

Although no confident detection for CWs have thus far been reported, non-detections are generally used to put upper limit on the strain amplitude h_0 and subsequently on

ellipticity parameter ϵ. For illustration, figure 1.7 shows the latest upper limits placed on CW strain from the inner parsec regions of the Galactic Center. We will abide by these upper limits even when choosing optimistic amplitude parameters in this thesis.

1.5   Outline

The remaining thesis is structured as follows. Chapter 2 gives a brief summary of Gravitational Lensing of GWs. Chapter 3 discusses the prospects of observing CWs from spinning non-axisymmetric NSs lensed by the Galactic Supermassive BH, Sgr A*. In Chapter 4, we employ Bayesian parameter estimation and the Fisher matrix technique to forecast our ability to extract properties of Sgr A*, including its mass and the proper motion velocity of the source, using future observations of lensed CWs. Chapter 5 presents a summary of the thesis and scope for future work. It also discusses certain limitations of our analysis and challenges in detecting lensed CWs, particularly phase and amplitude modulation due to interference from multiple copies of the signal, leading to mismatches in conventional CW searches.

Chapter 2

Gravitational lensing of gravitational waves

2.1 Introduction

While discussing the foundational principles for GWs in the previous chapter, we restricted ourselves to the framework of linearized theory with a flat background metric, $\eta_{\mu\nu}$. In the current chapter, we extend our discussion to the effect of the background curvature on GW propagation. This extension is motivated by the fact that GWs, while traveling from the source to detector, may encounter massive astronomical objects along their paths and be affected by the spacetime curvature they produce. This interaction results in a phenomenon called gravitational lensing which can deflect, magnify, and delay the propagating waves. In the case of strong lensing, this also leads to multiple copies of the same signal where their wavefronts arrive with a time delay.

We discuss the framework for these effects step by step. First, we derive the equation of motion for $h_{\mu\nu}$ in a general curved background, $\bar{g}_{\mu\nu}$, adopting the choice of Lorentz gauge. Consequently, we learn that lensing preserves the transverse nature of individual GW polarizations and parallel-transport them, allowing us to describe these propagation effects using scalar waves. We then formulate the problem in terms of the governing lens equation in the geometric optics limit, which provides the framework for analyzing the deflection and magnification of GWs as they propagate through curved spacetime. Next, we focus on a specific model for the intervening mass — the point mass model — which is particularly relevant to this thesis. We derive its governing equation and

associated lensing effects. Finally, we comment on the current observational status of strong lensing of GWs and science case for such detections. This chapter is based on discussions in [20, 137, 138].

2.2 Gravitational Lensing in GR: Theory

Similar to our treatment in section 1.1.1, we begin by writing the spacetime metric but now around a general metric $\bar{g}_{\mu\nu}$ instead of $\eta_{\mu\nu}$,

$$g_{\mu\nu} = \bar{g}_{\mu\nu} + h_{\mu\nu}. \tag{2.1}$$

As a first specification, we restrict ourselves to the macroscopic description of the system by assuming the following hierarchy of scales in the problem.

$$h \ll \frac{\lambdabar}{L_B} \ll 1, \tag{2.2}$$

where h is the trace of the metric perturbation and represents the approximate strain amplitude. $\lambdabar = \frac{\lambda}{2\pi}$ denotes the reduced wavelength of the perturbation, $h_{\mu\nu}$, and L_B is the length scale of the background curvature. In this regime, the background curvature is not significantly influenced by the microscopic metric perturbations themselves (e.g., see Section 1.5 of [20]).

Our goal is to derive a wave equation analogous to Eq. 1.5, but in a curved background. One major difference here is the need for covariant formalism. We use the affine connections (Christoffel symbols) to define derivatives instead of the partial derivatives, as in the Minkowskian metric where the Christoffel symbols vanish. The covariant derivative is defined as:

$$\nabla_\lambda X_{\mu\nu} = \partial_\lambda X_{\mu\nu} - \Gamma^\sigma_{\lambda\mu} X_{\sigma\nu} - \Gamma^\sigma_{\lambda\nu} X_{\mu\sigma}, \tag{2.3}$$

where the Christoffel symbol takes the form:

$$\Gamma^\lambda_{\mu\nu} = \frac{1}{2} g^{\lambda\sigma} \left(\partial_\mu g_{\sigma\nu} + \partial_\nu g_{\sigma\mu} - \partial_\sigma g_{\mu\nu} \right) \tag{2.4}$$

To leading order in h and next-to-leading order in $\frac{\lambdabar}{L_B}$, the Ricci tensor outside the matter

sources again vanishes, i.e., $R_{\mu\nu} = 0$. This leads to the equation: [20]

$$\bar{g}^{\rho\sigma} \left(\bar{\nabla}_\rho \bar{\nabla}_\nu h_{\mu\sigma} + \bar{\nabla}_\rho \bar{\nabla}_\mu h_{\nu\sigma} - \bar{\nabla}_\nu \bar{\nabla}_\mu h_{\rho\sigma} - \bar{\nabla}_\rho \bar{\nabla}_\sigma h_{\mu\nu} \right) = 0. \tag{2.5}$$

Note that both the covariant derivative, $\bar{\nabla}$, and the index contraction are with the metric $\bar{g}_{\mu\nu}$.

Similar to section 1.1.1, working with the trace-reversed metric $\bar{h}_{\mu\nu} \equiv h_{\mu\nu} - \frac{1}{2}\bar{g}_{\mu\nu}h$ with trace $h \equiv \bar{g}^{\mu\nu}h_{\mu\nu}$ and imposing the Lorentz Gauge condition:

$$\bar{\nabla}^\mu \bar{h}_{\mu\nu} = 0, \tag{2.6}$$

we obtain the wave equation:[1]

$$\bar{\nabla}^\rho \bar{\nabla}_\rho \bar{h}_{\mu\nu} = 0. \tag{2.7}$$

This is the generalization of the linearized wave equation 1.5, but with the d'Alembert operator, $\Box \equiv \partial^\rho\partial_\rho$, replaced by $\bar{\nabla}^\rho\bar{\nabla}_\rho$. This generalization should however be treated with caution, and is not true for all background spacetime —particularly for those where the scale hierarchy in Eq. 2.2 is not satisfied. In these cases, where the perturbation wavelength λ is not well separated from the background curvature scale L_B, the distinction between the background and GWs become ambiguous. In such regimes, the leading-order approximation that led to Eq. 2.7 breaks down, and the wave equation cannot be reliably written in the same form as in flat spacetime with $\partial_\mu\partial^\mu \to \nabla_\mu\nabla^\mu$.

To study propagation effects on the metric tensor, $h_{\mu\nu}$, we make the Eikonal approximation for GWs under the assumption that the amplitude, wavelengths, and the polarization of the wave vary on a larger scale as compared to its phase which varies on the scale of the wavelength λ, i.e.

$$\bar{h}_{\mu\nu}(x) = \left[A_{\mu\nu}(x) + \varepsilon B_{\mu\nu}(x) + \dots \right] e^{i\theta(x)/\varepsilon}. \tag{2.8}$$

Here, $\epsilon \equiv \frac{\lambda}{L_B}$, is a fictitious parameter to denote the difference in scale over which amplitudes and phase change. We define the wave vector, $k_\mu \equiv \partial_\mu\theta$ and express the

---

[1]Here, we have ignored higher-order $\frac{h}{L_B^2}$ and $\frac{h}{\lambda^2}$ terms of the Ricci Tensor, in line with the hierarchy of scales in Eq. 2.2.

tensor amplitude $A_{\mu\nu}$ as a product of a scalar amplitude A and polarization tensor $e_{\mu\nu}$, i.e., $A_{\mu\nu} = A e_{\mu\nu}$. Using this ansatz in the Lorentz gauge condition (Eq. 2.6) and the wave equation (Eq. 2.7), we obtain:

$$k^{\mu} e_{\mu\nu} = 0 \tag{2.9}$$

$$k^{\mu} \bar{\nabla} e_{\mu\nu} = 0 \tag{2.10}$$

Equations 2.9 and 2.10 imply that GW polarizations remain transverse and are parallel transported along null geodesics. Therefore, lensing does not alter the polarization tensor, which allows us to express the perturbation as:

$$h_{\mu\nu} = \phi \, e_{\mu\nu}, \tag{2.11}$$

and solely study lensing effects on the scalar wave, ϕ. The wave equation for the scalar ϕ, derived from Eq. 2.7, is:

$$\partial_{\mu} \left(\sqrt{-\bar{g}} \, \bar{g}^{\mu\nu} \partial_{\nu} \phi \right) = 0 \tag{2.12}$$

2.3 The amplification factor

Assuming a weak-field approximation of the background metric,

$$\bar{g}_{\mu\nu} = \begin{bmatrix} -(1 + 2U) & 0 \\ 0 & (1 - 2U)\delta_{ij} \end{bmatrix}, \tag{2.13}$$

where U is the Newtonian potential ($U \ll 1$), the frequency domain equation for $\tilde{\phi}(f, r)$ to leading order in U is given by:

$$(\Delta + \omega^2)\tilde{\phi}(f, r) = 4\omega^2 U \tilde{\phi}(f, r), \tag{2.14}$$

where Δ is the Laplacian operator and $\omega = 2\pi f$. In the absence of the lens ($U = 0$), this simplifies to the standard wave equation in Euclidean space. The effect of lensing can be quantified by using the amplification $F(f, r) = \frac{\tilde{\phi}(f,r)}{\tilde{\phi}_0(f,r)}$, where $\tilde{\phi}_0(r)$ represents the
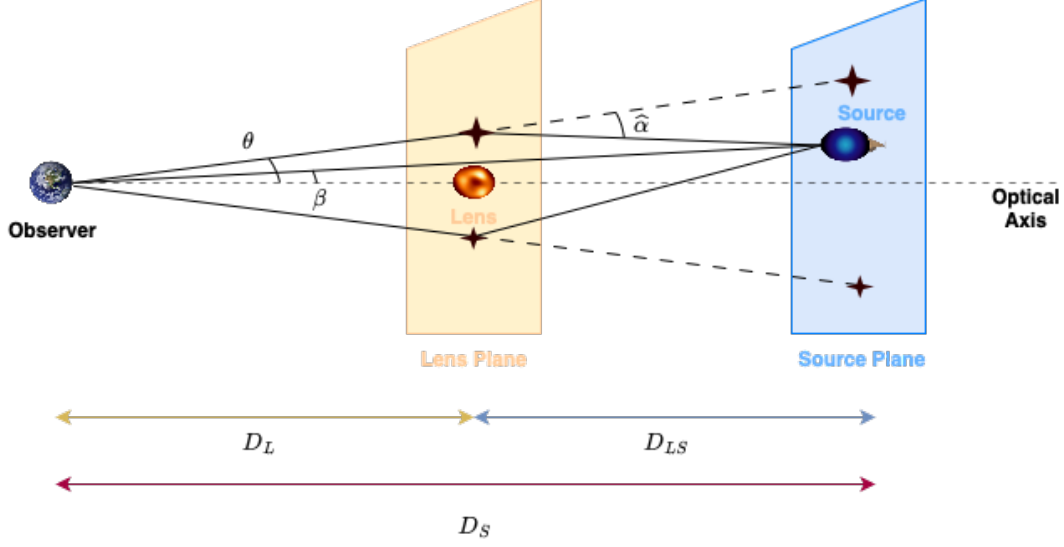
Figure 2.1: Schematic representation of gravitational lensing in the thin-lens approximation. The diagram illustrates the bending of GWs or electromagnetic waves due to an intervening mass, referred to as the lens. The optical axis passes through the observer and the lens. The source is located in the source plane (blue) and the lens in the lens plane (orange). The true position of the source is at an angular position β, while the lensing causes the observed image to appear at an angular position θ due to the deflection by an angle $\hat{\alpha}$. Distances between the observer and the lens (D_L), the lens and the source (D_{LS}), and the observer and the source (D_S) are indicated in the diagram.

unlensed solution ($U = 0$). The thin-lens approximation is commonly used to compute $F(f)$. This assumes that the lens is localized in a 2D plane rather than being extended in three dimensions. This assumption is reasonable because astrophysical lenses, such as galaxies or compact objects, are much smaller compared to the distances between the observer, the lens, and the source. An illustrative case is shown in Figure 2.1.

Under this scheme, the amplification factor $F(f)$ can be written using the Kirchhoff diffraction integral [137]:

$$F(f) = -\iota \frac{D_L D_S}{c D_{LS}} f \int d^2\vec{\theta}\, e^{2\pi \iota f t_d(\vec{\theta}, \vec{\beta})}. \tag{2.15}$$

Here, $\vec{\beta}$ and $\vec{\theta}$ are the angular positions of the source and the image, respectively, defined relative to the optical axis. The integral sums over all image positions in the lens plane, incorporating the phase delays introduced by the lens. The term $t_d(\vec{\theta}, \vec{\beta})$ represents the

time delay and is given by:

$$t_d(\vec{\theta}, \vec{\beta}) = \frac{D_L D_S}{c D_{LS}} \left[\frac{(\vec{\theta} - \vec{\beta})^2}{2} - \psi(\vec{\theta}) \right]. \tag{2.16}$$

The first term corresponds to the geometric time delay due to the path difference between the lensed and unlensed rays. The second term arises from the two-dimensional deflection potential caused by the gravitational field of the lens and is often referred to as the Shapiro delay.

The deflection potential $\psi(\vec{\theta})$ is the projection of the Newtonian potential U onto the lens plane. It is related to the two-dimensional surface mass density of the lens, $\Sigma(\vec{\theta})$, by:

$$\psi(\vec{\theta}) = \frac{1}{\pi \Sigma_{cr}} \int d\vec{\theta}' \, \Sigma(\vec{\theta}') \ln |\vec{\theta} - \vec{\theta}'| \tag{2.17}$$

Here, $\Sigma_{cr} = \frac{c^2 D_S}{4 \pi G_N D_{LS} D_L}$ represents the critical mass density. The significance of the thin-lens approximation becomes evident at this stage, as it allows us to work with the surface mass density rather than the full three-dimensional mass distribution, ρ.

$$\Sigma(\vec{\theta}) = \int_0^\infty dz \, \rho(z, \vec{\theta}), \tag{2.18}$$

where z is the line of sight distance along the optical axis. Equation 2.15 represents the full wave optics solution, and in principle, solves for the amplification factor given a source at an angular position $\vec{\beta}$, a lens with a surface mass distribution $\Sigma(\vec{\theta})$, and the distances between the observer and the lens (D_L), the lens and the source (D_{LS}), and the observer and the source (D_S).[2] For a point-mass lens, the integral has a closed-form solution. However, for more general lens models without analytical solutions, traditional numerical integration techniques often fail due to the highly oscillatory nature of the integrand. In the next section, we discuss the geometric optics approximation for computing the amplification factor.

---

[2] For cosmological distances, an additional factor of $(1 + z_L)$ appears in Equations 2.15 and 2.16, and the distances are defined as angular diameter distances. However, since this thesis focuses on lensing within our galaxy, we assume $z_L = 0$.

2.4 Geometric optics limit

As discussed earlier, the amplification factor in the wave optics regime, given by the Kirchhoff diffraction integral, doesn't have a closed-form solution in general. However, in the geometric optics limit, when wavelength λ is much smaller than the lens' characteristic size — such as its Schwarzschild radius, $\frac{2G_N M}{c^2}$ — the integral is dominated by stationary points of the exponent, $\partial_{\vec{\theta}} t_d(\vec{\theta}, \vec{\beta}) = 0$, also known as the Fermat principle of least time. In this regime, waves behave like rays that are deflected by the lens. For ground based GW observatories, where wavelengths lie between $\mathcal{O}(10^4)$ and $\mathcal{O}(10^7)$ m, the geometric optics approximation holds for lens masses exceeding $10^4 M_\odot$.[3] This consideration leads us to the lens equation:

$$\partial_{\vec{\theta}} t_d(\vec{\theta}, \vec{\beta}) = 0 \tag{2.19}$$

$$\implies \vec{\beta} = \vec{\theta} - \partial_{\vec{\theta}} \psi. \tag{2.20}$$

Equation 2.20 can also be derived from the schematic diagram (Figure 2.1). The image position $\vec{\theta}$ is related to the source position $\vec{\beta}$ and the scaled deflection angle $\vec{\alpha}$ as follows:

$$\vec{\theta} = \vec{\beta} + \vec{\alpha}(\vec{\theta}), \tag{2.21}$$

where the scaled deflection angle is defined as

$$\vec{\alpha} \equiv \frac{D_{LS}}{D_S} \hat{\alpha}. \tag{2.22}$$

From Eqs. 2.20 and 2.21, it follows that

$$\vec{\alpha}(\vec{\theta}) = \partial_{\vec{\theta}} \psi. \tag{2.23}$$

For strong lensing, the lens equation (Eq. 2.20) may admit multiple solutions for $\vec{\theta}$, meaning that a single source at $\vec{\beta}$ can produce multiple images, where the wavefronts arrive with a time delay. Often in the case of transients, the time delay between the images

---

[3]For electromagnetic waves, which have much shorter wavelengths, the geometric optics approximation remains valid for significantly smaller lens masses. This transition from wave optics to geometric optics is an important distinction between the lensing of GWs and electromagnetic waves.

is greater than the in-band time of the events, leading to two or more temporally resolved copies of the same signal. Another consequence of strong lensing in the geometric optics limit is that individual images have different magnifications, given by the inverse Jacobian of the lens mapping in Eq. 2.20. For the i-th image at location $\vec{\theta}_i$, the corresponding magnification is:

$$\mu_i = \left| \frac{\partial \vec{\beta}}{\partial \vec{\theta}_i} \right|^{-1}. \tag{2.24}$$

In the geometric optics limit, the Kirchhoff diffraction integral picks up the contribution from individual images:

$$F(f) = \sum_i |\mu_i|^{\frac{1}{2}} e^{\left(2\pi \iota f t_d(\vec{\theta}_i, \vec{\beta}) - \mathrm{sign}(f) n_i \pi \right)}. \tag{2.25}$$

Here, n_i is the Morse index with $n_i = 0, 0.5, 1$ for the minima, saddle point and maxima of the time delay, respectively. We have laid out the formalism for discussing lensing for a general lens model characterized by their surface mass density. The image positions, magnifications, and time delays are dictated by the specific mass distribution of the lens. In the next section, we derive the lensing properties of the point mass model in geometric optics limit.

2.5 Point Mass Model

The point mass model [139–141] is commonly used for lensing by compact objects, such as black holes, where the surface density for a M_L mass lens is well represented by the Dirac-delta function:

$$\Sigma(\vec{\theta}) = M_L \delta^{(2)}(\vec{\theta}). \tag{2.26}$$

This is one of those cases where the Kirchhoff diffraction integral has an analytical solution for the amplification factor [137]. In this section, we derive the geometric optics solution for the model. Using the Dirac delta mass profile in Equations 2.17 and 2.23, the scaled deflection angle is given by:

$$\vec{\alpha} = \frac{4 G_N M_L D_{LS}}{c^2 D_L D_S} \frac{\vec{\theta}}{\theta^2}. \tag{2.27}$$

The angular scale $\sqrt{\frac{4G_N M_L D_{LS}}{c^2 D_L D_S}}$ is known as the Einstein angle, denoted by θ_E. Using the expression for the scaled deflection angle, the lens equation for the point mass lens becomes:

$$\vec{\beta} = \vec{\theta} - \frac{\theta_E^2}{\theta^2}\vec{\theta} \tag{2.28}$$

It is conventional to express the lens equation in terms of dimensionless image and source location on the lens plane, $\vec{x} \equiv \frac{\vec{\theta}}{\theta_E}$ and $\vec{y} \equiv \frac{\vec{\beta}}{\theta_E}$, respectively. This leads to:

$$\vec{y} = \vec{x} - \frac{\vec{x}}{x^2} \tag{2.29}$$

A notable feature in Equation 2.28 is that $\vec{\beta}$ and $\vec{\theta}$ are collinear, meaning the images lie along the same direction as the source position on the lens plane. Using this, we can solve for the image location given the source location following the scalar equation:

$$\beta = \theta - \frac{\theta_E^2}{\theta} \tag{2.30}$$

Since this is a quadratic equation in θ, it has two solutions, denoting the image positions of two images formed due to lensing by a point mass,

$$\theta_{\frac{1}{2}} = \frac{\beta}{2}\left[1 \pm \sqrt{1 + \frac{4\theta_E^2}{\beta^2}}\right]. \tag{2.31}$$

The individual magnifications of the two images, computed as the inverse Jacobian of transformation between $\vec{\beta}$ and $\vec{\theta}$ (Equation 2.24), are given by:

$$\mu_{\frac{1}{2}} = \left[1 - \left(\frac{\theta_E}{\theta_{\frac{1}{2}}}\right)^4\right]^{-1}. \tag{2.32}$$

To emphasize strong lensing by a point mass lens, we re-express the magnification in terms of the dimensionless variable, $y \equiv \frac{\beta}{\theta_E}$,

$$\mu_{\frac{1}{2}} = \frac{1}{4}\left(\frac{y}{\sqrt{y^2 + 4}} + \frac{\sqrt{y^2 + 4}}{y} \pm 2\right). \tag{2.33}$$

The magnifications of the individual images are monotonically decreasing functions of y, implying higher magnifications for sources aligned close to the optical axis. As $y \to \infty$, $\mu_1 \to 1$ and $\mu_2 \to 0$. At $y = 1$, the magnification of the second image, $|\mu_2|$ falls below 0.17, making the signal considerably weaker. Therefore, $y < 1$ or $\beta < \theta_E$, is often used to demarcate the strong lensing regime for point mass lenses. We will utilize this feature in Chapter 3 to discuss strongly lensed sources.

The point mass lens model suffices to describe lensing by BHs and serves the purpose for this thesis. To characterize lensing by extended sources such as galaxies or dark matter halos, the Singular Isothermal Sphere and Singular Isothermal Ellipsoid are commonly used models [142]. For further discussions on these models, we refer the readers to [143–147].

2.6   Strong lensing of GWs

Arthur Eddington's 1919 solar eclipse expedition provided one of the earliest observations of gravitational lensing by measuring the deflection of starlight weakly lensed by the Sun and significantly contributing to the early acceptance of GR. The first confirmed case of gravitational lensing by a galaxy was reported by Walsh, Carswell, and Weymann in 1979, who observed the doubly imaged quasar Q0957+561A,B during an optical follow-up of a radio source [148]. Shortly thereafter, in 1980, a quadruply imaged quasar, PG 1115+080, was discovered at a redshift of 1.72, with its lensing galaxy at z = 0.31 [149]. Since then, electromagnetic observations have identified several such lensed systems, where the background galaxies or quasars appear as distinct images or are distorted as arcs or Einstein rings. Similar to electromagnetic signals, GWs can also be lensed by intervening masses. In case of transient events from CBCs, strong lensing by galaxies or galaxy clusters can form multiple temporally separated copies of the same event. As discussed earlier, in the geometric optics regime, these images will have similar phase evolution, but different amplitudes due to the varying magnifications. Moreover, unlike electromagnetic sources, which are well localized, our ability to localize GW transients is not good enough to distinguish their sky positions [4]. This also forms basis for many searches for lensed CBCs, which rely on overlapping sky area and consistent phase evolution across events

---

[4]This is not always the case for CWs, where the angular resolution for long integration time are much better than CBCs

to classify or reject them as lensed images. For example, the Posterior Overlap method performs hypothesis tests for the unlensed vs lensed hypothesis by comparing the Bayesian posterior distributions across pairs of events [150]. Another pipeline, the joint PE method, samples the joint likelihood across two data streams to estimate the lensing probability [151, 152]. Machine learning methods, such as those in [153], search for identical phase evolution with the time-frequency maps (Q-transforms [154]) and the Bayestar skymaps [155] of the events.

Although there has yet to be a confident detection of the gravitational lensing of GWs [156] [5], there is a growing consensus in the literature that lensed GWs from merging BBHs are likely to be detected in the upcoming observing runs of LIGO, Virgo, and KAGRA (see e.g., [158]). Observing such events will provide additional insights into various aspects of astrophysics, cosmology and fundamental physics. Apart from being the very first detection of gravitational lensing involving a new messenger, they will enable accurate localization of the host galaxy of the merger [159], provide unique constraints on the constituents of dark matter [160–162], on models of the populations of galaxies and galaxy clusters [163], and on alternative theories of gravity [164–166]. Even the non-observation of lensing signatures has been instrumental in placing several astrophysical constraints, such as limits on abundance of compact objects as dark matter [162, 167], formation channels of BBH mergers [168], and the CBC merger rate density at high redshifts [169].

---

[5]Note, however, that some tantalizing candidates of lensed GW signals have been proposed; see, e.g., [157].

Chapter 3

Prospects for detecting lensed continuous gravitational waves

3.1 Introduction

Gravitational lensing has been a powerful tool in electromagnetic astronomy, offering insights into dark matter distribution in the universe [170, 171], cosmic expansion [172, 173], and structure of distant galaxies [174] and clusters [175]. Additionally, it has also emerged as a novel test of GR [176]. As discussed in chapter 2, similar to light, GWs are also lensed by the intervening masses [137, 177–179]. Recent estimates suggest that a small fraction ($< 1\%$) of BBH mergers may be strongly lensed by intervening galaxies [158]. The LVK collaboration has detected $\mathcal{O}(100)$ events until their O3 run, while the current observing run (O4) has already observed 200 more events. In the third-generation (3G) era, the BBH detection rate is projected to reach $10^5 - 10^6$ per year [180]. As the catalog of GW events continues to grow with increasing sensitivity of the detectors, the first observations of strongly lensed GWs —likely from merging binaries —are expected in the near future. Such detections will mark a new era of astronomy, complementing the current probes from the electromagnetic front. These scenarios have already been explored extensively in research on lensing of CBCs (see, e.g., [166, 181–184] for tests of GR with lensed GWs, [185–187] for precision cosmology with strongly lensed GWs, and [159] for accurate localization of lensed events).

However, lensing of CWs —long lived monochromatic signals such as from spinning non-

axisymmetric NSs —remain almost unexplored in the literature. This is mostly a consequence of the horizon distance for CWs being limited to within our Galaxy or its immediate vicinity, unlike the loud transient CBCs originating from cosmological distances. Despite strong lenses being scarce in our galaxy, one promising lens is the Galactic supermassive BH (SMBH), Sgr A*, discovered as a radio source by Balick and Brown in 1974 [188]. Follow up studies on periodic stellar orbits around the Galactic center ascertained its nature as a supermassive compact object [189, 190], and estimated its mass to be around $4.15 \times 10^6 M_\odot$ [191]. More recently, the Event Horizon Telescope provided the first direct image of Sgr A*, revealing its shadow and surrounding accretion flow [192]. Searches for CWs directed towards the Galactic center [4] probe a region where strong gravitational lensing could play an important role as some of the NSs beyond Sgr A* may lie close to the optical axis —the line connecting the Earth and the lens (Sgr A*) —making them strong lensing candidates. Motivated by this, we explore the prospects of observing the gravitational lensing of CWs from spinning NSs by the Galactic SMBH in this chapter.

3.2 Method

In this section, we outline the method adopted in this chapter and then discuss them in more detail in the following sections. Focusing exclusively on strong lensing, we expect the CWs to be lensed if the source NS resides within the Einstein angle of the lens, as discussed in section 2.5. Assuming the SMBH to be a point mass lens, strong lensing will produce two copies of a CWs, with a time delay between them [1]. This arises because, in the geometric optics limit, the lens equation for a point mass lens has a quadratic form and admits two solutions (see Eq. 2.30), corresponding to two distinct images. The copies will have different amplitudes, although their time-dependent phase will be identical. Unlike CBCs, where the time delay results in separate events, the lensed CW images are persistent, and the time delay results in a phase shift between the two images. The image waveforms will therefore appear in the detector as one superposed CW, whose amplitude will depend on the magnifications of the images as well as the time-delay between

---

[1]CWs from rapidly spinning NSs, with spin frequencies spanning $\sim 10 - 1000$ Hz, have wavelengths that are $\mathcal{O}(10^2 - 10^4)$ times smaller than the Schwarzschild radius of the Galactic SMBH. The geometric optics approximation therefore holds for the lensing scenario considered here.

the two copies of the signal at the detector[2].

The number of NSs that are expected to lie within the Einstein angle of the SMBH will depend on the (poorly known) spatial distribution of NSs in the galaxy. We consider various astrophysically motivated distributions presented in the literature, and evaluate the distribution of the number of NSs that fall within the Einstein angle, assuming a total of 10^9 NSs in the galaxy [193]. We find that up to 6 NSs will be within the Einstein angle of the SMBH, so their CWs, if detected, will be strongly lensed.

We further assess the detectability of these signals by 3G GW detector network consisting of two Cosmic Explorers [194] and one Einstein Telescope [55], incorporating the effects of lensing magnification and time delays. The detectability, characterized by the signal-to-noise ratio (SNR), is proportional to their amplitude, as well as the square root of the observation time [43]. The CW amplitude, in turn, is proportional to the ellipticity, the moment of inertia, and the square of the spin frequency of the NS apart from extrinsic parameters such as the location and orientation (see discussion in section 1.4.2).

We assume an ellipticity of 10^{-7}, which is an order of magnitude smaller than the best upper limits obtained from a directed search for NSs towards the Galactic center, for a fiducial moment of inertia of 10^{38} kg m^2 [195]. Spin frequencies are drawn from the spin distribution of known pulsars [8]. The signal amplitude is averaged over the inclination angle of the NS's rotation axis with respect to the line of sight, over the angle between the rotation axis and the axis of symmetry, as well as the polarization angle. Using a single template search (i.e., assuming that the source parameters are known a priori) the probability of detecting at least one lensed CW signal at 1% false alarm rate (FAR) is $\sim 0 - 15\%$ $(2 - 53\%)$ in LIGO-Virgo (third generation detectors). For a more realistic, directed search towards the Galactic center using $\sim 10^{12}$ templates [196], the corresponding probability is $\sim 0 - 2\%$ $(2 - 51\%)$. Note that the ellipticity of most NSs could be

---

[2]Proper motion of NSs induces distinct phase evolution for the individual images, producing beating patterns in the superposed signal. Additionally, the spin-down of the NS during the time delay can also introduce a slight frequency difference between the two images, resulting in similar beating patterns. However, for time delays of order $\mathcal{O}(10)$–$\mathcal{O}(100)$ seconds, the contribution from spin-down is subdominant compared to the effect of the source's proper motion. Since this chapter focuses specifically on the astrophysical viability of detection, we defer a detailed discussion of these waveform modulations to later chapters.

much lower. For a more conservative assumption of $\epsilon = 10^{-8}$, LIGO-Virgo detectors are unlikely to detect any lensed signals. In 3G detectors the detection probability is $\sim 1 - 36\%$ ($\sim 0 - 18\%$) at 1% FAR for single template search (10^{12} templates). If the ellipticity is lower than 10^{-8}, the detection probability will be even smaller, as would prospects for CW searches in general.

We detail these steps in the rest of the chapter. Section 3.3 revisits gravitational lensing by a point mass lens and describes the spatial distributions of NSs assumed, as well as the resulting estimate of the number NSs strongly lensed by the Galactic SMBH. Section 3.4 delineates the calculation of the SNR and provides the (SNR-threshold-dependent) probability of detecting a lensed CW in the 3G era. Section 3.5 summarizes the chapter, discusses potential waveform modulations of lensed CW signals, and outlines the possible astrophysical measurements that can be performed from such an observation.

3.3 Number of strongly lensed neutron stars

In section 2.5, we discussed lensing by a point mass lens in the geometric optics limit. Here, we first revisit some key aspects from that discussion. The strong lensing of GWs, in the geometric optics limit, is identical to that of the lensing of electromagnetic waves, and applies in general to null geodesics (see e.g. [197]). Thus, as with the gravitational lensing of light, the fundamental equation that governs strong lensing of GWs is the so-called lens equation, which relates the source location $\vec{\beta}$, with the image location $\vec{\theta}$, via a deflection angle $\vec{\alpha}(\vec{\theta})$

$$\vec{\beta} = \vec{\theta} - \vec{\alpha}(\vec{\theta}). \tag{3.1}$$

Note that $\vec{\beta}, \vec{\theta}$ are angles measured with respect to the line connecting the Earth and the lens, called the optical axis. A natural angular scale that emerges in the lensing by a point mass M_L is the Einstein angle, $\theta_E = \sqrt{\frac{4G_N M_L D_{LS}}{D_S D_L}}$, such that the deflection angle $\vec{\alpha} = \frac{\theta_E^2}{\theta^2}\vec{\theta}$. Here, D_S, D_L are the distances (from Earth) to the source and the lens, respectively, and $D_{LS} = D_S - D_L$.[3] The Einstein angle can also be used to define dimensionless parameters, like the impact parameter, $y \equiv \frac{\beta}{\theta_E}$. With this parameterization, the magnifications of the

---

[3]Since the distances considered in this work are Galactic, cosmological effects are negligible. These distances can therefore be approximated to be Euclidean.
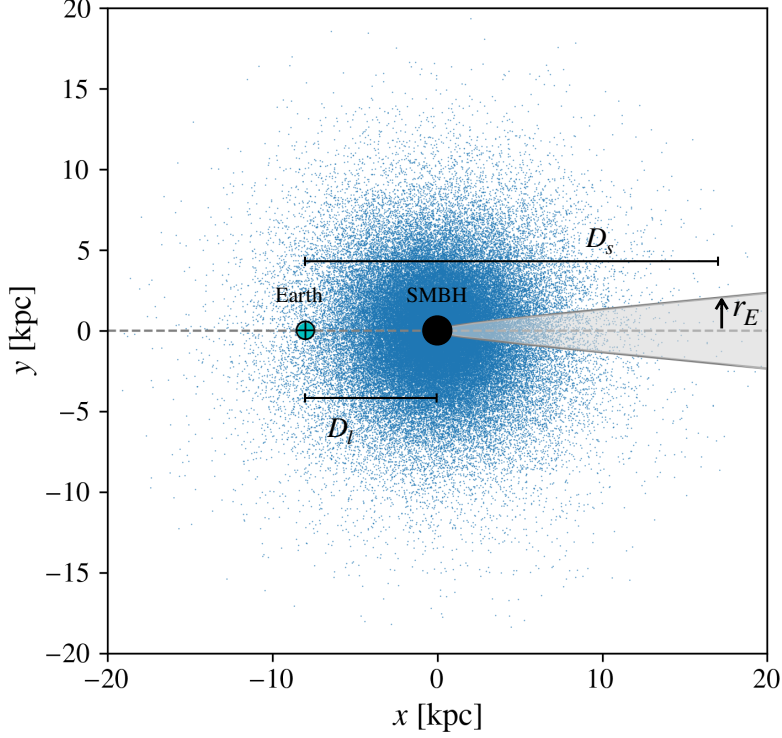
Figure 3.1: Schematic diagram of the distribution of NSs (blue dots) projected onto in our Galactic plane. The Einstein cone of the central SMBH is shown by the gray region (highly exaggerated). The NSs within the Einstein cone will be strongly lensed by the SMBH.

individual images can be expressed solely in terms of y:

$$\mu_{\substack{1\\2}} = \frac{1}{4}\left(\frac{y}{\sqrt{y^2+4}} + \frac{\sqrt{y^2+4}}{y} \pm 2\right). \tag{3.2}$$

For $y > 1$ i.e. $\beta > \theta_E$, the second image exists for the point mass model but is highly demagnified. Thus, we conservatively define the strong lensing regime as $\beta < \theta_E$. Investigating the prospects of detecting lensed CWs therefore involves counting the expected number of NSs within the Einstein angle of the SMBH and assessing the detectability of CWs produced by them. This requires assumptions on the total number of NSs in our galaxy and their spatial distribution. While it is generally believed that $\sim 10^9$ NSs reside in the our galaxy [193], only $\sim 10^3$ have been detected so far through electromagnetic observations. Thus, little is known about the statistical properties of Galactic NSs, including their spatial distribution.

We consider three types of spatial distribution of NSs in the galaxy. One assumes that NSs have the same distribution of stars in the young Galactic disk. Following [5], we write the

probability distributions in galactocentric cylindrical coordinates system (R, ϕ, z), where the z axis corresponds to the rotation axis of the Milky Way, as:

$$\frac{dP}{dR} = a_R \frac{R}{R_0^2} \exp\left(\frac{-R}{R_0}\right), \tag{3.3}$$

$$\frac{dP}{dz} = \frac{1}{2z_0} \exp\left(\frac{-|z|}{z_0}\right), \tag{3.4}$$

where $R_0 = 4.5$ kpc and $z_0 = 0.07$ kpc are scaling constants. We call this the "progenitor" model.

This will be a good approximation of the spatial distribution of the NSs if their natal kicks are small or when the NSs are young. However, the distribution of NSs can differ from that of stars depending on the NS birth velocities, which remains largely uncertain. To mimic the effect of natal kicks on the spatial distribution of NSs, some authors have considered different choices of z_0 in Eq.(3.4). For example, [7] uses a range of z_0 values out of which we choose four different values ($z_0 = 0.1, 0.2, 0.5, 1$ kpc) in Eq.(3.4) along with a Gaussian-like distribution in R.

$$\frac{dP}{dR} = \frac{R}{\sigma_R^2} \exp\left(\frac{-R^2}{2\sigma_R^2}\right), \tag{3.5}$$

where $\sigma_R = 5$ kpc. We refer to this class of models as Reed (z_0) models.

Several studies also have evolved populations of NSs in the Galactic potential by considering different models of the birth velocity to predict the expected distribution of NSs in the present epoch. [6] assumes that the NSs are born in the galaxy with a constant birth rate, at locations given by the progenitor distribution presented in Eqs.(3.3)-(3.4). They evolved this distribution under several different assumptions on their birth velocities (indicated by 1A, 1B, 1C, 1D, and 1E), and two different models of the Galactic potential (models with and without a "*"). By fitting their simulation data, [6] presented the following fitting functions:

$$\frac{dP}{dR} \propto R \exp\left(a_0 + a_1 R + a_2 R^2 + a_3 R^3 + a_4 R^4\right), \tag{3.6}$$

$$\frac{dP}{dz} \propto \frac{1}{b_0 b_1^z + b_2}, \tag{3.7}$$

where the fitting coefficients are tabulated in Tables A.1 and A.2 of [6].

For these models, we finally construct the 3-dimensional distribution

$$\frac{dP}{dRd\phi dz} = C \frac{dP}{dR} \frac{dP}{d\phi} \frac{dP}{dz},$$ (3.8)

where all models assume axial symmetry around the rotation axis of the galaxy ($dP/d\phi = 1/2\pi$). The distributions in [5] and [7] are already normalized; hence $C = 1$. For [6] models, the normalization constant C is determined by the condition that a certain fraction of the NSs presently resides in the disk of the galaxy.

$$\int_{R=0}^{R_{\rm disk}} dR \int_{\phi=0}^{2\pi} d\phi \int_{z=-z_{\rm disk}}^{z_{\rm disk}} dz \frac{dP}{dRd\phi dz} = f_{\rm disk}.$$ (3.9)

Above, $R_{\rm disk} = 20$ kpc and $z_{\rm disk} = 0.2$ kpc, while $f_{\rm disk}$ is given in Table 4 of [6].

One could distribute the entire population of NSs in the galaxy following the 3-dimensional distribution and search for lensed sources within the population. However, it is computationally expensive to simulate several realizations for such a large number of NSs. Since this is essentially a number-counting problem, we can use Poisson statistics to evaluate the distribution of lensed NSs. We therefore need to evaluate the average number of NSs that would be strongly lensed (producing multiple images) for each of the assumed distributions. In order to estimate that, we numerically integrate the probability $\frac{dP}{dR,d\phi,dz}$ over a cone-like region around the optical axis with a radius of $r_E \equiv \theta_E D_s$ (shaded region in Fig. 3.1), and multiply it by the total expected number of NSs in the galaxy ($N \sim 10^9$). We refer to this average as $\bar{N}_{\theta_E}$.

$$\bar{N}_{\theta_E} = N \int_{\rm lensing\ cone} dRd\phi dz \frac{dP}{dRd\phi dz}.$$ (3.10)

Depending on the distribution $\bar{N}_E$ varies from 0.1 to 5.6. Assuming no spatial clustering of NSs, the actual number, N_{θ_E}, of NSs that will be strongly lensed by the SMBH will be distributed according to a Poisson distribution with mean $\bar{N}_{\theta_E}$:

$$P(N_{\theta_E} = n | \bar{N}_{\theta_E}) = \frac{(\bar{N}_{\theta_E})^n e^{-\bar{N}_{\theta_E}}}{n!}.$$ (3.11)

Figure 3.2 shows the distribution of N_{θ_E} for various models of the NS spatial distribution and Galactic potential. We see that the probability of at least one NS being inside the
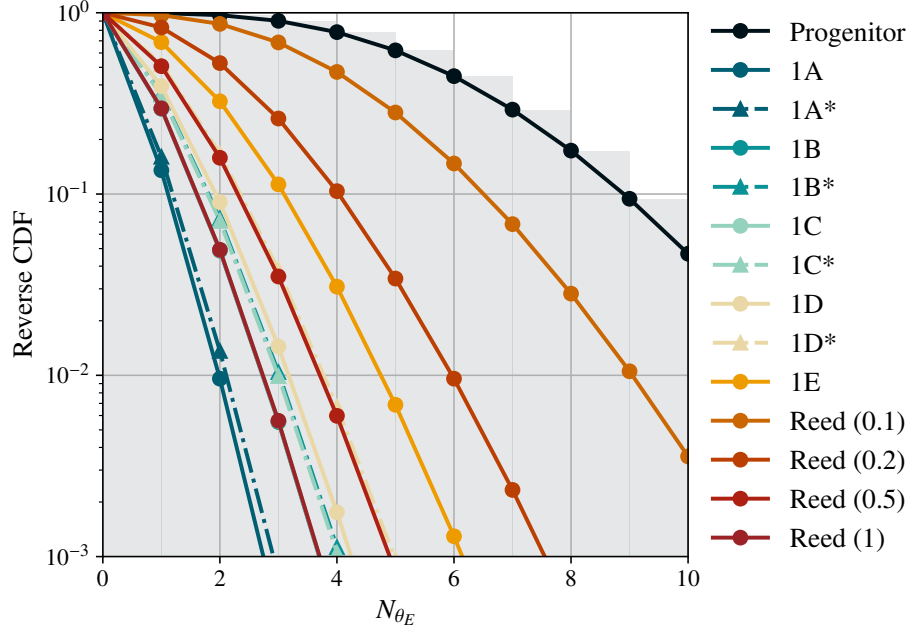
Figure 3.2: (Reverse) Cumulative distribution of the expected number of NSs within the Einstein angle of the Galactic SMBH as predicted by different models of the NS spatial distribution and Galactic potential. "Progenitor" model assumes that the spatial distribution of NSs follows that of the stars in the galaxy [5]. Models 1A, 1B, 1C, 1D and 1E are predicted by [6] assuming different models of NS birth velocities. The dashed curves correspond to the models 1A*, 1B*, 1C* and 1D* of [6] which assumes the same NS birth velocities but a different model for the Galactic potential. For the [7] models, we consider different values of z_0 (shown in brackets, in kpc). The probability of at least one NS being inside the lensing cone, $P(N_{\theta_E} \geq 1)$, is $\sim 0.1 - 1$, depending on the model.

lensing cone is significant $\sim 0.1 - 1$, depending on the model.

3.4 Lensed continuous GWs and their detectability

We model NS as a triaxial ellipsoid (see, e.g: [198]). Its ellipticity is defined in terms of the moments of inertia around the rotation axis (I) and in the plane perpendicular to the principal axis (I_1, I_2):

$$\epsilon = \frac{|I_1 - I_2|}{I}. \tag{3.12}$$

For a triaxial ellipsoid NS with moment of inertia about rotation axis, I, and ellipticity ϵ, the resulting time-varying mass quadrupole moment will produce GWs whose amplitude is proportional to ϵ, I, as well as the squared rotation frequency $f_\star$:

$$h_0 = \frac{16\pi^2 G_N}{c^4} \frac{\epsilon \, I \, f_\star^2}{r}, \tag{3.13}$$

67
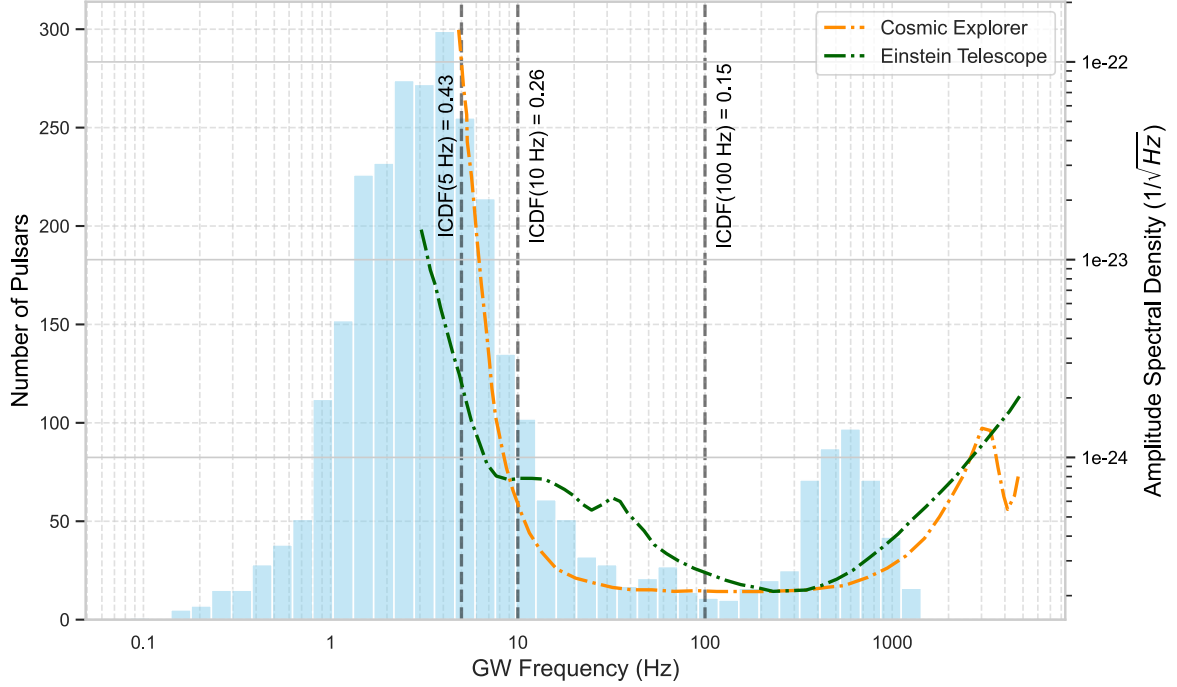
Figure 3.3: Histogram of GW emission frequencies (i.e., twice the rotation frequency) of known pulsars from the ATNF catalogue [8]. Vertical dashed lines indicate the inverse cumulative distribution function evaluated at 5 Hz, 10 Hz, and 100 Hz, illustrating the fraction of pulsars emitting above those frequencies. The ASD curves of the ET and CE, from the "optimal" curves presented in Fig. 2 of [9], are overlaid (refer to the right y-axis) highlighting the frequency ranges where these detectors are sensitive.

where r is the distance to the NS. For the mass quadrupole radiation considered here, we consider the monochromatic signal at twice the rotation frequency of the star ($f_{\mathrm{GW}} = 2f_\star$). As in the discussion of section 1.4.2, other mechanisms such as the r-mode instabilities or free precession in NSs can radiate at different harmonics ($\frac{4}{3}f_\star$ and $f_\star$ respectively). The corresponding GW polarizations are given by:

$$h_+(t) = A_+ \, h_0 \, \cos\left(2\pi f_{\mathrm{GW}} \, t + \varphi\right), \tag{3.14}$$

$$h_\times(t) = A_\times \, h_0 \, \sin\left(2\pi f_{\mathrm{GW}} \, t + \varphi\right), \tag{3.15}$$

where $A_+ = \sin^2\chi \frac{1+\cos^2\iota}{2}$, $A_\times = \sin^2\chi \cos\iota$. Here, ι is the inclination angle between the total angular momentum vector of the star and the line of sight, χ is called the wobble angle, and $\frac{\pi}{2} - \chi$ is the misalignment angle of the total angular momentum to the rotation axis, and φ is a constant phase offset. [4]

---

[4]For $\chi \neq \frac{\pi}{2}$, free precession of the system also leads to emission at $f_{\mathrm{GW}} = f_*$. We only consider the second harmonic, $f_{\mathrm{GW}} = 2f_*$ here.

The measured GW strain at a detector depends on its response to the GWs. This response, characterized by the time-dependent antenna pattern functions $F_+(t), F_\times(t)$, depends on the relative orientation and location of the detector with respect to the source location:

$$h(t) = F_+(t)h_+(t) + F_\times(t)h_\times(t). \tag{3.16}$$

CWs lensed by the Galactic SMBH (modeled as a point-mass lens with mass M_L), will produce exactly two images with magnification $\mu_{\frac{1}{2}}$ and time delay $\Delta t_{\frac{1}{2}}$. As we established in chapter 2, lensing doesn't alter polarisations of GWs. The lensed strain for "plus" and "cross" polarisations of the two images can be written as:

$$h_{j,\overset{+}{\times}}^{L}\left(t; \mu_j, \Delta t_j\right) = \sqrt{|\mu_j|} h_{j,\overset{+}{\times}}\left(t - \Delta t_j\right) \tag{3.17}$$

where the subscript $j \in \{1, 2\}$ denotes the two images, μ_j is their respective magnifications and Δt_j their time delays. Without loss of generality, one can set the $\Delta t_1 = 0$ such that Δt_2 (hereafter just Δt) denotes the arrival time delay of the second image with respect to the first. For a point mass lens, in the strong lensing regime, i.e., $\beta < \theta_E$, the time delay between the two images is approximately given by:

$$\Delta t \simeq 2 \frac{D_{\mathrm{L}} D_{\mathrm{S}}}{c D_{\mathrm{SL}}} \theta_E \beta. \tag{3.18}$$

For a lens mass of $4.15 \times 10^6\, M_\odot$, corresponding to Sgr A*, the time delay between the two images varies approximately between 16 and 160 seconds as β ranges from $0.1\,\theta_E$ to θ_E. The resulting strain measured at the detector will therefore be a superposition of the two copies of CWs:

$$h_{\mathrm{tot}}(t) = \sqrt{\mu^{\mathrm{int}}} \left[F_+(t)h_+(t) + F_\times(t)h_\times(t) \right]. \tag{3.19}$$

Here, μ^{int} is an amplification factor that results from the interference of the two lensed

signals, and is given by [5]

$$\mu^{\text{int}} = |\mu_1| + |\mu_2| + 2\sqrt{|\mu_1 \mu_2|}\cos(2\pi f_{\text{GW}}\,\Delta t). \tag{3.20}$$

In order to assess the detectability of such signals, we evaluate an averaged SNR ρ of the composite image given in Eq. 3.19 (which depends on an averaged h_{tot}^2), where the average is taken over the period of rotation of the NS (for $h_{+,\times}$), the sidereal day (for $F_{+,\times}$), as well as the inclination angle (ι), polarization angle (ψ), and wobble angle (χ).

$$\rho = \left[\frac{\langle (h^{\text{tot}})^2 \rangle (f_{\text{GW}}) T_{\text{obs}}}{S_n(f_{\text{GW}})} \right]^{1/2}. \tag{3.21}$$

Here, $S_n(f_{\text{GW}})$ is the detector's noise PSD at the GW frequency, and T_{obs} is the observation time. Since the signal is periodic during the observation time, the SNR can be evaluated using a time average. While doing so, it is important to note that the two polarizations of the signal are periodic over the much shorter half-rotation period of NS while the antenna pattern function is periodic over a sidereal day. The time average $\langle (h^{\text{tot}})^2 \rangle$ can therefore be separated into an average over the NS period for $\langle (h_+)^2 \rangle$ and $\langle (h_\times)^2 \rangle$, and a sidereal day average for $\langle F_+^2 \rangle$ and $\langle F_\times^2 \rangle$.

We simulated populations of NSs within the lensing cone, distributed according to different models. For each NS, we computed the lensing magnifications and time delays using Eqs. (3.2) and (3.18). The single-detector SNR (defined in Eq. (3.21)) was evaluated for the superposed images after accounting for interference (cf. Eqs. 3.19, 3.20). We set the sky location of the lensed sources to coincide with the location of the SMBH (Sgr A*), which is a good approximation given that the Einstein angle extends to within an arcsecond centered at that location. We assume an ellipticity of $\epsilon = 10^{-7}$, and frequencies drawn from the frequency distribution of pulsars in the ATNF catalog [8].

The network SNR is the quadratic sum of the individual detector SNRs.

---

[5]Note that in addition to this amplification, lensing will add a constant phase φ^{int} to the signal that depends on the magnifications of the images, and the time delay. This can be absorbed into the phase constant φ. However, proper motion of the source with respect to the optical axis will make μ^{int} and φ^{int} time-dependent, introducing amplitude and phase modulations in the lensed signal. We discuss these implications in later chapters.
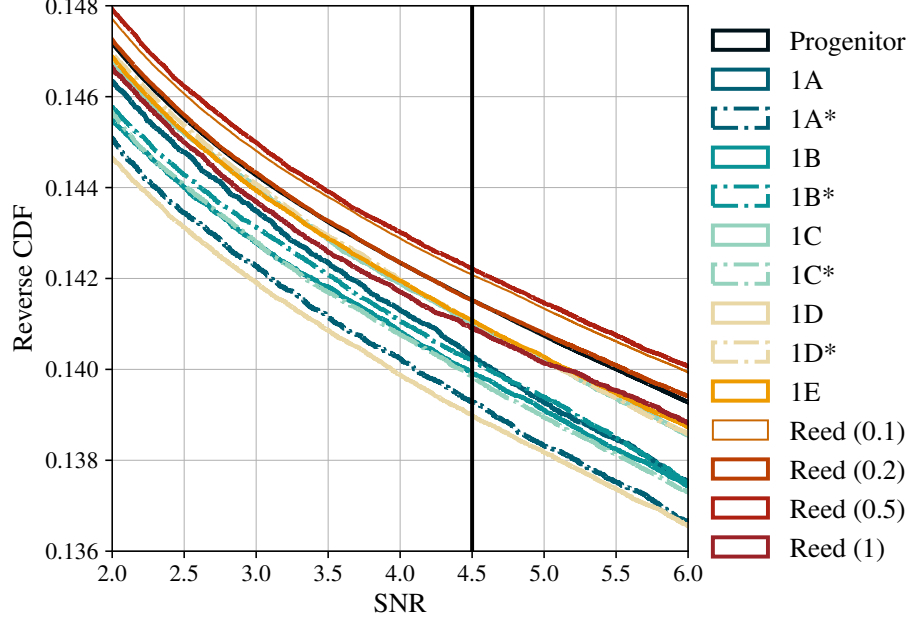
Figure 3.4: (Reverse) Cumulative distribution of the SNRs of the lensed NSs for different spatial distributions (same as Fig.3.2). The SNR threshold of 4.5 corresponding to a false alarm probability of 1% and false dismissal probability of 10% using a single-template search is shown by the vertical line. The fraction of lensed NSs crossing the threshold is approximately reflects fraction of the pulsar population above rotation frequency of 50 Hz ($f_{GW} = 100$ Hz) as seen in Fig. 3.3

The fraction of detectable NSs within the Einstein angle is

$$N_{\theta_E}^{\mathrm{det}} = N_{\theta_E} \ \alpha(\rho_{\mathrm{thresh}}), \quad \alpha(\rho_{\mathrm{thresh}}) = \int_{\rho_{\mathrm{thresh}}}^{\infty} \frac{dP}{d\rho} d\rho, \tag{3.22}$$

where the SNR distribution $dP/d\rho$ for each model is estimated from simulations (see Fig. 3.4). We reference our SNR threshold choice based on the formulation developed by Jaranowski, Krolak & Schutz [43], which defines a detection statistic, known as $\mathcal{F}$-statistic, by analytically maximizing log-likelihood over the amplitude parameters. It has been shown that $X = 2\mathcal{F}$ follows a chi-squared (χ^2) distribution with 4 degrees of freedom and a non-centrality parameter equal to square of the SNR, ρ^2, i.e.

$$P(X) = \chi^2(X|4, \rho^2) \tag{3.23}$$

The false alarm probability (FAP) and the false dismissal probability (FDP) can be used

71

to set the threshold on ρ by using:

$$\text{FAP} = \int_{X_{\text{thresh}}}^{\infty} \chi^2(X|4, \rho^2 = 0)dX \qquad (3.24)$$

$$\text{FDP} = \int_{0}^{X_{\text{thresh}}} \chi^2(X|4, \rho^2)dX \qquad (3.25)$$

Choosing a FAP of 1% with a FDP of 10% sets $X_{\text{thresh}} = 13.27$ and corresponding $\rho_{\text{thresh}} = 4.5$. Figure 3.5 shows the distribution of detectable number of NSs within the Einstein cone based on this choice of threshold. Depending on the model and the assumptions of the NS properties, the probability of detecting at least one strongly lensed NS is $\sim 2 - 53\%$ [6].

We also investigated the detection probability of lensed NSs in the fifth observing run (O5) of LIGO, Virgo and KAGRA [199], and find that the range of detection probabilities is $\sim 0 - 15\%$ [7]. However, a realistic search for such signals would require a bank of templates, since the intrinsic parameters of the NSs are not known a priori. Assuming a directed search towards the Galactic center involving $\sim 10^{12}$ templates [196], the SNR threshold corresponding to the FAP and FDP mentioned above, but now also accounting for the trials factor due to the template bank, becomes $\simeq 9.6$. With this threshold, the detection probability in O5 drops to $\sim 0-2\%$. In 3G detectors, this probability continues to be non-trivial, with a range of $\sim 2 - 51\%$. If we make a more pessimistic assumption of ellipticity $\epsilon = 10^{-8}$, LIGO-Virgo detectors are unlikely to detect any lensed signals. In 3G detectors, the detection probability is $\sim 1 - 36\%$ for a single template search and $\sim 0 - 18\%$ for a directed search involving 10^{12} templates. Smaller values of ϵ will reduce the detection probability further.

These estimates are consistent with the non-detection of CWs by the directed searches towards the Galactic center using LIGO-Virgo data from the third observing run [195]. Using the spatial and frequency distribution models that we employed to study the detectability of lensed signals, we estimate the detection probability of (all) CWs to be $\sim 0 - 2\%$ with $\epsilon = 10^{-7}$ and coherent integration time of 1 yr [8]. For the coherent in-

---

[6]We assume a three-detector network consisting of two CE detectors and one ET. The expected PSDs are generated from the "optimal" curves presented in Fig. 2 of [9].

[7]We assume a five-detector network involving three LIGO detectors (including LIGO-India), Virgo and KAGRA. The expected PSDs are generated using ALIGOAPLUSDESIGNSENSITIVITYT1800042, ADVVIRGO, KAGRALATESENSITIVITYT1600593 functions of the PyCBC PSD package [200].

[8]Here we assume that the search is directed towards NSs located in a cone that has its apex on the Earth and has a base radius equal to the Einstein radius of the SMBH for a source at $D_{LS} = 15$ kpc.
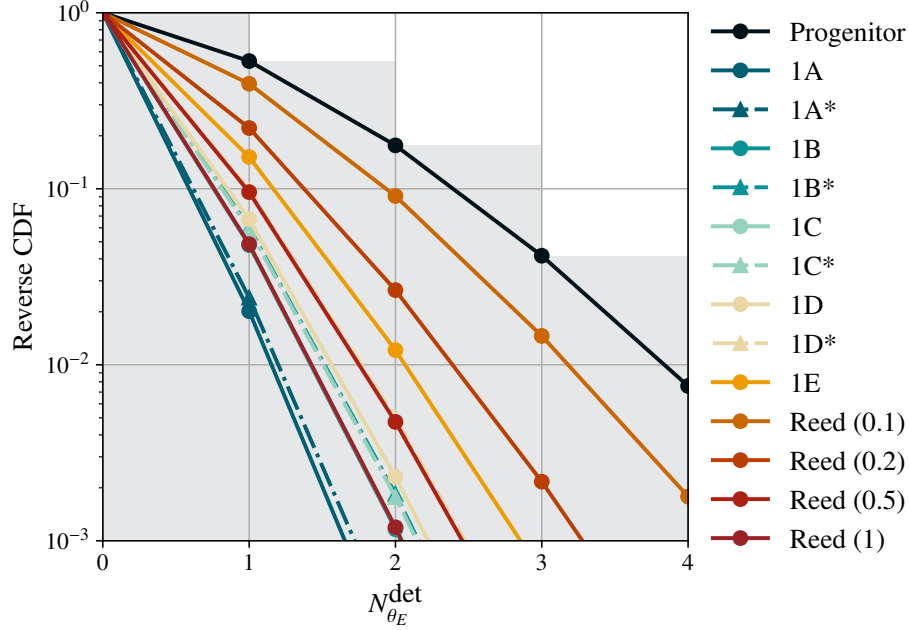
Figure 3.5: (Reverse) Cumulative distribution of the detectable number of strongly lensed events by 3G detectors with SNR threshold of 4.5. The probability of detecting at least one NS inside the lensing cone, $P(N_{\theta_E}^{\text{det}} \geq 1)$, is $\sim 2 - 53\%$, depending on the model. The gray histogram shows the results computed using a simulation using the progenitor model, while the different lines are analytical calculations using Poisson distributions.

tegration times of a few hours employed in [195], the expected detection probability is almost zero.

3.5 Discussion

In this chapter, we explored the possibility of detecting CWs from spinning NSs strongly lensed by the Galactic SMBH. Treating the SMBH as a point-mass lens, we consider a source to be lensed if it lies within the Einstein angle of the SMBH. To assess the prospects of detecting such lensed CWs, we considered several spatial distributions of NSs presented in the literature. We find that up to 6 out of 10^9 NSs lie within the Einstein angle. Accounting for the lensing magnification and time delays as well as the resulting interference between the two images, we evaluate the detectability of such sources.

Unlike the lensing of GW transients such as CBCs, which gives temporally resolved copies of signals whose morphology can be compared to determine whether they are lensed, lensed CWs would show-up in the data as a single, interfering signal. However, they

might be resolved as two different sources in the sky, if the integration time used in the CW search is sufficiently large to attain a sufficiently large sky resolution. This is studied in Chapter 4. Further, if lensing introduces a constant time delay, the interfered signal would be indistinguishable from an unlensed CW with the same amplitude, except for a constant phase shift.

However, if the relative transverse motion between the NS and the lensing optical axis (axis connecting the Earth and the SMBH) is sufficiently large, the time delay Δt between the lensed copies of the CW itself becomes a function of time. This will result in the modulation of the amplitude and phase of the lensed CW signals. Generically, we expect some relative motion between the NS and the optical axis. This could be caused by the proper motion of the NS in the galaxy (e.g., due to the natal kicks; $v \sim 100$ km/s), due to the motion of the Earth around the Sun ($v \sim 30$ km/s), or due to the differential motion of the solar system in the Galactic potential ($v \sim 10$ km/s). A simple, back-of-the-envelope calculation can give an estimate of the degree of this modulation. From Eq.(3.18), the accumulated change in the lensing time delay over an observational time T can be estimated as $\simeq 2 \frac{D_{\mathrm{L}} D_{\mathrm{S}}}{c \, D_{\mathrm{SL}}} \theta_E \frac{d\beta}{dt} \, T \simeq 2 \frac{D_{\mathrm{L}}}{c \, D_{\mathrm{SL}}} \theta_E \, v \, T$. This can cause several modulation cycles in the amplitude and phase of the CW signal over the course of a year.

Lensed CWs, if detected, would enable unique probes of astrophysics and gravity. For example, the lensing time delay, image separation and the amplitude of the images depend on the mass of the lens. Such an observation would therefore be a unique and independent way of measuring the mass of Sgr A*. We explore this in the next chapter.

In addition, compact objects and stars in the Galactic center could produce additional microlensing effects on the GW signal, which are potentially measurable [201–203]. This would be a powerful means of probing the astrophysical environment of the Galactic center. Unlike electromagnetic radiation, GWs do not suffer from extinction, and can potentially provide an uncontaminated picture. For example, radio pulsars are predominantly discovered away from the Galactic plane. Pulsars close to the galactic center are affected by strong radio-wave scattering, dispersion and absorption of the waves by the free electrons, dust and ionized gas in the interstellar medium of the plane [204]. The

nearest observed pulsar to the Galactic Center is PSR J1745-2900, which is still 0.1 pc away from the Sgr A* along the line of sight, and even it is heavily broadened [205]. As such, lensed radio pulsar signals —which require pulsars to be aligned along the line of sight to the Galactic SMBH —would be subject to these additional propagation effects, diminishing their observational viability. Lensed CW signals can, in principle, also contain signatures of additional properties of the SMBH, such as its spin angular momentum [206], and more speculatively, other possible "hairs" [207].

Chapter 4

Inferring the mass of Sgr A* using lensed continuous gravitational waves

4.1 Introduction

The advent of GW astronomy has enriched our understanding of compact objects, such as BHs and NSs. GW signals carry imprints of their source properties, such as their component masses and spins in the case of CBCs. We discussed in Chapter 1, how Bayesian PE techniques infer these properties post the detection of a GW signal. In contrast, estimating the properties of galaxies however still relies on electromagnetic observations. For example, studying the stellar kinematics through velocity dispersion curves provides insights into the mass-profile of galaxies [208, 209]. Similarly, studying Doppler shifts of 21 cm emission lines from neutral hydrogen have been used to study rotation curves and map out mass distributions of galaxies. The galactic rotation curves have also played a crucial role in confirming the presence of dark matter [210–212]. Such galaxy-scale features are not yet accessible through GW events currently detected by the LVK collaboration. The observation of lensed GWs in upcoming years will change this scenario. These GWs will not only have information about the source properties, but also carry information on the mass density profile of the lens galaxies and their substructure through key observables, such as relative magnifications, time delay between multiple images, and wave-optics effects like frequency-dependent waveform modulations.

Similarly, the SMBH at the center of the Milky Way Galaxy has been extensively studied through electromagnetic observations. High resolution tracking of stellar orbits —particularly that of the star S2 —around the Galactic center, such as by the Keck Telescope, Very Large Telescope, and more recently by the GRAVITY collaboration, have played essential role in establishing that Sgr A* is a supermassive compact object and subsequently estimating its mass to be around $4.15 \times 10^6 M_\odot$ [10, 190, 191, 213]. The Event Horizon Telescope image of Sgr A* has further strengthened claims of this compact object being a SMBH [192].

In the previous chapter, we discussed the possibility that CWs from some non-axisymmetric NSs could be lensed by the presence of the Galactic SMBH and detected by the next generation of detectors, such as the ET and CEs. Since lensed signals, as noted earlier, carry additional imprints of the lens property, this chapter is dedicated to how such an observation can be used to probe the mass of Sgr A*, independent of the electromagnetic tracers.

4.2 Method

In this section, we outline the methods used in this chapter. As discussed in section 1.4, CWs are described by their amplitude and phase parameters. We first study how gravitational lensing by a point mass, such as Sgr A*, affects these parameters for the two images. We focus the discussion on three observables: relative amplitude of the two images which is determined by their respective magnifications, the shift in their phase parameters due to the time delay [1], and their sky positions. The imprint of lensing on signal morphology suggests that precise measurement of these parameters can help us reconstruct the lens (Sgr A*) mass. To infer the precision on these parameters, we employ the Bayesian PE technique to recover the posterior distributions of the individual image parameters, and subsequently the lens parameters. While Bayesian PE is a robust inference framework, performing it across the parameter space for different observation times is computationally expensive. To address this, we then conduct a Fisher matrix analysis to get error estimates and posterior distribution for different source and lens parameters. In doing so, we also establish the consistency between the Bayesian PE and

---

[1]We also consider the case of a moving source, resulting in a time-dependent time delay

the Fisher matrix method. We then resample the lens parameters from the amplitude and phase parameter posteriors obtained for the two images.

The rest of the chapter is structured as follows: Section 4.3 details how the lens properties affect the parameters of the two images. We note that the two images have their amplitudes scaled with their respective magnifications, shift their sky position as well as their inferred spin parameters. In Section 4.4, we detail the Bayesian PE technique used to sample the image parameters. We then discuss an approximate and computationally cheaper method of estimating these parameters using the Fisher matrix in Section 4.5. The inference of the lens parameters from the image amplitude and phase is discussed in Section 4.6. Section 4.7 summarizes the chapter.

4.3   Signal Morphology

In Chapter 3, to assess the detectability of the lensed signal, we averaged over the signal phase to calculate the SNR. Inferring the posteriors on these parameters requires a more careful treatment of how they enter the signal model. We therefore revisit our discussion of Section 1.4 and explicitly write the phase of the signal measured at both the Solar system barycenter (SSB) and at the detector's location. For a nearly monochromatic emission from the source, the GW phase can be expressed as a Taylor series:

$$\Phi(t_{\mathrm{NS}}; \{f_{\mathrm{GW}}^{(k)}\}) = 2\pi \sum_{k=0}^{k_{\mathrm{max}}} f_{\mathrm{GW}}^{(k)} \frac{t_{\mathrm{NS}}^{k+1}}{(k+1)!}, \tag{4.1}$$

where $f_{\mathrm{GW}}^{(k)}$ represents the k-th derivative of the GW frequency at reference time $t_{\mathrm{NS}} = 0$. In this chapter we adopt the quadrupole emission model from a triaxial NS, in which case the GW frequency $f_{\mathrm{GW}} = 2f$, where f is the rotational frequency of the star. In terms of the rotational frequency parameters $\{f^{(k)}\}$, the phase of the signal at the NS can be expressed as [2]:

$$\Phi(t_{\mathrm{NS}}; \{f^{(k)}\}) = 4\pi \sum_{k=0}^{k_{\mathrm{max}}} f^{(k)} \frac{t_{\mathrm{NS}}^{k+1}}{(k+1)!}, \tag{4.2}$$

---

[2]From hereon, unless explicitly stated as GW frequency, $\{f^{(k)}\}$ refers to the rotation spin parameters of the star.

For an isolated source, the time taken by a wavefront emitted by a non-relativistic NS at a distance r to reach the SSB is a constant, $\frac{r}{c}$. This allows us to treat the emission time at the NS and the arrival time at the SSB as equivalent. The phase at the SSB can be written as equivalent to the phase at the NS[3]:

$$\Phi(t_{\mathrm{SSB}}; \{f^{(k)}\}) = 4\pi \sum_{k=0}^{k_{\max}} f^{(k)} \frac{t_{\mathrm{SSB}}^{k+1}}{(k+1)!}, \tag{4.3}$$

To write the phase at the detector, one needs to take into account the Doppler shift due to the Earth's rotation about its own axis as well as its revolution around the SSB. Based on Eq. 1.53, the CW phase for a NS with intrinsic spin parameters $\{f^{(k)}\}$ at the detector is approximately written as [43] [4]:

$$\Phi(t; \{f^{(k)}, \hat{n}\}) = 4\pi \sum_{k=0}^{k_{\max}} \frac{f^{(k)}}{(k+1)!} t^{k+1} + \frac{4\pi}{c} \hat{n} \cdot \vec{r}_d(t) \sum_{k=0}^{k_{\max}} \frac{f^{(k)} t^k}{k!}, \tag{4.4}$$

where $\hat{n}$ denotes the sky position of the source measured at the frame attached to the SSB. The total phase at the detector, $\Psi(t; \{f^{(k)}\})$, includes a reference phase, Φ_0 and is given by:

$$\Psi(t; \{f^{(k)}, \hat{n}\}) = \Phi_0 + \Phi(t; \{f^{(k)}, \hat{n}\}). \tag{4.5}$$

The key takeaway is that, since the phase at the SSB is expressible as a Taylor series in terms of the NS spin parameters (Eq. 4.3), we can express the corresponding phase measured at the detector incorporating the Doppler modulation terms as Eq. 4.4. We can now write the GW strain time series measured at the detector as:

$$h(t) = F_+(t; \alpha, \delta, \psi) h_+(t; \{f^{(k)}, \hat{n}\}) +$$
$$F_\times(t; \alpha, \delta, \psi) h_\times(t; \{f^{(k)}, \hat{n}\}), \tag{4.6}$$

$$h_+(t) = h_0 \frac{1 + \cos^2 \iota}{2} \cos \left[\Psi(t; \{f^{(k)}, \hat{n}\}) \right], \text{ and} \tag{4.7}$$

$$h_\times(t) = h_0 \cos \iota \sin \left[\Psi(t; \{f^{(k)}, \hat{n}\}) \right]. \tag{4.8}$$

---

[3]The additional phase shift associated with the travel time can be absorbed in the reference phase, Φ_0.

[4]We ignore the Einstein and Shapiro time delay due to the local gravitational potential of the Solar System

Here, F_+ and $F_\times$ denote the antenna pattern function for the two GW polarizations, ι is the inclination angle of the source, ψ is the polarization angle, and h_0 is the quadrupole amplitude of radiation from a triaxial NS, given by Eq. 3.13.

Having studied the strain for a typical (unlensed) CW signal, we can examine how lensing effects the intrinsic amplitude and phase parameters for the individual images. There are three features associated with a lensed signal in the geometric optics regime:

- Magnification of the individual images,

- Angular separation of the images,

- Time delay between the images.

As discussed earlier, for a source strongly lensed by a point mass, the magnification, angular separation, and the time delay are given by:

$$\mu_{\frac{1}{2}} = \frac{1}{4}\left(\frac{y}{\sqrt{y^2+4}} + \frac{\sqrt{y^2+4}}{y} \pm 2\right), \tag{4.9}$$

$$\Delta\vec{\theta} = \vec{\beta}\left(\sqrt{1 + \frac{4\,\theta_E^2}{\beta^2}}\right), \tag{4.10}$$

$$\Delta t = \frac{2\,D_L\,D_S}{(D_S - D_L)}\,\theta_E\,\beta = \frac{2\,D_L\,D_S}{(D_S - D_L)}\,\theta_E^2\,y. \tag{4.11}$$

Here, $\vec{y} = \frac{\vec{\beta}}{\theta_E}$ is the dimensionless impact parameter, $\vec{\beta}$ is the angular position with respect to the optical axis, and θ_E is the Einstein angle.

The magnification factor μ modifies the observed strain amplitude of each lensed image, scaling the intrinsic amplitude h_0 by $\sqrt{|\mu|}$. Consequently, the strain for the i-th image becomes $h_{0,i} = \sqrt{|\mu_i|}\,h_0$, where μ_i is the magnification of that image. Additionally, lensing shifts the apparent angular position of the source, altering the sky location $\hat{n}$ in the detector-frame phase (Eq. 4.4). To understand the contribution of the time delay, we note that the phase arriving at the SSB has an additional delay of Δt for the second image with respect to the first image. Henceforth, we restrict our treatment to the instantaneous frequency, $f^{(0)} \equiv f$, and the first spin-down term, $f^{(1)} \equiv \dot{f}$. Therefore, while expressing the phase of the two images at the SSB, Φ_1 and Φ_2, the second image should be time

shifted by Δt, i.e.,

$$\Phi_1(t_{SSB}; \{f, \dot{f}\}) = 4\pi \left(f t_{SSB} + \frac{1}{2} \dot{f} t_{SSB}^2 \right), \tag{4.12}$$

$$\Phi_2(t_{SSB}; \{f, \dot{f}\}) = 4\pi \left(f(t_{SSB} - \Delta t) + \frac{1}{2} \dot{f}(t_{SSB} - \Delta t)^2 \right). \tag{4.13}$$

If we consider a source to be moving with a constant transverse velocity $\vec{v} \equiv v\hat{\beta}$, the source position changes over time.

$$\vec{\beta}(t) = \vec{\beta}(t_0) + \frac{\vec{v}}{D_S}(t - t_0). \tag{4.14}$$

Here, without loss of generality, we can set the reference time $t_0 = 0$. Since, the expression for time delay depends on the angular position of the source, $\vec{\beta}$, movement of the source introduces a time-dependent time delay. We can expand Eq. 2.16, for the moving source, and compute the time delay of the second image with respect to the first at the SSB as:

$$\Delta t(t_{SSB}) = \Delta t_0 + \kappa\, t_{SSB}, \tag{4.15}$$

$$\kappa = \frac{D_L\,(\vec{v} \cdot \hat{\beta})(2\,\theta_E)}{c\,D_{SL}} \sqrt{1 + \left(\frac{y}{2}\right)^2}. \tag{4.16}$$

Here, Δt_0 represents the time delay at the reference time, $t_0 = 0$. We now expand the phase of the second image at the SSB in Eq. 4.13 accounting for the temporal dependence of Δt:

$$\Phi_2(t_{SSB}; \{f, \dot{f}\}) = 4\pi \left(f(t_{SSB} - \Delta t_0 - \kappa\, t_{SSB}) + \frac{1}{2}\dot{f}(t_{SSB} - \Delta t_0 - \kappa\, t_{SSB})^2 \right), \tag{4.17}$$

$$= 4\pi \left(\left[f(1-\kappa) - \dot{f}(1-\kappa)\Delta t_0 \right] t_{SSB} + \frac{1}{2} \left[\dot{f}(1-\kappa)^2 \right] t_{SSB}^2 \right)$$

$$- 4\pi f \Delta t_0 + 2\pi \dot{f} \Delta t_0^2. \tag{4.18}$$

Eq. 4.18 reveals that the phase of the second image at the SSB for spin parameters $\{f, \dot{f}\}$ is equivalent to the first image but with apparent spin parameters $\{\tilde{f}, \tilde{\dot{f}}\}$ in the Taylor

expansion of the phase, i.e.

$$\phi_2(t_{SSB}; \{f, \dot{f}\}) \equiv \phi_1(t_{SSB}; \{\tilde{f}, \tilde{\dot{f}}\}) - \tilde{\Phi}_0, \text{ where} \tag{4.19}$$

$$\tilde{f} = f(1 - \kappa) - \dot{f}(1 - \kappa)\Delta t_0 \tag{4.20}$$

$$\tilde{\dot{f}} = \dot{f}(1 - \kappa)^2 \approx \dot{f}(1 - 2\kappa) \tag{4.21}$$

$$\tilde{\Phi}_0 = -4\pi f \Delta t_0 + 2\pi \dot{f} \Delta t_0^2 \tag{4.22}$$

Consider a source with $f = 500$ Hz, $\dot{f} = -10^{-9}$ Hz/s, $y = 0.5$, velocity $=100$ km/s and $D_{LS} = 1$ kpc. In this case, the frequency shift between the two images, $\tilde{f} - f \approx -9 \times 10^{-6}$ Hz. The resolution achieved in frequency as a function of coherent time T goes as [5]:

$$\delta f \sim \frac{1}{T^{3/2}}. \tag{4.23}$$

For full PE done with year long observation time, this resolution is sufficient to distinguish the two images in frequency. This holds true for even the angular separation and frequency derivative, and sets our premise to recover two lensed copies of the CW signal using standard CW templates with different values for the frequency f, the spin down parameter $\dot{f}$, reference phase Φ_0 and the sky location ($\hat{n}$).

It is noteworthy that even for no proper motion, i.e., $\kappa = 0$, there is a frequency shift between the two images due to the intrinsic spin down of the source within the constant time delay interval, Δt_0. We have now established the relation between the amplitude (h_0) and phase parameters ($f, \dot{f}, \hat{n}$) of the images, and the lens parameters, (y, M_L, D_{LS}, v). [6] Although the reference phase is also shifted (see Eq. 4.22), it can only be measured modulo 2π. For the typical time delay of $\mathcal{O}(10\text{–}100)$ s for strong lensing by Sgr A*, the phase shift is much larger than 2π, and measurement of $\tilde{\Phi}_0$ cannot be used to infer the lens parameters. We discuss inference of ($h_0, f, \dot{f}, \hat{n}$) next.

---

[5] $1/T$ comes from the resolution of frequency grid and $1/T^{1/2}$ is the SNR scaling with time. This is only to denote the order of magnitude of the resolution achieved, but PE methods used later in the chapter recover these with more robust techniques.

[6] We consider the distance to the Sgr A*, $D_L = 8$ kpc, known in our analysis.

4.4   Bayesian Parameter Estimation

Eqs. 4.9, 4.10, 4.20, and 4.21 establish relations between the intrinsic parameters of the two images, and therefore carry information about the lens mass, M_L, impact parameter, y, distance, D_{LS}, and transverse velocity, v, of the source. To estimate the precision with which these properties can be measured, we need a handle on how well we can recover the intrinsic phase and amplitude parameters of the images themselves. In this section, we use a time-domain Bayesian PE technique based on [214] to recover these parameters. As discussed in Section 1.3.1, Bayes' theorem can be used to recover the posterior probability distribution of the source parameter:

$$p(\vec{\theta}|s, H) = \frac{\mathcal{L}(s|\vec{\theta}, H)\pi(\vec{\theta}|H)}{\mathcal{Z}(s|H)},\tag{4.24}$$

In the expression above, $\mathcal{L}(s|\vec{\theta}, H)$ is the likelihood function, and gives the probability distribution of the data, s, given the choice of parameters $\vec{\theta}$ under hypothesis H, while $\pi(\vec{\theta}|H)$ is the prior. Under the assumption of Gaussian noise, the likelihood function for source parameters $\vec{\theta}$ given a GW model, h (see Eqs. 4.6, 4.7, and 4.8), takes the form:

$$\mathcal{L}(s|\vec{\theta}, H) \propto \exp\left(-\frac{1}{2}(s - h|s - h)\right),\tag{4.25}$$

where for an observation time, T, and a quasi monochromatic source of frequency, f_{GW}, the brackets $(.|.)$ denote the following time-domain inner product:[7]

$$(x|y) \approx \frac{1}{S_n(f_{GW})} \int_{-T}^{0} x(t)y(t)dt.\tag{4.26}$$

Constructing the Bayesian posteriors for the source parameters requires sampling over the parameter space of $\vec{\theta}$ and computing the corresponding likelihood function $\mathcal{L}(s|\vec{\theta}, H)$. To explore the large parameter space, stochastic sampling methods, such as [79], are used. The sampler makes a choice of parameters $\vec{\theta}_i$ from the prior, computes the likelihood function $\mathcal{L}(s|\vec{\theta}_i, H)$, and jumps to another $\vec{\theta}_{i+1}$. The new sample is selected as the next initial stage with a probability, $\min\left(\frac{\mathcal{L}(s|\vec{\theta}_{i+1},H)}{\mathcal{L}(s|\vec{\theta}_i,H)}, 1\right)$. This is repeated till the sampler con-

---

[7]The convention for the limits of the integral is so chosen because the reference time for Bayesian analysis was set at the end.

Parameters	Range
f	100 Hz to 1000 Hz (in steps of 100 Hz)
$\dot{f}$	-10^{-9} Hz/s
y	0.1, 0.5, 1.0
D_{LS}	0.1, 1, 10 kpc
v	10, 100, 300 km/s

Table 4.1: Parameters used for Bayesian PE runs using CWInPy. The first images were injected with the f and $\dot{f}$ values listed here, while the second images were injected with the corresponding shifted values given by Eqs. 4.20 and 4.21. The sky position of the two images were shifted along the RA, α, by their respective deflection. The amplitude of the two images, h_0 is set as $\sqrt{|\mu_1|}\,h_0$ and $\sqrt{|\mu_2|}\,h_0$, respectively. The lens model assumes a point lens with Sgr A* mass, $4.15 \times 10^6 M_\odot$.

.

verges near the parameter values that maximize the likelihood function. The histogram of the sampled parameters, $\{\vec{\theta}\}$, represents the posterior distribution of the parameters. We employ the Bayesian PE strategy discussed above using the CWInPy python package [214], and construct the posterior distribution on the amplitude parameter h_0 and the phase parameters $\{f, \dot{f}, \alpha\}$. Note that we shift the image location along the right ascension (RA) angle for both the images[8]. CWInPy is a bilby [215] based package, fine tuned to doing CW inference. One major difference is the computation of the likelihood integral in Eq. 4.26. Since for transients, the integral is performed on $\mathcal{O}(1)$ s long data, working with a high sampling rate, typically 4096 Hz, is feasible. However, for longer integration time demanded for CW PE, 4096 Hz of sampling rate makes the data volume prohibitively large to compute the integral across the parameter space. To tackle this issue of large volume of data, CWInPy uses a PE optimization technique called heterodyning, described in [216]. The PE is done using nested sampling [79] on the data for all the relevant parameters, $\{h_0, f, \dot{f}, \alpha\}$, required for lens property reconstruction. We perform this for 3 years of observation period, for ellipticities of $\epsilon = 10^{-6,-7}$ across a range of different intrinsic and lens parameters tabulated in 4.1. We also list the choice of priors in Table 4.2.

For illustration, Figure 4.1 presents the posterior parameter recovered for image 1 given a set of injection parameters, $\{\epsilon = 10^{-7}, f = 500$ Hz, $\dot{f} = -10^{-9}$ Hz/s, $y = 0.5$, $D_{LS} = 1$ kpc, $v = 100$ km/s$\}$. Also, notice that the resolution in the parameters achieved here

---

[8]We restrict sampling of the angular position, $\hat{n}$, to the RA angle α for the Bayesian PE due to the computational limitation of running PE for the various source parameters on the set of two lensed images.
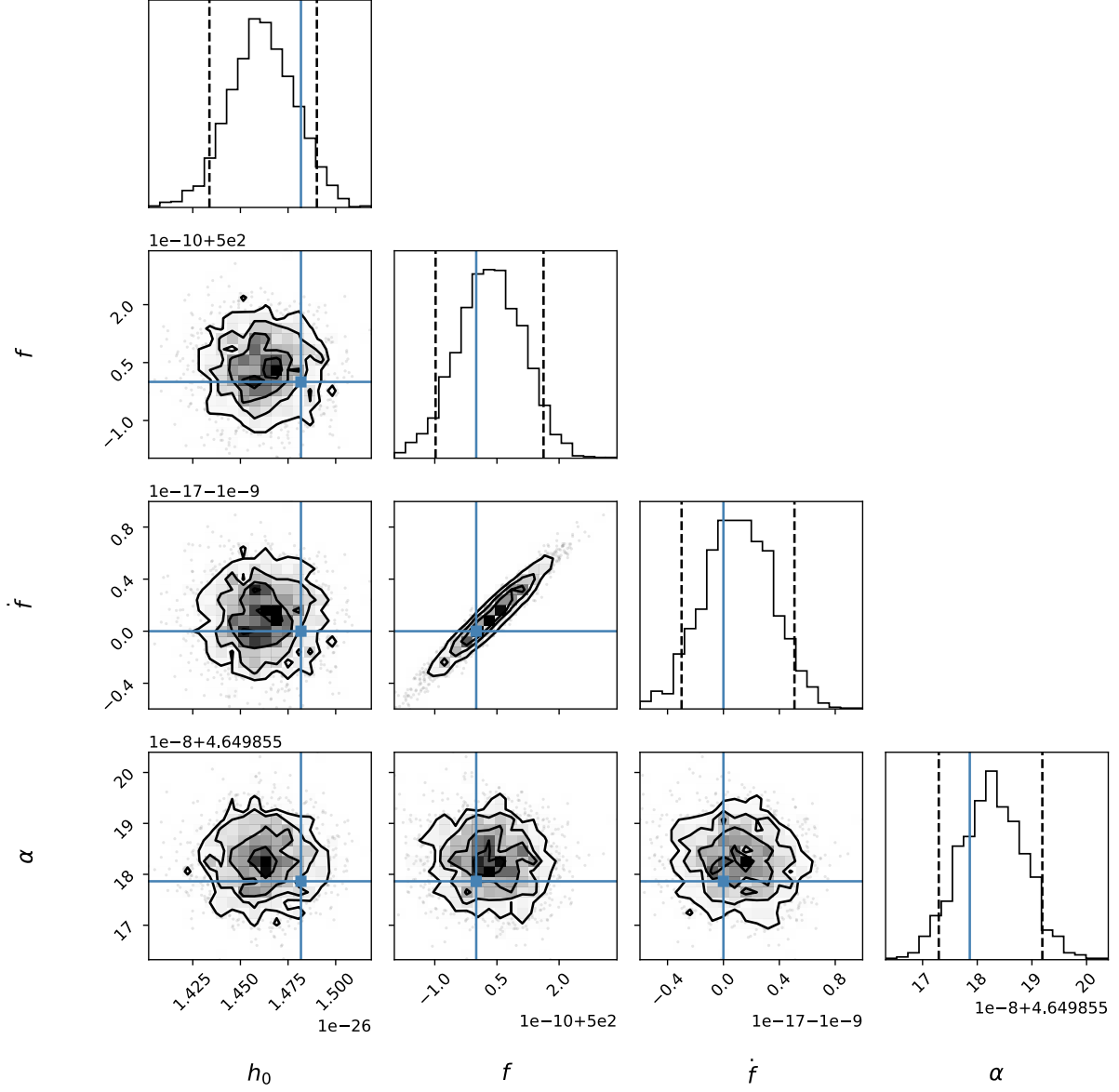
Figure 4.1: Posterior of the amplitude parameter h_0 and phase parameters $\{f, \dot{f}, \alpha\}$ for image 1 of injection done with: ellipticity $\epsilon = 10^{-7}$, source-lens distance $D_{LS} = 1$ kpc, impact parameter at reference time $y = 0.5$, transverse velocity $v = 100$ km/s, intrinsic frequency $f = 500$ Hz, and spin-down $\dot{f} = -10^{-9}$ Hz/s. The remaining amplitude parameters are fixed to the fiducial values of $\cos \iota = 0.5$, $\Phi_0 = 2.4$ rad, and $\psi = 1.1$ rad. h_0 here refers to the scaled amplitude $\sqrt{|\mu_1(y)|} h_0$. The vertical dashed lines in the 1-d marginalized posteriors indicate the 5% and 95% credible limits, while the blue lines in the posterior plots represent the injection value.

Parameter	Prior (Uniform)
h_0	$U(h_0^{\text{inj}}/10,\ 10\,h_0^{\text{inj}})$
f	$U(f^{\text{inj}} - 10^{-7},\ f^{\text{inj}} + 10^{-7})$ Hz
$\dot{f}$	$U(\dot{f}^{\text{inj}}(1 + 10^{-7}),\ \dot{f}^{\text{inj}}(1 - 10^{-7}))$ Hz/s
α	$U(\alpha^{\text{inj}} - 10^{-6},\ \alpha^{\text{inj}} + 10^{-6})$ rad

Table 4.2: Priors used for the Bayesian PE runs. Here, h_0 again represents the intrinsic amplitude scaled with the magnification factor $\sqrt{|\mu_2^1|}$. $U(x, y)$ denotes a uniform probability distribution between x and y. The superscript $(^{\text{inj}})$ denotes the injection value.

are much smaller than the shift values, as claimed earlier.

While CWInPy implements optimization techniques such as heterodyning to make the likelihood computation efficient, running the analysis for different observation times, and various source and lens parameters of the signal is still computationally expensive. To tackle this, we will discuss a method based on Fisher matrix analysis to obtain approximate posteriors in the next section.

4.5 Fisher Matrix Approximation

Given a parametrized model of the waveform, Fisher matrix Γ provides a computationally cheap method of approximating the expected posterior distributions [217]. For a signal model, $h(\vec{\theta})$, the Fisher matrix components Γ_{ij} are given by the expectation value of the derivatives of the log-likelihood with respect to the parameters θ_i, θ_j, i.e.,

$$\Gamma_{ij} = \mathbb{E}\left[-\frac{\partial \log(\mathcal{L}(s|\vec{\theta}, H))}{\partial \theta_i\, \partial \theta_j} \right]. \tag{4.27}$$

For high SNR, where the log likelihood can be expanded around a maximum likelihood point, $\vec{\theta}^{\text{ML}}$, often equal to true parameters of the signal $\vec{\theta}^{tr}$, the Fisher matrix can be written as the following inner product:

$$\Gamma_{ij} = \left(\frac{\partial h}{\partial \theta^i} \middle| \frac{\partial h}{\partial \theta^j} \right), \tag{4.28}$$

such that the likelihood function is Gaussian with the covariance matrix given by the inverse of the Fisher matrix:

$$\mathcal{L}(s|\vec{\theta}, H) \approx \mathrm{N} \exp\left(-\frac{1}{2}\Gamma_{ij}(\theta_i - \theta_i^{tr})(\theta_j - \theta_j^{tr})\right), \tag{4.29}$$

where N is the normalization. The inner product for the CW signal model is given by the Eq. 4.26.

To compute the Fisher matrix components for CW model, it is useful to express the signal model in the well-known JKS factorization introduced in [43]. The signal model described in Eqs. 4.6, 4.8 and 4.7 reads out:

$$h(t; \vec{A}, \vec{\lambda}) = F_+(t; \alpha, \delta, \psi)h_0 \frac{1 + \cos^2 \iota}{2} \cos\left[\Phi_0 + \Phi(t; \vec{\lambda})\right] + $$
$$F_\times(t; \alpha, \delta, \psi)h_0 \cos \iota \sin\left[\Phi_0 + \Phi(t; \vec{\lambda})\right]. \tag{4.30}$$

Here, $\vec{A}$ denotes the amplitude parameters $\equiv \{h_0, \psi, \cos \iota, \Phi_0\}$ and $\vec{\lambda}$ denotes the phase parameters $\equiv \{f, \dot{f}, \alpha, \delta\}$. Explicitly using the expression for the antenna pattern function (see Eq. 1.30), we can rewrite the signal model in the following form [43]:

$$h(t; \vec{\mathcal{A}}, \vec{\lambda}) = \sum_{\mu=1}^{4} \mathcal{A}^\mu h_\mu(t; \vec{\lambda}), \tag{4.31}$$

where the basis waveforms, $h_\mu(t; \vec{\lambda})$ have the form:

$$h_1(t; \vec{\lambda}) = a(t) \cos \Phi(t; \vec{\lambda}), \tag{4.32}$$
$$h_2(t; \vec{\lambda}) = b(t) \cos \Phi(t; \vec{\lambda}), \tag{4.33}$$
$$h_3(t; \vec{\lambda}) = a(t) \sin \Phi(t; \vec{\lambda}), \tag{4.34}$$
$$h_4(t; \vec{\lambda}) = b(t) \sin \Phi(t; \vec{\lambda}), \tag{4.35}$$

and the time-independent expansion coefficients $\mathcal{A}^\mu$ are:

$$\mathcal{A}^1 = h_0 \frac{1 + \cos^2 \iota}{2} \cos \Phi_0 \cos 2\psi - h_0 \cos \iota \sin \Phi_0 \sin 2\psi, \tag{4.36}$$

$$\mathcal{A}^2 = h_0 \frac{1 + \cos^2 \iota}{2} \cos \Phi_0 \sin 2\psi + h_0 \cos \iota \cos \Phi_0 \cos 2\psi, \tag{4.37}$$

$$\mathcal{A}^3 = -h_0 \frac{1 + \cos^2 \iota}{2} \sin \Phi_0 \cos 2\psi - h_0 \cos \iota \cos \Phi_0 \sin 2\psi, \tag{4.38}$$

$$\mathcal{A}^4 = -h_0 \frac{1 + \cos^2 \iota}{2} \sin \Phi_0 \sin 2\psi + h_0 \cos \iota \cos \Phi_0 \cos 2\psi. \tag{4.39}$$

In this new basis, we can now compute the Fisher matrix components for the amplitude parameters $\vec{\mathcal{A}}$ and phase parameters $\vec{\lambda}$. Previous works have demonstrated that these amplitude and phase parameters are practically uncorrelated [218]. We therefore treat them separately. We use the indices $\mu\nu$ when writing the amplitude components of the Fisher matrix and indices i, j to express the phase components.

For the signal model, Eq. 4.31, the amplitude component of the Fisher matrix, $\Gamma_{\mu\nu} = (h_\mu | h_\nu)$, where h_μ and h_ν are the basis vectors in Eq. 4.32.

$$(h_\mu | h_\nu) = T S_n^{-1}(f_{\text{GW}}) \cdot \left[\frac{1}{T} \int_{-T}^{0} h_\mu(t, \vec{\lambda}) h_\nu(t, \vec{\lambda}) dt \right]. \tag{4.40}$$

The term in the square bracket denotes the time average over the observation period $\langle h_\mu h_\nu \rangle \equiv \left[\frac{1}{T} \int_{-T}^{0} h_\mu(t, \vec{\lambda}) h_\nu(t, \vec{\lambda}) dt \right]$. Let's now derive the expression for $\mu = 1, \nu = 1$ component [218].

$$\Gamma_{\mu=1,\nu=1} = T S_n^{-1}(f_{\text{GW}}) \langle a(t) \cos \Phi(t, \vec{\lambda}) \cdot a(t) \cos \Phi(t, \vec{\lambda}) \rangle,$$
$$\approx T S_n^{-1}(f_{\text{GW}}) \langle a^2(t) \rangle \langle \cos^2 \Phi(t, \vec{\lambda}) \rangle. \tag{4.41}$$

In the second step, we have used the approximation that for $f_{\text{GW}} \gg 1/\text{day}$, the antenna pattern function remains almost constant over the GW period. Using $\langle \cos^2 \Phi(t, \vec{\lambda}) \rangle = \frac{1}{2}$, the Fisher matrix component can be written as

$$\Gamma_{\mu=1,\nu=1} = \frac{1}{2} T S_n^{-1}(f_{\text{GW}}) \langle a^2(t) \rangle. \tag{4.42}$$

It is straightforward to similarly compute all the other components, giving us:
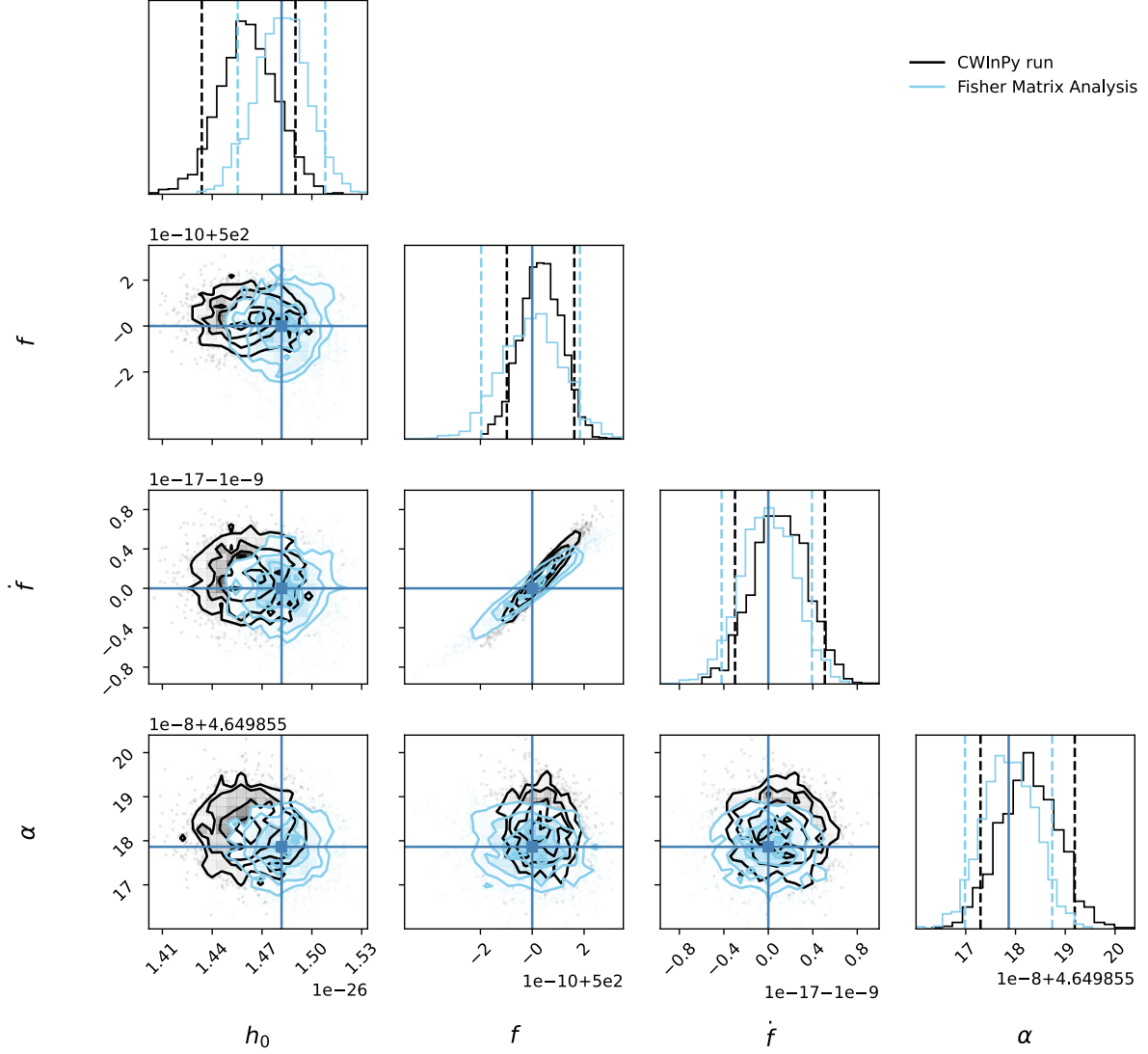
Figure 4.2: Posterior of the amplitude parameter h_0 and phase parameters $\{f, \dot{f}, \alpha\}$ recovered with the Fisher matrix analysis for image 1 of injection done with: ellipticity $\epsilon = 10^{-7}$, source-lens distance $D_{LS} = 1$ kpc, impact parameter at reference time $y = 0.5$, transverse velocity $v = 100$ km/s, intrinsic frequency $f = 500$ Hz, and spin-down $\dot{f} = -10^{-9}$ Hz/s. The remaining amplitude parameters are fixed to the fiducial values of $\cos\iota = 0.5$, $\Phi_0 = 2.4$ rad, and $\psi = 1.1$ rad. h_0 here refers to the scaled amplitude $\sqrt{|\mu_1(y)|} h_0$. The vertical dashed lines in the 1-d marginalized posteriors indicate the 5% and 95% credible limits, while the blue lines in the posterior plots represent the injection value. For comparison the recovered posteriors (as in Figure 4.1) from the CWInPy PE run are also shown in black. The bias in h_0 is due to statistical fluctuation due to noise, and not a systematic bias across CWInPy runs.

$$\Gamma_{\mu\nu} = \frac{1}{2}TS_n^{-1}(f_{\mathrm{GW}}) \begin{pmatrix} \langle a^2(t) \rangle & \langle a(t)b(t) \rangle & 0 & 0 \\ \langle a(t)b(t) \rangle & \langle b^2(t) \rangle & 0 & 0 \\ 0 & 0 & \langle a^2(t) \rangle & \langle a(t)b(t) \rangle \\ 0 & 0 & \langle a(t)b(t) \rangle & \langle b^2(t) \rangle \end{pmatrix} \tag{4.43}$$

We now move our attention to the phase parameters. The expected errors in measuring the phase parameters can be calculated using the so-called phase metric [218, 219].

$$g_{ij} = \left\langle \frac{\partial \Phi(t; \vec{\lambda})}{\partial \lambda^i} \frac{\partial \Phi(t; \vec{\lambda})}{\partial \lambda^j} \right\rangle - \left\langle \frac{\partial \Phi(t; \vec{\lambda})}{\partial \lambda^i} \right\rangle \left\langle \frac{\partial \Phi(t; \vec{\lambda})}{\partial \lambda^j} \right\rangle. \tag{4.44}$$

The phase parameters considered are again the spin (f), spin-down $(\dot{f})$, and angular positions (α, δ). The Fisher matrix on the phase parameter can be then computed as:

$$\Gamma_{ij} = \rho^2 g_{ij}, \tag{4.45}$$

where, ρ is the SNR for the perfectly matched template.

Considering $\vec{\lambda} \equiv \{f, \dot{f}, \alpha, \delta\}$, we can now construct the Fisher matrix for the $8-$dimensional parameter space $\{\vec{\mathcal{A}}, \vec{\lambda}\}$, and therefore the covariance matrix Γ^{-1}. The diagonal elements of this covariance matrix represents the $1-\sigma$ error on the corresponding parameter, while the off diagonal terms represent the correlation between them. Under the assumption of flat priors, we use the derived covariance expression to draw posteriors on the parameters $h_0, f, \dot{f}, \alpha$ [9]. Using the same injection parameters as in Figure 4.1, which presents results from the CWInPy PE, Figure 4.2 shows the corresponding posteriors obtained from the Fisher matrix analysis. In order to validate the consistency of the Fisher approximation across parameter space, we compare its $1 - \sigma$ error estimates with that obtained from CWInPy PE for all parameters tabulated in Table 4.1 for the observation time of 3 years in Figure 4.3. We fix the velocity value to $v = 100$ km/s for this comparison because velocity doesn't affect errors of intrinsic parameters, but only shifts the injection values. Since, the error estimates agree between the two analysis, we now proceed using the Fisher matrix calculation to estimate errors on the lens parameters for different observation time and injection parameters. For computational efficiency in our comparative analysis, we

---

[9]To compute the posterior distribution of h_0 from the amplitude parameters $\vec{\mathcal{A}}$, we apply a change of variables using the Jacobian of the transformation for Eq. 4.36 that relates $\vec{\mathcal{A}}$ to $\{h_0, \psi, \cos \iota, \Phi_0\}$.

Figure 4.3: Comparison of the $1 - \sigma$ (denoted by Σ) error bound on $h_0, f, \dot{f}, \alpha$ (top to bottom panels of the plot respectively) obtained through Fisher matrix analysis with the corresponding $1 - \sigma$ errors obtained in CWInPy PE run. All values for $y, D_{LS}, f,$ and $\dot{f}$ tabulated in Table 4.1 are chosen for the image 1 injection along with ellipticity, $\epsilon = 10^{-6,-7}$ for 3 years observation period to make this comparison. Velocity, $v = 100$ km/s was used since error estimates on intrinsic amplitude and phase parameters aren't affected by this choice. The solid line represents the Fisher matrix estimate, while the marker of the same color is the CWInPy estimate on $1 - \sigma$ error bounds for the corresponding parameters.

restricted the parameter space for each lensed image to $\{h_0, f, \dot{f}, \alpha\}$. Henceforth, with the Fisher analysis method, we will include the declination (dec) angle δ and sample all the relevant parameters, $\{h_0, f, \dot{f}, \alpha, \delta\}$ for each lensed image. Sampling δ ensures accurate estimation of sky localization error and therefore accurate error estimates on the lens parameters.

4.6   Reconstruction of the lens properties

We noted in Section 4.3, how the amplitude parameter h_0 and the phase parameters $f, \dot{f}, \hat{n}$ of the two lensed image are related. In the subsequent sections, we estimated the precision with which these parameters for the individual copies can be measured given an observed lensed event. Here, we use these to compute the errors on the lens parameters (y, M_L, D_{LS}, v) sampled from the intrinsic parameters of the images. We will consider two cases: 1) Static source ($v = 0$), [10] and 2) Moving source ($v \neq 0$).

For the case of no transverse motion of the source, the parameter κ in Eq. 4.16 becomes 0. Therefore, the frequency shift $\Delta f = \tilde{f} - f$ and spin-down shift $\Delta \dot{f} = \tilde{\dot{f}} - \dot{f}$ derived from Eq. 4.20 and 4.21 between the two images are given by:

$$\Delta f = -\dot{f} \Delta t_0, \tag{4.46}$$

$$\Delta \dot{f} = 0. \tag{4.47}$$

Furthermore, the ratio of the amplitude of the two images can be written as:

$$\frac{h_{0,1}}{h_{0,2}} = \sqrt{\frac{|\mu_1|}{|\mu_2|}} = \sqrt{|\mu_{\rm rel}|}, \text{ where} \tag{4.48}$$

$$\sqrt{\mu_{\rm rel}} = \left[\frac{y^2 + y\sqrt{y^2 + 4} + 2}{y^2 - y\sqrt{y^2 + 4} + 2} \right]^{1/2}. \tag{4.49}$$

The difference in the image positions can also be expressed in terms of the dimensionless impact parameter, $y \equiv \frac{\beta}{\theta_E}$ and the Einstein Angle, θ_E. Following Eq. 4.10, we can write the image separation as:

$$\Delta \theta = \theta_E \sqrt{y^2 + 4}. \tag{4.50}$$

---

[10]Static here refers to no transverse motion of the source with respect to the optical axis.

Figure 4.4: Posterior distribution on the lens mass M_L, impact parameter at reference time y, and source distance D_S (in units of lens distance D_L). The injected signal has a frequency of 500 Hz and a spin-down rate of $\dot{f} = -10^{-9}$ Hz/s. The source has ellipticity $\epsilon = 10^{-7}$ located at $y = 0.5$ and $D_{LS} = 1$ kpc behind the lens. The remaining amplitude parameters are fixed to the fiducial values of $\cos \iota = 0.5$, $\Phi_0 = 2.4$ rad, and $\psi = 1.1$ rad. The vertical dashed lines in the 1D marginalized posteriors indicate the 5% and 95% credible limits, while the blue lines in the posterior plots represent the injection value.
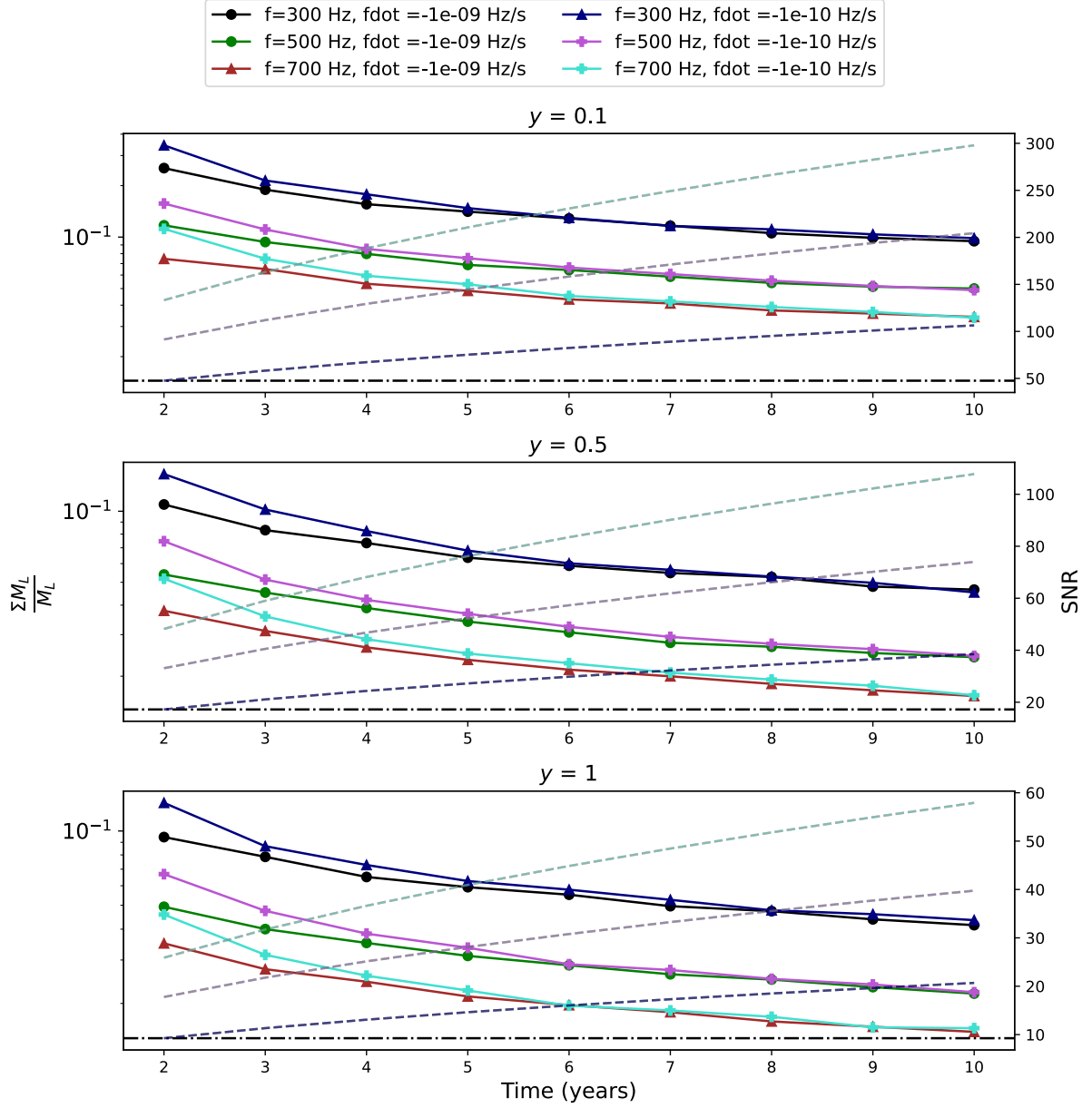
Figure 4.5: Fractional $1 - \sigma$ uncertainty (normalized by the mass M_L) on the lens mass M_L as a function of observation time for a static source. Each panel corresponds to a different value of the impact parameter at reference time $y = \{0.1,\ 0.5,\ 1\}$, and curves within each panel represent different combinations of frequency f and spin-down rate $\dot{f}$. The distance of the source is fixed at $D_{LS} = 1$ kpc behind the lens, and ellipticity $\epsilon = 10^{-7}$. The right vertical axes show the corresponding SNR for the de-magnified image as a function of observation time for each configuration. The dash-dotted horizontal line denotes the mass uncertainty of Sgr A* observed in [10] through 16 years monitoring of stellar orbits around it.

Here we just write the scalar shift because as noted in Section 2.5, the shift of the two images are collinear with a point mass lens. In our analysis, we shift the images along the RA, but the sky position is sampled in both RA and dec.

For this $v = 0$ case, we can now use the Fisher matrix posteriors on intrinsic parameters to derive the posteriors on the lens parameters M_L, y, D_{LS} through the relations noted above. For $f = 500$ Hz, $\dot{f} = 10^{-9}$ Hz/s, $\epsilon = 10^{-7}$, $y = 0.5$ and $D_{LS} = 1$ kpc, Figure 4.4 shows the infer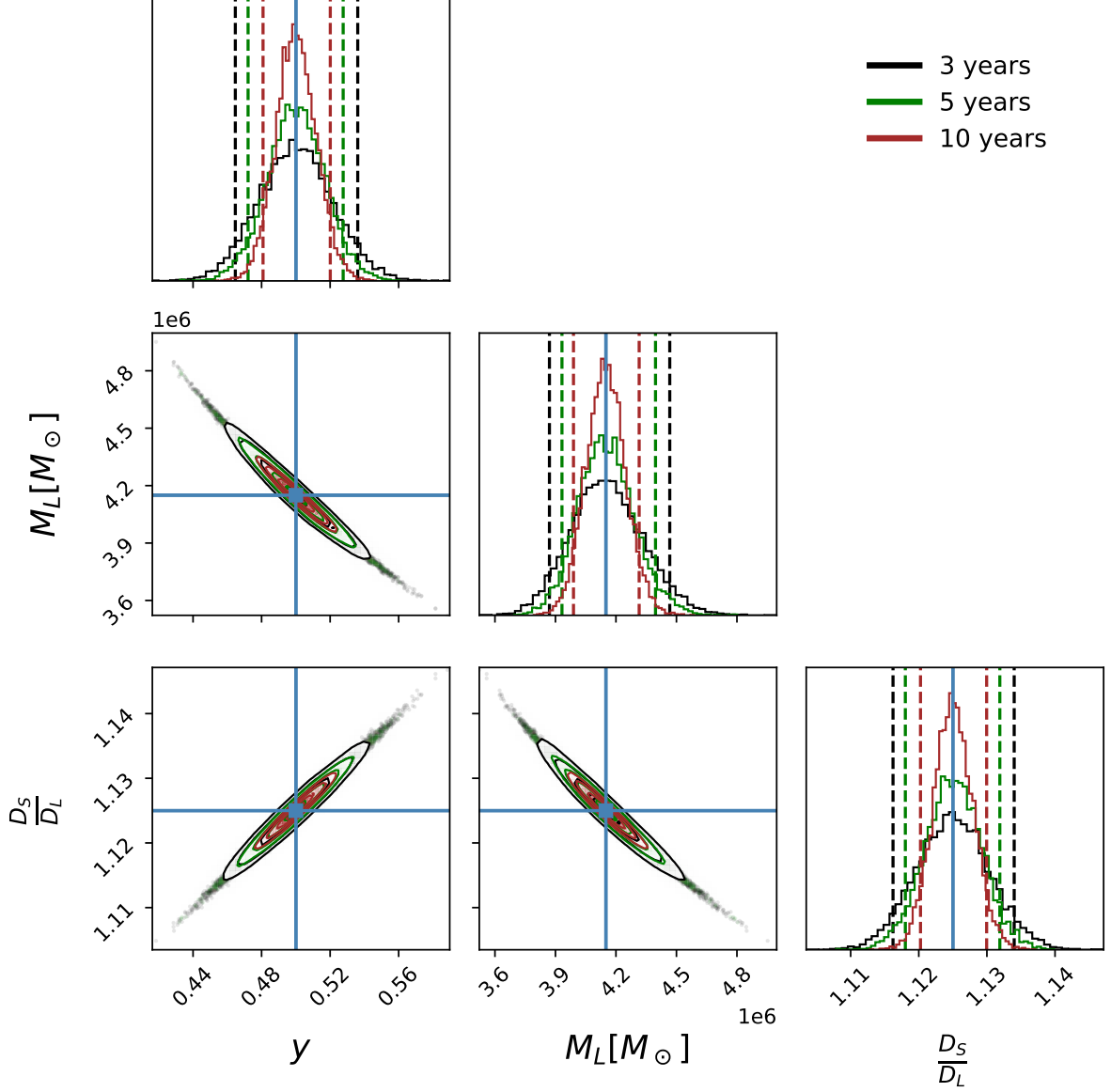red posterior distribution of the lens mass M_L, impact parameter at reference time y and source distance (in units of lens distance $D_L = 8$ kpc) [11] for observation period of 3, 5 and 10 years using ET PSD. To illustrate how the uncertainty in the lens mass measurement scales with observation time, Figure 4.5 shows the $1 - \sigma$ fractional errors on the M_L posteriors for various values of f, $\dot{f}$, and y. We fix the distance of the source from the lens to $D_{LS} = 1$ kpc and the ellipticity to $\epsilon = 10^{-7}$.

The above treatment is based on the hypothesis that the source is static along the transverse direction, and therefore doesn't sample the velocity parameter. However, in more realistic scenarios, we expect the source to move over the long observation period. We therefore now consider the case of $v \neq 0$. The frequency shift and the spin-down shift between the two images can be written as:

$$\Delta f = -\kappa f - \dot{f}(1 - \kappa)\Delta t_0, \tag{4.51}$$

$$\Delta \dot{f} = -2\kappa \dot{f}. \tag{4.52}$$

We sample the entire lens parameter space of (M_L, y, v, D_{LS}) from the intrinsic parameter posterior for individual images using the expressions for the frequency shift (Eq. 4.51), spin-down shift (Eq. 4.52), relative amplitude (Eq. 4.48), and the angular separation (Eq. 4.50). As we now include the parameter κ in the inference and subsequently derive the transverse velocity v, it is important to highlight a key feature. From the spin-down shift relation in Eq. 4.21, the uncertainty in κ is related to the uncertainty in the fractional shift of the spin down,

$$\delta \kappa \approx \delta \left(\frac{\Delta \dot{f}}{\dot{f}} \right) \approx \frac{\delta \Delta \dot{f}}{\Delta \dot{f}} + \frac{\delta \dot{f}}{\dot{f}}. \tag{4.53}$$

---

[11]The source distance is estimated from D_{LS} posterior and known lens distance $D_L = 8$ kpc.
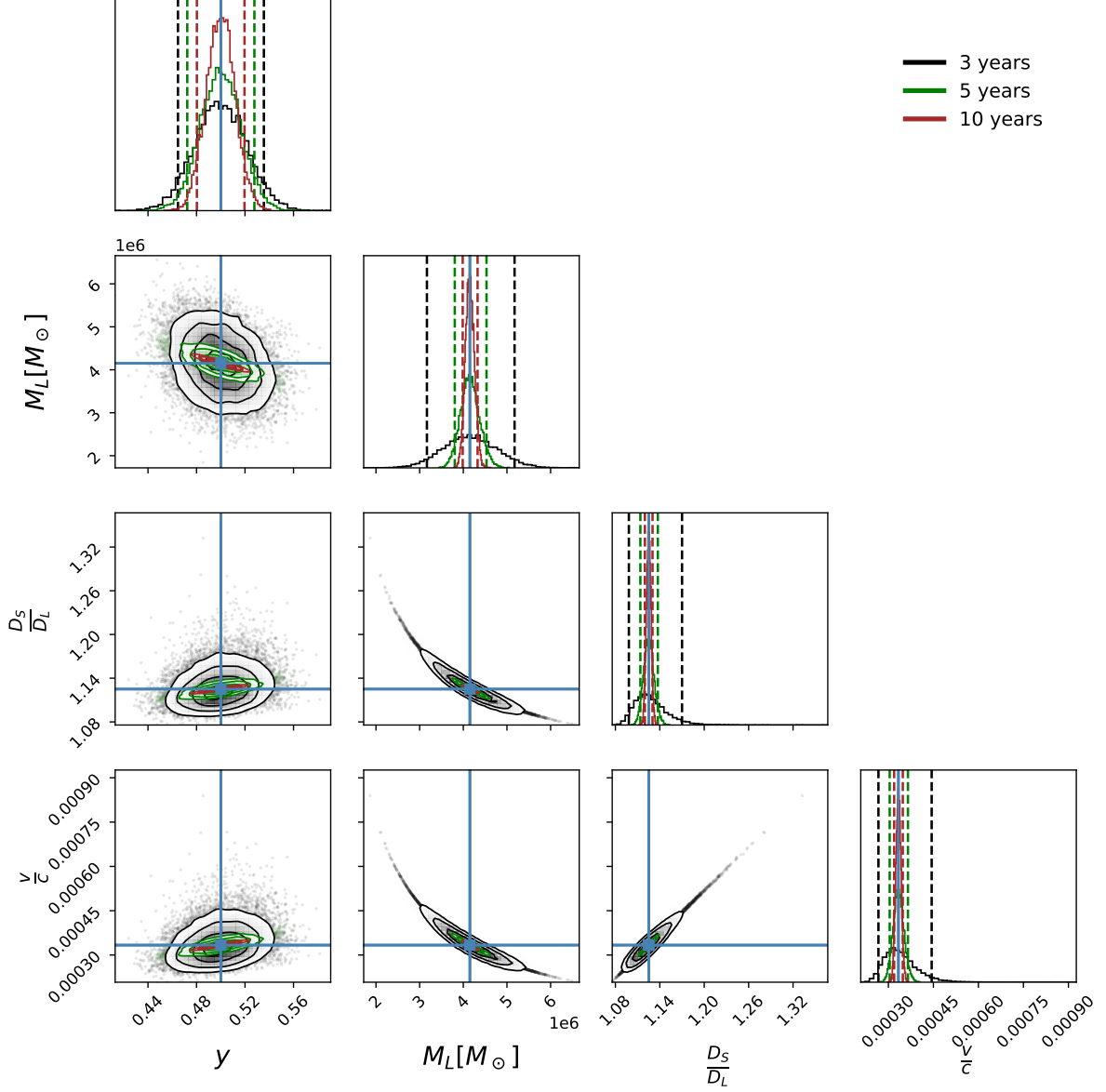
Figure 4.6: Posterior distribution on the lens mass M_L, impact parameter at reference time y, velocity v (in units of c), and source distance D_S (in units of lens distance D_L) for a source moving with constant transverse velocity, $v = 100$ km/s. The injected signal has a frequency of 500 Hz and a spin-down rate of $\dot{f} = -10^{-8}$ Hz/s. The source has ellipticity $\epsilon = 10^{-7}$ located at $y = 0.5$ and $D_{LS} = 1$ kpc. The vertical dashed lines in the 1-d marginalized posteriors indicate the 5% and 95% credible limits, while the blue lines in the posterior plots represent the injection value.

Since $\Delta\dot{f} \ll \dot{f}$ and $\delta\Delta\dot{f} \sim \delta\dot{f}$, the first term typically dominates, and we can approximate:

$$\delta\kappa \approx \frac{\delta\dot{f}}{\Delta\dot{f}}. \tag{4.54}$$

A notable property of the spin-down measurement uncertainty $\delta\dot{f}$ is that it only depends on the SNR and the observation time, and not on the absolute spin-down value itself, while $\Delta\dot{f}$ scales with $\dot{f}$ linearly. As a result, for sources with a large intrinsic spin-down rate $\dot{f}$, the relative shift $\Delta\dot{f}/\dot{f}$ is more easily detectable, leading to significantly smaller errors on κ. Additionally, larger value of $\dot{f}$ enhances contribution of term $\dot{f}(1-\kappa)\Delta t_0$ in Eq. 4.51, leading to better measurements of the lens parameters [12]. Observing a signal from a highly spinning down source thus leads to better constraints on the lens parameters as compared to a slowly spinning down source for all the other parameters fixed. This feature is also seen in other analyses where the NS intrinsic properties like ellipticity ϵ, moment of inertia I, or braking index n from the typical CW amplitude and phase measurements are better inferred for higher values of the spin-down terms (e.g. see [220]).

We now present an illustrative case of the posterior on all the lens parameters for the same choice of fiducial parameters as other corner plots, but a higher $\dot{f}$ value of -10^{-8} Hz/s in Figure 4.6, and the fractional error estimate on the lens mass in Figure 4.7. Any reasonable estimation of the lens mass for lower values of spin-down requires a high SNR signal. To depict this, Figure 4.8 shows the trend of fractional M_L error for an optimistic choice of $\epsilon = 10^{-6}$ including the spin down -10^{-9} Hz/s. It also becomes evident in this figure that higher spin-down results in better lens mass estimation. For the case of highly spinning down source in Figure 4.8, $\dot{f} = -10^{-8}$ Hz/s, lensed CW observation shows comparable accuracy in the measurement of the lens mass to the current EM observation measurement, such as through tracking the stellar orbits around Sgr A*, in [10]. The error estimate on lens pass presented in Figure 4.8 depend loosely on other choices of distance, D_{LS} and transverse velocity, v considered.

---

[12]Reliable estimation from Eq. 4.51 requires $\mathcal{O}(\dot{f}(1-\kappa)\Delta t_0) > \mathcal{O}(\delta(\kappa f))$
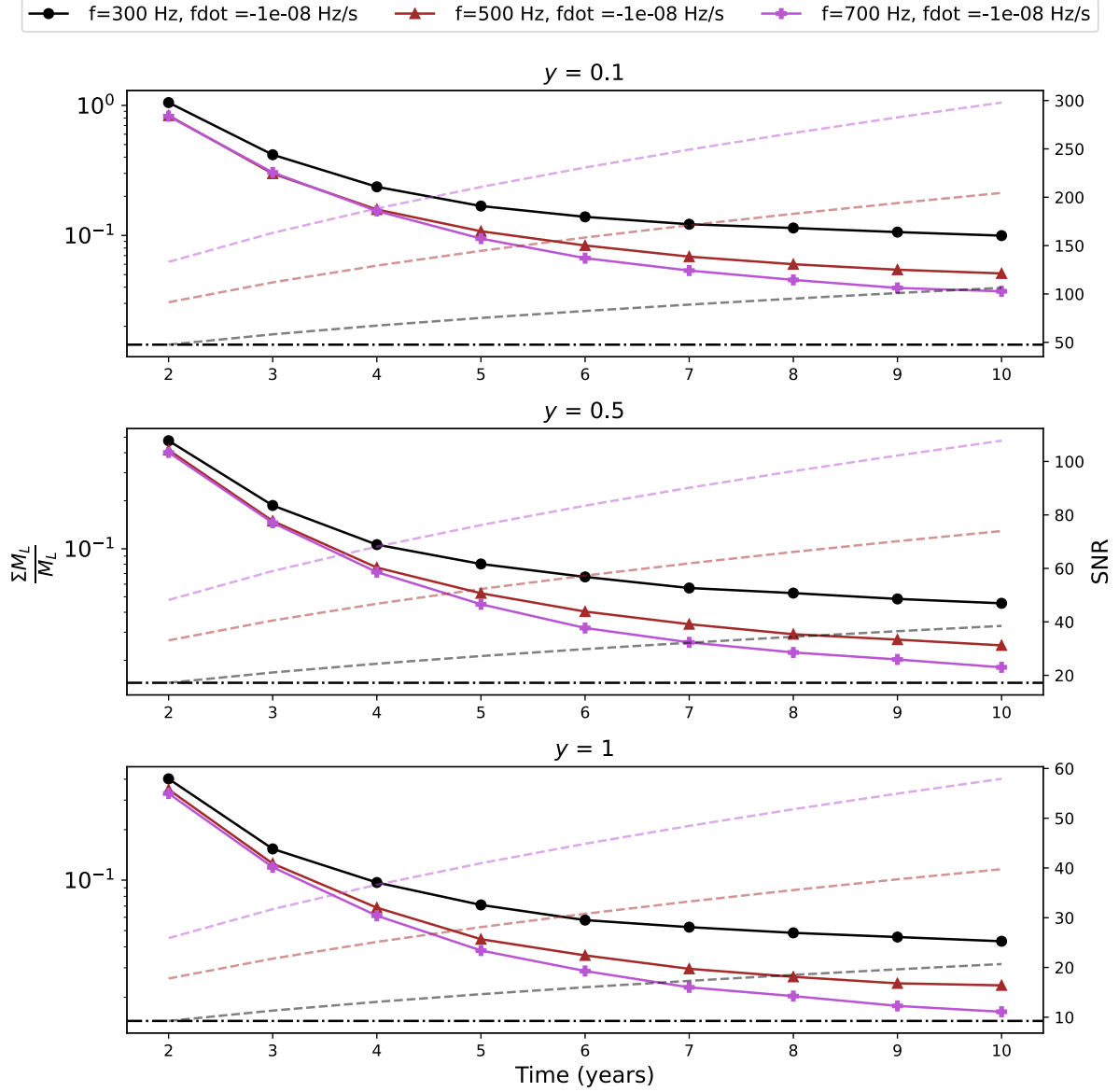
Figure 4.7: Fractional $1 - \sigma$ uncertainty (normalized by the lens mass M_L) as a function of observation time for a source moving with constant transverse velocity, $v = 100$ km/s. Each panel corresponds to an impact parameter at reference time $y = \{0.1,\ 0.5,\ 1\}$, and curves show different frequencies f. The source is located at $D_{LS} = 1$ kpc behind the lens, with ellipticity $\epsilon = 10^{-7}$. Right vertical axes show the corresponding SNR of the de-magnified image for different frequencies. The dash-dotted horizontal line indicates the fractional mass uncertainty of Sgr A* from [10] through 16 years monitoring of stellar orbits around Sgr A* assuming known D_L.

4.7 Discussion

In this chapter, we demonstrate how the observation of CWs from lensed NSs can be used as an independent probe of the mass of the Sgr A*. Using the point mass lens model for Sgr A*, we show that the CW signals from the two lensed images lie in different amplitude and phase parameter space of traditional CWs, but yet remain described by the quasi-monochromatic model. This key insight enables the identification of lensing features through detailed study of the image parameters. We use a Bayesian PE technique using the python package CWInPy and Fisher matrix analysis to perform source property inference for the two images. We then reconstruct the lens parameters for the case of no transverse motion and another more realistic case of a source moving with a constant transverse velocity. For the latter, we find that rapidly spinning NSs lensed by Sgr A* —particularly those with high spin-down rates —can effectively constrain the lens mass. For example, a lensed NS with ellipticity $\epsilon = 10^{-7}$, rotation frequency, $f > 300$ Hz, and spin-down $\dot{f} = -10^{-8}$ Hz/s can be used to estimate the Sgr A* to an accuracy of better than 10% for observation time greater than 5 years with ET (see Figure 4.7). While for sources with smaller spin-down rate, such as $\dot{f} = -10^{-9}$ Hz/s, one needs higher ϵ. For the optimistic choice of $\epsilon = 10^{-6}$, a source with rotation frequency $f > 300$ Hz attains $\approx 10\%$ precision in Sgr A* mass measurement after an observation period of 10 years (see Figure 4.8). Notably for $\epsilon = 10^{-6}$, $f > 300$ Hz, and $\dot{f} = -10^{-8}$ Hz/s, mass measurement for Sgr A* using lensed CW match or exceed the electromagnetic precision from stellar orbit monitoring (e.g. 16-year S2 observation [10]) in observation period of greater than 4 years with ET.

In this analysis, we have assumed the lens profile to be described by a point mass. However, stellar objects in the vicinity of Sgr A* can perturb the potential and cause additional distinct features in the lensed images. For example, a study which also discusses lens property inference using lensed CWs indicates that stellar perturbers around the lens can cause the image positions to no longer be collinear with the lens [221]. The lens potential can also have additional contribution from the dark matter distribution in the Galactic center [222]. Further, microlensing of long duration GWs by stellar objects lead to transient features, such as increased magnifications for the period of a few days [223]. Going beyond the point mass lens model could reveal these substructure features. While

these pose additional challenges, they also present brighter prospects for studying lensing of CWs.
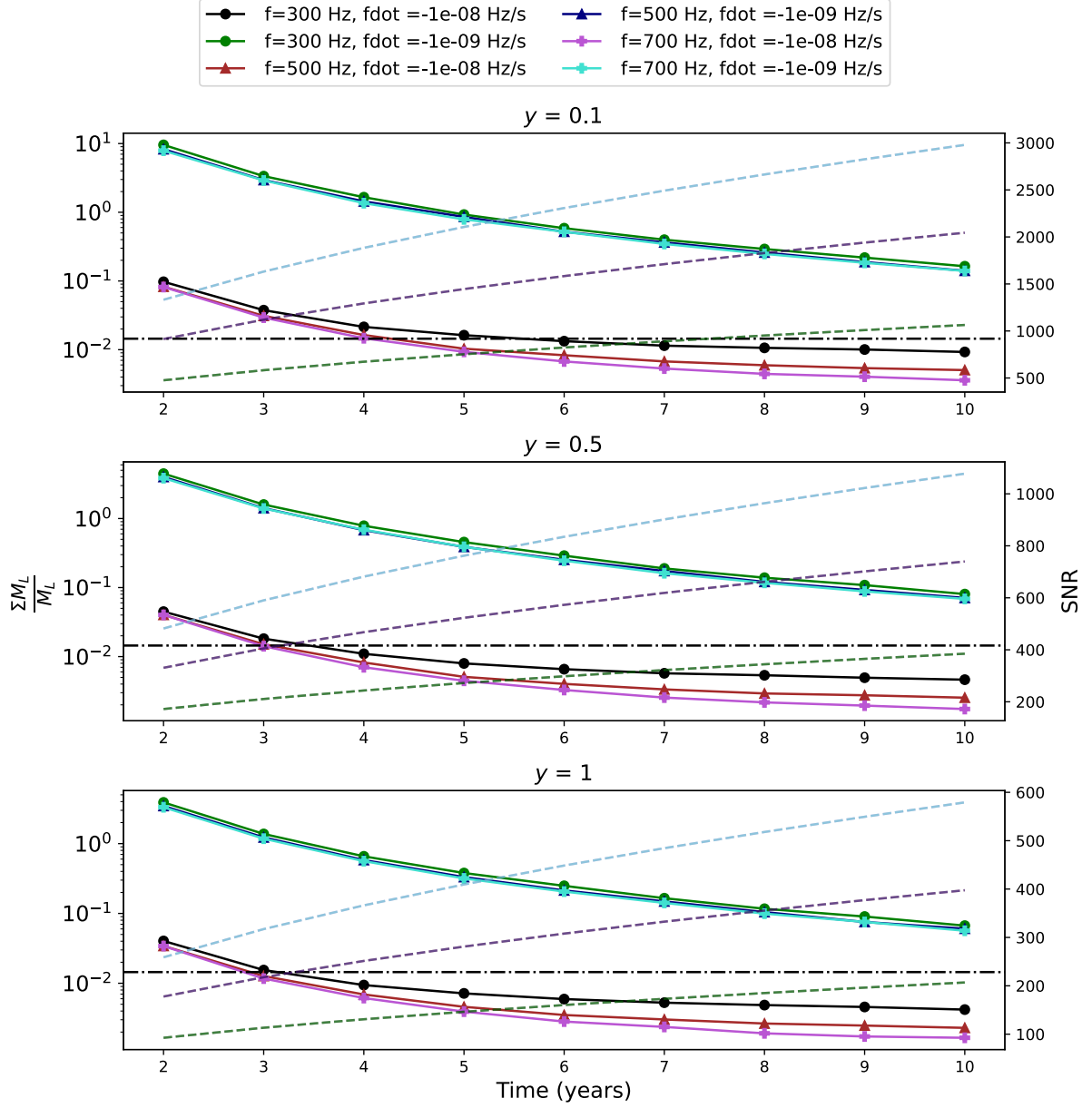
Figure 4.8: Same as Figure 4.7, but for a higher ellipticity $\epsilon = 10^{-6}$ and including spin-down rate $\dot{f} = -10^{-9}$ Hz/s.

Chapter 5

Summary and Discussion

In Chapter 1, we provide an overview of GWs. We learn about their existence by linearizing the Einstein field equations. They originate from sources with time-varying mass quadrupole moments, described to leading order by the Einstein quadrupole formula. We then present several milestones in GW astronomy: from the resonant bar detectors to the indirect evidence via Hulse and Taylor pulsar orbital shrinkage, leading up to the first direct detection of GWs by LIGO. We also discuss how the interferometric detectors operate and the various noise sources that affect them. Finally, we review the different astrophysical sources that produce GWs detectable by current and future detectors, with emphasis on CWs from spinning NSs.

In Chapter 2, we introduce the theory of gravitational lensing within the framework of GR. We study the propagation of GWs in curved spacetime and learn that lensing preserves the nature of GW polarizations. This allows us to study the propagation effect through scalar waves and quantify the effect of lensing on GWs in terms of the scalar amplification factor, given by the Kirchhoff diffraction integral. Within the thin-lens and geometric optics approximation, we study the strong lensing of GWs, particularly for the point mass lens model. Strong lensing by a point mass lens produces two images of the signal with different magnifications and sky positions, and a time delay between them. We then give a brief account of the science case for observing gravitational lensing of GWs.

In Chapter 3, we study the prospects of observing gravitational lensing of CWs. Using various astrophysical models describing the spatial distribution of NSs in our Galaxy, we estimate that up to 6 NSs can be strongly lensed by Sgr A*. This results in two

images of the signal. Unlike CBCs, CWs are not temporally resolved, and the two images therefore interfere in the detectors. Accounting for the magnifications and time delays of the lensed signals, we investigate their detectability by ground-based detectors. Modeling the spin distribution of NSs based on that of known pulsars and assuming an ellipticity of $\epsilon = 10^{-7}$, we report that lensed CWs are unlikely to be detectable by LIGO and Virgo. However, 3G detectors have a $2 - 51\%$ probability of detecting at least one lensed CW signal. For a pessimistic choice of $\epsilon = 10^{-8}$, this probability diminishes to $0 - 18\%$. Though rare, such an observation holds potential for interesting probes of the Galactic SMBH.

We demonstrate this in Chapter 4, where we use Sgr A* as a point mass lens and consider strongly lensed sources both with and without proper motion. We study the signal morphology of the individual images and establish that they can be described by traditional CW models, but with different parameters. Under the assumption that these images can be resolved over long observation periods, we employ Bayesian PE method using CWInPy and Fisher matrix analysis to perform source property inference on individual images. The much lower errors recovered for the parameters compared to the lensing shift validate our premise. We use these estimates to infer the lens parameters, including the lens mass, the source velocity in the transverse direction to the optical axis, the distance of the source from the lens, and the initial impact parameter. Among these, the precise recovery of the lens mass is particularly exciting, indicating the potential of lensed CWs as an independent probe of the Galactic SMBH. For favorable intrinsic parameters of the source, such as high spin, spin-down value, and ellipticity, we forecast that error bounds on the mass of Sgr A* with ET can achieve accuracy comparable to current electromagnetic probes.

Limitations and Future Work

Directed searches towards the Galactic center by the LVK [4] are motivated by the excess Gamma ray emission observed from the inner-parsec region of the Galactic center [224–226]. Possible candidates responsible for such emission include, e.g., proposed dark matter candidates such as weakly interacting massive particles [227], and a population of millisecond pulsars [228]. These candidates provide motivation to extend beyond

the point mass lens model assumed in this work. The dark matter profile extended in the region around the Galactic center makes a compelling case for embedding the point mass lens in a dark matter profile [229, 230], whereas several unresolved NSs or stellar objects motivates consideration of microlensing signatures and perturbations around point mass lens potential in future work.

Moreover, in Chapter 3, we assumed the two images have the same frequency and therefore the interfered image appears as a monochromatic wave, with an overall amplification and constant phase shift. This was done to learn about the astrophysical prospects of detection, without accounting for the waveform systematics. However later in Chapter 4, we studied how the phase parameters of individual images change. In particular, the frequency between the lensed images have a shift, dominantly due to the proper motion of the source (see Eq. 4.20). These shifts are resolvable by long coherence integration which can be performed as follow-ups on detected candidates and remain described by standard CW templates, as shown in Chapter 4. However, directed searches without apriori knowledge of the spin parameters do not integrate the data for the entire observation period due to the prohibitive computational cost associated in doing so, and therefore won't resolve them. For all practical purposes, searches would see an interfered copy of the two quasi-monochromatic signals with slightly different, but unresolved frequencies and sky positions [1]. These interfered signal, therefore, appear as beats with amplitude and phase modulations. Since such modulations are not taken into account for conventional CW searches, this can affect their sensitivity to lensed signals, especially for sources moving with large velocities where such modulations are large. In addition to this, the presence of beating pattern could also affect outlier follow-up strategies that rely on consistent SNR build-up over time. In such cases, lensed signals with noticeable beating may be incorrectly rejected as inconsistent with a standard CW signal hypothesis. This is part of our ongoing investigation.

In Chapter 3, it is also important to note that the frequency distribution of NSs, as drawn from that of known pulsars, has an underlying selection bias towards higher, more detectable frequencies. Using this as a representative distribution for the NS population provides us with an optimistic estimate for the SNR distribution and the detectable

---

[1]In directed search performed in O3, one sky bin is placed and covers 30-300 pc region around the Galactic center depending on the frequency searched. This is much larger than the order arcsecond angular separation of the two images [4].

fraction of lensed NSs. For example, [231] depicts how spin-down over their lifetimes drives most NSs out of the detectable frequency band, even for 3G-era detector networks, providing a more pessimistic outlook for detectability. Moreover, while we considered representative ellipticities on the order of $\sim 10^{-8}$ —10^{-7} for our detection forecasts, studies of the millisecond pulsar population suggest that typical values could be as low as $\sim 10^{-9}$, which would further reduce the strain amplitude and, consequently, the detection prospects [232].

Furthermore, in Chapter 4, while we focused on the phase evolution of the individual images due to proper motion of the source, we treated the magnification factor as a constant. This assumption introduces some caveats to the analysis. The magnifications depend on y. Hence, as y changes due to proper motion of the source, the individual magnifications would also change, especially at lower values of y where the gradient of magnification with respect to impact parameter, y, is considerable. Standard CW inferences do not factor such time variation of intrinsic amplitude into account. While this departure from the standard CW signal model presents additional challenges, factoring in a time varying amplitude could reveal characteristic lensing signatures on individual images. This can therefore serve as tell-tale signatures of lensing and may also additionally improve lens parameter estimation, potentially allowing for partial inference of the lens parameters even when only one image is observable. We plan to include this effect in future work by parameterizing the signal model with the lens parameters themselves while performing the Bayesian PE, and also deriving Fisher matrix estimates beyond the standard treatment of constant amplitude parameters, $\vec{\mathcal{A}}$.

Publications

Publications relevant to this thesis

- Soummyadip Basak, **Aditya Kumar Sharma**, Shasvath J. Kapadia, Parameswaran Ajith.
  Prospects for the Observation of Continuous Gravitational Waves from Spinning Neutron Stars Lensed by the Galactic Supermassive Black Hole.
  The Astrophysical Journal Letters, Volume 942, Number 2, 2023.

- **Aditya Kumar Sharma**, Karl Wette, Parameswaran Ajith.
  Probing the Galactic Supermassive Black Hole using Lensed Continuous Gravitational Waves. *(In Preparation)*

Other Publications:

- Gopalkrishna Prabhu, **Aditya Kumar Sharma**, R Prasad, Shasvath J. Kapadia.
  Constraining the abundance of Galactic compact objects with continuous gravitational waves
  The Astrophysical Journal, Volume 971, Number 2, 2024

- Samson H. W. Leong, Justin Janquart, **Aditya Kumar Sharma**, Paul Martens, Parameswaran Ajith, Otto A. Hannukshela.
  Constraining binary mergers in active galactic nuclei disks using the nonobservation of lensed gravitational waves
  The Astrophysical Journal Letters, Volume 979, Number 2, 2025

Bibliography

[1] F. Gittins, *Gravitational waves from deformed neutron stars: mountains and tides*, Ph.D. thesis, University of Southampton, UK, Sept., 2021.

[2] J.M. Weisberg and J.H. Taylor, *The Relativistic Binary Pulsar B1913+16: Thirty Years of Observations and Analysis*, in *Binary Radio Pulsars*, F.A. Rasio and I.H. Stairs, eds., vol. 328 of *Astronomical Society of the Pacific Conference Series*, p. 25, July, 2005, DOI [astro-ph/0407149].

[3] LIGO Scientific Collaboration, J. Aasi, B.P. Abbott, R. Abbott, T. Abbott, M.R. Abernathy et al., *Advanced LIGO*, *Classical and Quantum Gravity* **32** (2015) 074001 [1411.4547].

[4] R. Abbott, H. Abe, F. Acernese, K. Ackley, N. Adhikari, R.X. Adhikari et al., *Search for continuous gravitational wave emission from the Milky Way center in O3 LIGO-Virgo data*, Phys. Rev. D **106** (2022) 042003 [2204.04523].

[5] B. Paczynski, *A Test of the Galactic Origin of Gamma-Ray Bursts*, ApJ **348** (1990) 485.

[6] N. Sartore, E. Ripamonti, A. Treves and R. Turolla, *Galactic neutron stars. I. Space and velocity distributions in the disk and in the halo*, A&A **510** (2010) A23 [0908.3182].

[7] B.T. Reed, A. Deibel and C.J. Horowitz, *Modeling the Galactic Neutron Star Population for Use in Continuous Gravitational-wave Searches*, ApJ **921** (2021) 89 [2104.00771].

[8] R.N. Manchester, G.B. Hobbs, A. Teoh and M. Hobbs, *The Australia Telescope National Facility Pulsar Catalogue*, AJ **129** (2005) 1993 [astro-ph/0412641].

[9] E.D. Hall and M. Evans, *Metrics for next-generation gravitational-wave detectors*, *Classical and Quantum Gravity* **36** (2019) 225002 [`1902.09485`].

[10] S. Gillessen, F. Eisenhauer, T.K. Fritz, H. Bartko, K. Dodds-Eden, O. Pfuhl et al., *The Orbit of the Star S2 Around SGR A* from Very Large Telescope and Keck Data*, *The Astrophysical Journal Letters* **707** (2009) L114 [`0910.3069`].

[11] A. Einstein, *The Field Equations of Gravitation*, *Sitzungsber. Preuss. Akad. Wiss. Berlin (Math. Phys.)* **1915** (1915) 844.

[12] A. Einstein, *Explanation of the Perihelion Motion of Mercury from the General Theory of Relativity*, *Sitzungsber. Preuss. Akad. Wiss. Berlin (Math. Phys.)* **1915** (1915) 831.

[13] G.M. Clemence, *The relativity effect in planetary motions*, *Rev. Mod. Phys.* **19** (1947) 361.

[14] U.J.L. Verrier, *Théorie du mouvement de mercure*, *Annales de l'Observatoire Impérial de Paris* **5** (1859) 76.

[15] S. Newcomb, *Discussion and results of observations on transits of Mercury from 1677 to 1881*, *United States. Nautical Almanac Office. Astronomical paper ; v.1* **1** (1882) 363.

[16] A.S. Eddington, *The total eclipse of 1919 may 29 and the influence of gravitation on light*, *The Observatory* **42** (1919) 119.

[17] R.V. Pound and G.A. Rebka, *Gravitational red-shift in nuclear resonance*, *Phys. Rev. Lett.* **3** (1959) 439.

[18] R.V. Pound and G.A. Rebka, *Apparent weight of photons*, *Phys. Rev. Lett.* **4** (1960) 337.

[19] A. Einstein, *Über Gravitationswellen*, *Sitzungsber. Preuss. Akad. Wiss. Berlin (Math. Phys.)* **1918** (1918) 154.

[20] M. Maggiore, *Gravitational Waves. Vol. 1: Theory and Experiments*, Oxford Master Series in Physics, Oxford University Press (2007).

[21] J. Weber, *Gravitational radiation, Phys. Rev. Lett.* **18** (1967) 498.

[22] J. Weber, *Evidence for discovery of gravitational radiation, Phys. Rev. Lett.* **22** (1969) 1320.

[23] O.D. Aguiar, *Past, present and future of the resonant-mass gravitational wave detectors, Research in Astronomy and Astrophysics* **11** (2011) 1.

[24] E. Mauceli, Z.K. Geng, W.O. Hamilton, W.W. Johnson, S. Merkowitz, A. Morse et al., *The Allegro gravitational wave detector: Data acquisition and analysis,* Phys. Rev. D **54** (1996) 1264 [`gr-qc/9609058`].

[25] A. Vinante and (for the AURIGA Collaboration), *Present performance and future upgrades of the auriga capacitive readout, Classical and Quantum Gravity* **23** (2006) S103.

[26] P. Astone and (for the ROG Collaboration), *Seven years of data taking and analysis of data from the explorer and nautilus gravitational wave detectors, Classical and Quantum Gravity* **21** (2004) S1585.

[27] P. Ajith, P.A. Seoane, M. Arca Sedda, R. Arcodia, F. Badaracco, B. Banerjee et al., *The Lunar Gravitational-wave Antenna: mission studies and science case,* J. Cosmology Astropart. Phys. **2025** (2025) 108 [`2404.09181`].

[28] R.A. Hulse and J.H. Taylor, *Discovery of a pulsar in a binary system.*, ApJ **195** (1975) L51.

[29] P.C. Peters, *Gravitational Radiation and the Motion of Two Point Masses, Physical Review* **136** (1964) 1224.

[30] B.P. Abbott, R. Abbott, T.D. Abbott, M.R. Abernathy, F. Acernese, K. Ackley et al., *GW150914: First results from the search for binary black hole coalescence with Advanced LIGO,* Phys. Rev. D **93** (2016) 122003 [`1602.03839`].

[31] F. Acernese, M. Agathos, K. Agatsuma, D. Aisa, N. Allemandou, A. Allocca et al., *Advanced Virgo: a second-generation interferometric gravitational wave detector, Classical and Quantum Gravity* **32** (2015) 024001 [`1408.3978`].

[32] KAGRA collaboration, *Overview of KAGRA: Detector design and construction history*, *PTEP* **2021** (2021) 05A101 [2005.05574].

[33] R. Abbott, T.D. Abbott, S. Abraham, F. Acernese, K. Ackley, A. Adams et al., *GWTC-2: Compact Binary Coalescences Observed by LIGO and Virgo during the First Half of the Third Observing Run*, *Physical Review X* **11** (2021) 021053 [2010.14527].

[34] R. Abbott, T. Abbott, F. Acernese, K. Ackley, C. Adams, N. Adhikari et al., *Gwtc-3: Compact binary coalescences observed by ligo and virgo during the second part of the third observing run*, *arXiv preprint arXiv:2111.03606* (2021) .

[35] B.P. Abbott, R. Abbott, T.D. Abbott, F. Acernese, K. Ackley, C. Adams et al., *GW170817: Observation of Gravitational Waves from a Binary Neutron Star Inspiral*, Phys. Rev. Lett. **119** (2017) 161101 [1710.05832].

[36] B.P. Abbott, R. Abbott, T.D. Abbott, S. Abraham, F. Acernese, K. Ackley et al., *GW190425: Observation of a Compact Binary Coalescence with Total Mass $\sim$ 3.4 $M_\odot$*, ApJ **892** (2020) L3 [2001.01761].

[37] R. Abbott, T.D. Abbott, S. Abraham, F. Acernese, K. Ackley, A. Adams et al., *Observation of Gravitational Waves from Two Neutron Star-Black Hole Coalescences*, ApJ **915** (2021) L5 [2106.15163].

[38] R. Abbott et al., *Ligo-virgo-kagra cumulative detection plot - o1-o4b*, jan, 2025.

[39] M. Saleem, J. Rana, V. Gayathri, A. Vijaykumar, S. Goyal, S. Sachdev et al., *The science case for LIGO-India*, *Classical and Quantum Gravity* **39** (2022) 025004 [2105.01716].

[40] C. Cahillane, J. Betzwieser, D.A. Brown, E. Goetz, E.D. Hall, K. Izumi et al., *Calibration uncertainty for Advanced LIGO's first and second observing runs*, Phys. Rev. D **96** (2017) 102001 [1708.03023].

[41] L. Sun, E. Goetz, J.S. Kissel, J. Betzwieser, S. Karki, D. Bhattacharjee et al., *Characterization of systematic error in Advanced LIGO calibration in the second half of O3*, *arXiv e-prints* (2021) arXiv:2107.00129 [2107.00129].

[42] F. Acernese, M. Agathos, A. Ain, S. Albanesi, A. Allocca, A. Amato et al., *Calibration of advanced Virgo and reconstruction of the detector strain h(t) during the observing run O3*, *Classical and Quantum Gravity* **39** (2022) 045006 [`2107.03294`].

[43] P. Jaranowski, A. Królak and B.F. Schutz, *Data analysis of gravitational-wave signals from spinning neutron stars: The signal and its detection*, Phys. Rev. D **58** (1998) 063001 [`gr-qc/9804014`].

[44] L. Trozzo and F. Badaracco, *Seismic and Newtonian Noise in the GW Detectors*, *Galaxies* **10** (2022) 20.

[45] Y. Levin, *Internal thermal noise in the LIGO test masses: A direct approach*, Phys. Rev. D **57** (1998) 659 [`gr-qc/9707013`].

[46] P.R. Saulson, *Thermal noise in mechanical experiments*, Phys. Rev. D **42** (1990) 2437.

[47] C.M. Caves, *Quantum-mechanical noise in an interferometer*, Phys. Rev. D **23** (1981) 1693.

[48] J. Aasi, J. Abadie, B.P. Abbott, R. Abbott, T.D. Abbott, M.R. Abernathy et al., *Enhanced sensitivity of the LIGO gravitational wave detector by using squeezed states of light*, *Nature Photonics* **7** (2013) 613 [`1310.0383`].

[49] D. Ganapathy, W. Jia, M. Nakano, V. Xu, N. Aritomi, T. Cullen et al., *Broadband Quantum Enhancement of the LIGO Detectors with Frequency-Dependent Squeezing*, *Physical Review X* **13** (2023) 041021.

[50] D. Davis, T.B. Littenberg, I.M. Romero-Shaw, M. Millhouse, J. McIver, F. Di Renzo et al., *Subtracting glitches from gravitational-wave detector data during the third LIGO-Virgo observing run*, *Classical and Quantum Gravity* **39** (2022) 245013 [`2207.03429`].

[51] M. Zevin, S. Coughlin, S. Bahaadini, E. Besler, N. Rohani, S. Allen et al., *Gravity Spy: integrating advanced LIGO detector characterization, machine learning, and citizen science*, *Classical and Quantum Gravity* **34** (2017) 064003 [`1611.04596`].

[52] L. Bariuan, R. Gurav, V. Papalexakis and J. Richardson, *Identifying witnesses to ligo glitches using auxiliary channels*, 2022.

[53] S. Hild, M. Abernathy, F. Acernese, P. Amaro-Seoane, N. Andersson, K. Arun et al., *Sensitivity studies for third-generation gravitational wave observatories*, *Classical and Quantum Gravity* **28** (2011) 094013 [1012.0908].

[54] S. Hild, S. Chelkowski and A. Freise, *Pushing towards the ET sensitivity using 'conventional' technology*, *arXiv e-prints* (2008) arXiv:0810.0604 [0810.0604].

[55] M. Punturo, M. Abernathy, F. Acernese, B. Allen, N. Andersson, K. Arun et al., *The third generation of gravitational wave observatories and their science reach*, *Classical and Quantum Gravity* **27** (2010) 084007.

[56] D. Reitze, R.X. Adhikari, S. Ballmer, B. Barish, L. Barsotti, G. Billingsley et al., *Cosmic Explorer: The U.S. Contribution to Gravitational-Wave Astronomy beyond LIGO*, in *Bulletin of the American Astronomical Society*, vol. 51, p. 35, Sept., 2019, DOI [1907.04833].

[57] P. Amaro-Seoane, H. Audley, S. Babak, J. Baker, E. Barausse, P. Bender et al., *Laser Interferometer Space Antenna*, *arXiv e-prints* (2017) arXiv:1702.00786 [1702.00786].

[58] P. Amaro-Seoane, J. Andrews, M. Arca Sedda, A. Askar, Q. Baghi, R. Balasov et al., *Astrophysics with the Laser Interferometer Space Antenna*, *Living Reviews in Relativity* **26** (2023) 2 [2203.06016].

[59] J. Mei, Y.-Z. Bai, J. Bao, E. Barausse, L. Cai, E. Canuto et al., *The TianQin project: Current progress on science and technology*, *Progress of Theoretical and Experimental Physics* **2021** (2021) 05A107 [2008.10332].

[60] M. Musha, *Space gravitational wave detector DECIGO/pre-DECIGO*, in *Society of Photo-Optical Instrumentation Engineers (SPIE) Conference Series*, vol. 10562 of *Society of Photo-Optical Instrumentation Engineers (SPIE) Conference Series*, p. 105623T, Sept., 2017, DOI.

[61] L. Blanchet, *Post-Newtonian theory for gravitational waves*, *Living Reviews in Relativity* **27** (2024) 4.

[62] L. Blanchet, *Gravitational Waves and Dynamics of Compact Binary Systems*, in *General Relativity and Gravitation*, N.T. Bishop and S.D. Maharaj, eds., pp. 54–71, Sept., 2002, DOI [`gr-qc/0201050`].

[63] L. Blanchet, T. Damour, G. Esposito-Farèse and B.R. Iyer, *Gravitational Radiation from Inspiralling Compact Binaries Completed at the Third Post-Newtonian Order*, Phys. Rev. Lett. **93** (2004) 091101 [`gr-qc/0406012`].

[64] L. Blanchet, G. Faye, B.R. Iyer and B. Joguet, *Gravitational-wave inspiral of compact binary systems to 7/2 post-Newtonian order*, Phys. Rev. D **65** (2002) 061501 [`gr-qc/0105099`].

[65] C. Palenzuela, *Introduction to Numerical Relativity*, *Frontiers in Astronomy and Space Sciences* **7** (2020) 58 [`2008.12931`].

[66] M. Boyle, D. Hemberger, D.A.B. Iozzo, G. Lovelace, S. Ossokine, H.P. Pfeiffer et al., *The SXS collaboration catalog of binary black hole simulations*, *Classical and Quantum Gravity* **36** (2019) 195006 [`1904.04831`].

[67] J. Healy and C.O. Lousto, *Fourth RIT binary black hole simulations catalog: Extension to eccentric orbits*, Phys. Rev. D **105** (2022) 124010 [`2202.00018`].

[68] C.V. Vishveshwara, *Scattering of Gravitational Radiation by a Schwarzschild Black-hole*, Nature **227** (1970) 936.

[69] P. Ajith, M. Hannam, S. Husa, Y. Chen, B. Brügmann, N. Dorband et al., *Inspiral-Merger-Ringdown Waveforms for Black-Hole Binaries with Nonprecessing Spins*, Phys. Rev. Lett. **106** (2011) 241101 [`0909.2867`].

[70] A. Buonanno and T. Damour, *Effective one-body approach to general relativistic two-body dynamics*, Phys. Rev. D **59** (1999) 084006 [`gr-qc/9811091`].

[71] L.A. Wainstein and V.D. Zubakov, *Extraction of Signals from Noise* (1970).

[72] B.S. Sathyaprakash and S.V. Dhurandhar, *Choice of filters for the detection of gravitational waves from coalescing binaries*, Phys. Rev. D **44** (1991) 3819.

[73] P. Ajith, S. Babak, Y. Chen, M. Hewitson, B. Krishnan, A.M. Sintes et al., *Template bank for gravitational waveforms from coalescing binary black holes: Nonspinning binaries*, Phys. Rev. D **77** (2008) 104017 [`0710.2335`].

[74] B. Allen, *Optimal template banks*, Phys. Rev. D **104** (2021) 042005 [`2102.11254`].

[75] C. Kalaghatgi, P. Ajith and K.G. Arun, *Template-space metric for searches for gravitational waves from the inspiral, merger, and ringdown of binary black holes*, Phys. Rev. D **91** (2015) 124042 [`1501.04418`].

[76] C. Cutler and É.E. Flanagan, *Gravitational waves from merging compact binaries: How accurately can one extract the binary's parameters from the inspiral waveform\?*, Phys. Rev. D **49** (1994) 2658 [`gr-qc/9402014`].

[77] E. Thrane and C. Talbot, *An introduction to Bayesian inference in gravitational-wave astronomy: Parameter estimation, model selection, and hierarchical models*, PASA **36** (2019) e010 [`1809.02293`].

[78] N. Christensen and R. Meyer, *Parameter estimation with gravitational waves*, *Reviews of Modern Physics* **94** (2022) 025001 [`2204.04449`].

[79] J. Skilling, *Nested Sampling*, in *Bayesian Inference and Maximum Entropy Methods in Science and Engineering: 24th International Workshop on Bayesian Inference and Maximum Entropy Methods in Science and Engineering*, R. Fischer, R. Preuss and U.V. Toussaint, eds., vol. 735 of *American Institute of Physics Conference Series*, pp. 395–405, AIP, Nov., 2004, DOI.

[80] K. Kotake and T. Kuroda, *Gravitational Waves from Core-Collapse Supernovae*, in *Handbook of Supernovae*, A.W. Alsabti and P. Murdin, eds., p. 1671 (2017), DOI.

[81] C.L. Fryer and K.C.B. New, *Gravitational Waves from Gravitational Collapse*, *Living Reviews in Relativity* **6** (2003) 2 [`gr-qc/0206041`].

[82] N. Muhammed, M.D. Duez, P. Chawhan, N. Ghadiri, L.T. Buchman, F. Foucart et al., *Stability of hypermassive neutron stars with realistic rotation and entropy profiles*, Phys. Rev. D **110** (2024) 124063 [`2403.05642`].

[83] W. Kastaun and F. Galeazzi, *Properties of hypermassive neutron stars formed in mergers of spinning binaries*, Phys. Rev. D **91** (2015) 064027 [`1411.7975`].

[84] O. Gottlieb, *Jetted and Turbulent Stellar Deaths: New LIGO-Detectable Gravitational Wave Sources*, in *American Astronomical Society Meeting Abstracts*, vol. 242 of *American Astronomical Society Meeting Abstracts*, p. 211.03, June, 2023.

[85] S. Klimenko, I. Yakushin, A. Mercer and G. Mitselmakher, *A coherent method for detection of gravitational wave bursts*, *Classical and Quantum Gravity* **25** (2008) 114029 [`0802.3232`].

[86] S. Klimenko, G. Vedovato, M. Drago, F. Salemi, V. Tiwari, G.A. Prodi et al., *Method for detection and reconstruction of gravitational wave transients with networks of advanced detectors*, Phys. Rev. D **93** (2016) 042004 [`1511.05999`].

[87] M. Maggiore, *Gravitational wave experiments and early universe cosmology*, Phys. Rep. **331** (2000) 283 [`gr-qc/9909001`].

[88] N. Christensen, *Stochastic gravitational wave backgrounds*, *Reports on Progress in Physics* **82** (2019) 016903 [`1811.08797`].

[89] T. Regimbau, *The astrophysical gravitational wave stochastic background*, *Research in Astronomy and Astrophysics* **11** (2011) 369 [`1101.2762`].

[90] J.D. Romano and N.J. Cornish, *Detection methods for stochastic gravitational-wave backgrounds: a unified treatment*, *Living Reviews in Relativity* **20** (2017) 2 [`1608.06889`].

[91] G. Agazie, A. Anumarlapudi, A.M. Archibald, Z. Arzoumanian, P.T. Baker, B. Bécsy et al., *The NANOGrav 15 yr Data Set: Detector Characterization and Noise Budget*, ApJ **951** (2023) L10 [`2306.16218`].

[92] D.J. Reardon, A. Zic, R.M. Shannon, G.B. Hobbs, M. Bailes, V. Di Marco et al., *Search for an Isotropic Gravitational-wave Background with the Parkes Pulsar Timing Array*, ApJ **951** (2023) L6 [`2306.16215`].

[93] P. Cerda-Duran and N. Elias-Rosa, *Neutron Stars Formation and Core Collapse Supernovae*, in *Astrophysics and Space Science Library*, L. Rezzolla, P. Pizzochero, D.I. Jones, N. Rea and I. Vidaña, eds., vol. 457 of *Astrophysics and Space Science Library*, p. 1, Jan., 2018, DOI [1806.07267].

[94] T. Kuroda, T. Fischer, T. Takiwaki and K. Kotake, *Core-collapse Supernova Simulations and the Formation of Neutron Stars, Hybrid Stars, and Black Holes*, ApJ **924** (2022) 38 [2109.01508].

[95] J.M. Lattimer and M. Prakash, *The Physics of Neutron Stars*, Science **304** (2004) 536 [astro-ph/0405262].

[96] V. Kalogera and G. Baym, *The Maximum Mass of a Neutron Star*, ApJ **470** (1996) L61 [astro-ph/9608059].

[97] R.W. Romani, D. Kandel, A.V. Filippenko, T.G. Brink and W. Zheng, *PSR J0952-0607: The Fastest and Heaviest Known Galactic Neutron Star*, ApJ **934** (2022) L17 [2207.05124].

[98] K. Nomoto and S. Tsuruta, *Cooling of young neutron stars and Einstein X-ray observartions.*, ApJ **250** (1981) L19.

[99] K. Riles, *Searches for continuous-wave gravitational radiation*, Living Reviews in Relativity **26** (2023) 3 [2206.06447].

[100] D.L. Kaplan, *Nearby, Thermally Emitting Neutron Stars*, in *40 Years of Pulsars: Millisecond Pulsars, Magnetars and More*, C. Bassa, Z. Wang, A. Cumming and V.M. Kaspi, eds., vol. 983 of *American Institute of Physics Conference Series*, pp. 331–339, AIP, Feb., 2008, DOI.

[101] A. Lyne and F. Graham-Smith, *Pulsar Astronomy* (2012).

[102] G. Ushomirsky, C. Cutler and L. Bildsten, *Deformations of accreting neutron star crusts and gravitational wave emission*, MNRAS **319** (2000) 902 [astro-ph/0001136].

[103] C. Kittel, *Introduction to Solid State Physics*, Wiley, 8th ed. (2005).

[104] J.A. Morales and C.J. Horowitz, *Neutron star crust can support a large ellipticity*, MNRAS **517** (2022) 5610 [`2209.03222`].

[105] R.X. Xu, *Solid Quark Stars?*, ApJ **596** (2003) L59 [`astro-ph/0302165`].

[106] B.J. Owen, *Maximum Elastic Deformations of Compact Stars with Exotic Equations of State*, Phys. Rev. Lett. **95** (2005) 211101 [`astro-ph/0503399`].

[107] B. Haskell, N. Andersson, D.I. Jones and L. Samuelsson, *Are Neutron Stars with Crystalline Color-Superconducting Cores Relevant for the LIGO Experiment?*, Phys. Rev. Lett. **99** (2007) 231101 [`0708.2984`].

[108] N.K. Johnson-McDaniel and B.J. Owen, *Maximum elastic deformations of relativistic stars*, Phys. Rev. D **88** (2013) 044004 [`1208.5227`].

[109] H.T. Janka, K. Langanke, A. Marek, G. Martínez-Pinedo and B. Müller, *Theory of core-collapse supernovae*, Phys. Rep. **442** (2007) 38 [`astro-ph/0612072`].

[110] S. Bonazzola and E. Gourgoulhon, *Gravitational waves from pulsars: emission by the magnetic-field-induced distortion.*, A&A **312** (1996) 675 [`astro-ph/9602107`].

[111] A. Melatos and D.J.B. Payne, *Gravitational Radiation from an Accreting Millisecond Pulsar with a Magnetically Confined Mountain*, ApJ **623** (2005) 1044 [`astro-ph/0503287`].

[112] S. Chandrasekhar, *Solutions of Two Problems in the Theory of Gravitational Radiation*, Phys. Rev. Lett. **24** (1970) 611.

[113] W. Unno, Y. Osaki, H. Ando and H. Shibahashi, *Nonradial oscillations of stars* (1979).

[114] L. Rezzolla, F.K. Lamb and S.L. Shapiro, *R-Mode Oscillations in Rotating Magnetic Neutron Stars*, ApJ **531** (2000) L139 [`astro-ph/9911188`].

[115] R.V. Wagoner, *Conditions for Steady Gravitational Radiation from Accreting Neutron Stars*, ApJ **578** (2002) L63 [`astro-ph/0207589`].

[116] N. Andersson and K.D. Kokkotas, *The R-Mode Instability in Rotating Neutron Stars*, *International Journal of Modern Physics D* **10** (2001) 381 [`gr-qc/0010102`].

[117] B.J. Owen, *How to adapt broad-band gravitational-wave searches for r-modes*, Phys. Rev. D **82** (2010) 104002 [`1006.1994`].

[118] D.I. Jones and N. Andersson, *Freely precessing neutron stars: model and observations*, MNRAS **324** (2001) 811 [`astro-ph/0011063`].

[119] M. Zimmermann and E. Szedenits, Jr., *Gravitational waves from rotating and precessing rigid bodies: Simple models and applications to pulsars*, Phys. Rev. D **20** (1979) 351.

[120] C. Van Den Broeck, *The gravitational wave spectrum of non-axisymmetric, freely precessing neutron stars*, *Classical and Quantum Gravity* **22** (2005) 1825 [`gr-qc/0411030`].

[121] K. Wette, *Searches for continuous gravitational waves from neutron stars: A twenty-year retrospective*, *Astroparticle Physics* **153** (2023) 102880 [`2305.07106`].

[122] R. Prix, *Gravitational Waves from Spinning Neutron Stars*, in *Astrophysics and Space Science Library*, W. Becker, ed., vol. 357 of *Astrophysics and Space Science Library*, p. 651, Jan., 2009, DOI.

[123] R. Abbott, T.D. Abbott, S. Abraham, F. Acernese, K. Ackley, A. Adams et al., *Diving below the Spin-down Limit: Constraints on Gravitational Waves from the Energetic Young Pulsar PSR J0537-6910*, ApJ **913** (2021) L27 [`2012.12926`].

[124] B.P. Abbott, R. Abbott, T.D. Abbott, S. Abraham, F. Acernese, K. Ackley et al., *Searches for Gravitational Waves from Known Pulsars at Two Harmonics in 2015-2017 LIGO Data*, ApJ **879** (2019) 10 [`1902.08507`].

[125] R. Abbott, T.D. Abbott, F. Acernese, K. Ackley, C. Adams, N. Adhikari et al., *Narrowband Searches for Continuous and Long-duration Transient Gravitational Waves from Known Pulsars in the LIGO-Virgo Third Observing Run*, ApJ **932** (2022) 133 [`2112.10990`].

[126] B.P. Abbott, R. Abbott, T.D. Abbott, S. Abraham, F. Acernese, K. Ackley et al., *Search for gravitational waves from Scorpius X-1 in the second Advanced LIGO observing run with an improved hidden Markov model*, Phys. Rev. D **100** (2019) 122002 [`1906.12040`].

[127] J.T. Whelan, R. Tenorio, J.K. Wofford, J.A. Clark, E.J. Daw, E. Goetz et al., *Search for Gravitational Waves from Scorpius X-1 in LIGO O3 Data with Corrected Orbital Ephemeris*, ApJ **949** (2023) 117 [2302.10338].

[128] Y. Zhang, M.A. Papa, B. Krishnan and A.L. Watts, *Search for Continuous Gravitational Waves from Scorpius X-1 in LIGO O2 Data*, ApJ **906** (2021) L14 [2011.04414].

[129] V. Dergachev, M.A. Papa, B. Steltner and H.-B. Eggenstein, *Loosely coherent search in LIGO O1 data for continuous gravitational waves from Terzan 5 and the Galactic Center*, Phys. Rev. D **99** (2019) 084048 [1903.02389].

[130] J. Ming, M.A. Papa, A. Singh, H.B. Eggenstein, S.J. Zhu, V. Dergachev et al., *Results from an Einstein@Home search for continuous gravitational waves from Cassiopeia A, Vela Jr., and G347.3*, Phys. Rev. D **100** (2019) 024063 [1903.09119].

[131] H. Middleton, P. Clearwater, A. Melatos and L. Dunn, *Search for gravitational waves from five low mass x-ray binaries in the second Advanced LIGO observing run with an improved hidden Markov model*, Phys. Rev. D **102** (2020) 023006 [2006.06907].

[132] M.A. Papa, J. Ming, E.V. Gotthelf, B. Allen, R. Prix, V. Dergachev et al., *Search for Continuous Gravitational Waves from the Central Compact Objects in Supernova Remnants Cassiopeia A, Vela Jr., and G347.3-0.5*, ApJ **897** (2020) 22 [2005.06544].

[133] R. Abbott, T.D. Abbott, S. Abraham, F. Acernese, K. Ackley, A. Adams et al., *Searches for Continuous Gravitational Waves from Young Supernova Remnants in the Early Third Observing Run of Advanced LIGO and Virgo*, ApJ **921** (2021) 80 [2105.11641].

[134] B.P. Abbott, R. Abbott, T.D. Abbott, S. Abraham, F. Acernese, K. Ackley et al., *All-sky search for continuous gravitational waves from isolated neutron stars using Advanced LIGO O2 data*, Phys. Rev. D **100** (2019) 024004 [1903.01901].

[135] R. Abbott, T.D. Abbott, S. Abraham, F. Acernese, K. Ackley, A. Adams et al., *All-sky search in early O3 LIGO data for continuous gravitational-wave signals from unknown neutron stars in binary systems*, Phys. Rev. D **103** (2021) 064017 [2012.12128].

[136] B. Steltner, M.A. Papa, H.B. Eggenstein, R. Prix, M. Bensch, B. Allen et al., *Deep Einstein@Home All-sky Search for Continuous Gravitational Waves in LIGO O3 Public Data*, ApJ **952** (2023) 55 [2303.04109].

[137] T.T. Nakamura and S. Deguchi, *Wave Optics in Gravitational Lensing*, Progress of Theoretical Physics Supplement **133** (1999) 137.

[138] M. Grespan and M. Biesiada, *Strong Gravitational Lensing of Gravitational Waves: A Review*, Universe **9** (2023) 200.

[139] A. Einstein, *Lens-Like Action of a Star by the Deviation of Light in the Gravitational Field*, Science **84** (1936) 506.

[140] B. Paczynski, *Gravitational Microlensing by the Galactic Halo*, ApJ **304** (1986) 1.

[141] P. Schneider, J. Ehlers and E.E. Falco, *Gravitational Lenses* (1992), 10.1007/978-3-662-03758-4.

[142] C.R. Keeton, *A Catalog of Mass Models for Gravitational Lensing*, arXiv e-prints (2001) astro [astro-ph/0102341].

[143] R. Narayan and M. Bartelmann, *Lectures on Gravitational Lensing*, arXiv e-prints (1996) astro [astro-ph/9606001].

[144] S. Mao and H.J. Witt, *Lensing by a singular isothermal sphere and a black hole*, MNRAS **420** (2012) 792 [1111.2429].

[145] E.L. Turner, J.P. Ostriker and J.R. Gott, III, *The statistics of gravitational lenses : the distributions of image angular separations and lens redshifts.*, ApJ **284** (1984) 1.

[146] L.V.E. Koopmans, T. Treu, A.S. Bolton, S. Burles and L.A. Moustakas, *The Sloan Lens ACS Survey. III. The Structure and Formation of Early-Type Galaxies and Their Evolution since z ~1*, ApJ **649** (2006) 599 [astro-ph/0601628].

[147] R. Kormann, P. Schneider and M. Bartelmann, *Isothermal elliptical gravitational lens models.*, A&A **284** (1994) 285.

[148] D. Walsh, R.F. Carswell and R.J. Weymann, *0957+561 A, B: twin quasistellar objects or gravitational lens?*, Nature **279** (1979) 381.

[149] R.J. Weymann, D. Latham, J.R.P. Angel, R.F. Green, J.W. Liebert, D.A. Turnshek et al., *The triple QSO PG1115 + 08: another probable gravitational lens*, Nature **285** (1980) 641.

[150] K. Haris, A.K. Mehta, S. Kumar, T. Venumadhav and P. Ajith, *Identifying strongly lensed gravitational wave signals from binary black hole mergers*, *arXiv e-prints* (2018) arXiv:1807.07062 [1807.07062].

[151] X. Liu, I. Magaña Hernandez and J. Creighton, *Identifying Strong Gravitational-wave Lensing during the Second Observing Run of Advanced LIGO and Advanced Virgo*, ApJ **908** (2021) 97 [2009.06539].

[152] J. Janquart, O.A. Hannuksela, K. Haris and C. Van Den Broeck, *GOLUM: A fast and precise methodology to search for, and analyze, strongly lensed gravitational-wave events*, *arXiv e-prints* (2022) arXiv:2203.06444 [2203.06444].

[153] S. Goyal, D. Harikrishnan, S.J. Kapadia and P. Ajith, *Rapid identification of strongly lensed gravitational-wave events with machine learning*, Phys. Rev. D **104** (2021) 124057 [2106.12466].

[154] S. Chatterji, L. Blackburn, G. Martin and E. Katsavounidis, *Multiresolution techniques for the detection of gravitational-wave bursts*, *Classical and Quantum Gravity* **21** (2004) S1809 [gr-qc/0412119].

[155] L.P. Singer and L.R. Price, *Rapid Bayesian position reconstruction for gravitational-wave transients*, Phys. Rev. D **93** (2016) 024013 [1508.03634].

[156] R. Abbott, T.D. Abbott, S. Abraham, F. Acernese, K. Ackley, A. Adams et al., *Search for Lensing Signatures in the Gravitational-Wave Observations from the First Half of LIGO–Virgo's Third Observing Run*, ApJ **923** (2021) 14 [2105.06384].

[157] L. Dai, B. Zackay, T. Venumadhav, J. Roulet and M. Zaldarriaga, *Search for Lensed Gravitational Waves Including Morse Phase Information: An Intriguing Candidate in O2*, *arXiv e-prints* (2020) arXiv:2007.12709 [2007.12709].

[158] K.K.Y. Ng, K.W.K. Wong, T. Broadhurst and T.G.F. Li, *Precise LIGO lensing rate predictions for binary black holes*, Phys. Rev. D **97** (2018) 023012 [1703.06319].

[159] O.A. Hannuksela, T.E. Collett, M. Çalışkan and T.G.F. Li, *Localizing merging black holes with sub-arcsecond precision using gravitational-wave lensing*, MNRAS **498** (2020) 3395 [2004.13811].

[160] K. Liao, S. Tian and X. Ding, *Probing compact dark matter with gravitational wave fringes detected by the Einstein Telescope*, MNRAS **495** (2020) 2002 [2001.07891].

[161] J. Urrutia and V. Vaskonen, *Lensing of gravitational waves as a probe of compact dark matter*, MNRAS **509** (2022) 1358 [2109.03213].

[162] S. Basak, A. Ganguly, K. Haris, S. Kapadia, A.K. Mehta and P. Ajith, *Constraints on Compact Dark Matter from Gravitational Wave Microlensing*, ApJ **926** (2022) L28 [2109.06456].

[163] G.P. Smith, M. Bianconi, M. Jauzac, J. Richard, A. Robertson, C.P.L. Berry et al., *Deep and rapid observations of strong-lensing galaxy clusters within the sky localization of GW170814*, MNRAS **485** (2019) 5180 [1805.07370].

[164] X.-L. Fan, K. Liao, M. Biesiada, A. Piórkowska-Kurpas and Z.-H. Zhu, *Speed of Gravitational Waves from Strongly Lensed Gravitational Waves and Electromagnetic Signals*, Phys. Rev. Lett. **118** (2017) 091102.

[165] J.M. Ezquiaga and M. Zumalacárregui, *Gravitational wave lensing beyond general relativity: Birefringence, echoes, and shadows*, Phys. Rev. D **102** (2020) 124048 [2009.12187].

[166] S. Goyal, K. Haris, A.K. Mehta and P. Ajith, *Testing the nature of gravitational-wave polarizations using strongly lensed signals*, Phys. Rev. D **103** (2021) 024038 [2008.07060].

[167] A.K. Meena, *Gravitational lensing of gravitational waves: prospects for probing intermediate-mass black holes in galaxy lenses with global minima image*, *Monthly Notices of the Royal Astronomical Society* **532** (2024) 3568.

[168] S.H.W. Leong, J. Janquart, A.K. Sharma, P. Martens, P. Ajith and O.A. Hannuksela, *Constraining Binary Mergers in Active Galactic Nuclei Disks Using the Nonobservation of Lensed Gravitational Waves*, ApJ **979** (2025) L27 [2408.13144].

[169] R. Abbott, T.D. Abbott, S. Abraham, F. Acernese, K. Ackley, A. Adams et al., *Search for Lensing Signatures in the Gravitational-Wave Observations from the First Half of LIGO–Virgo's Third Observing Run*, ApJ **923** (2021) 14 [2105.06384].

[170] R. Massey, T. Kitching and J. Richard, *The dark matter of gravitational lensing*, *Reports on Progress in Physics* **73** (2010) 086901 [1001.1739].

[171] M. Bartelmann, *TOPICAL REVIEW Gravitational lensing*, *Classical and Quantum Gravity* **27** (2010) 233001 [1010.3829].

[172] S. Refsdal, *On the possibility of determining Hubble's parameter and the masses of galaxies from the gravitational lens effect*, MNRAS **128** (1964) 307.

[173] K.C. Wong, S.H. Suyu, G.C.F. Chen, C.E. Rusu, M. Millon, D. Sluse et al., *H0LiCOW - XIII. A 2.4 per cent measurement of H_0 from lensed quasars: 5.3σ tension between early- and late-Universe probes*, *Monthly Notices of the Royal Astronomical Society* **498** (2020) 1420 [1907.04869].

[174] S.G. Turyshev and V.T. Toth, *Recovering the mass distribution of an extended gravitational lens*, MNRAS **513** (2022) 5355 [2108.07172].

[175] J.-P. Kneib and P. Natarajan, *Cluster lenses*, A&A Rev. **19** (2011) 47 [1202.0185].

[176] T.E. Collett, L.J. Oldham, R.J. Smith, M.W. Auger, K.B. Westfall, D. Bacon et al., *A precise extragalactic test of General Relativity*, *Science* **360** (2018) 1342 [1806.08300].

[177] H.C. Ohanian, *On the focusing of gravitational radiation*, *International Journal of Theoretical Physics* **9** (1974) 425.

[178] S. Deguchi and W.D. Watson, *Wave effects in gravitational lensing of electromagnetic radiation*, Phys. Rev. D **34** (1986) 1708.

[179] Y. Wang, A. Stebbins and E.L. Turner, *Gravitational Lensing of Gravitational Waves from Merging Neutron Star Binaries*, Phys. Rev. Lett. **77** (1996) 2875 [astro-ph/9605140].

[180] M. Maggiore, C. Van Den Broeck, N. Bartolo, E. Belgacem, D. Bertacca, M.A. Bizouard et al., *Science case for the Einstein telescope*, J. Cosmology Astropart. Phys. **2020** (2020) 050 [1912.02622].

[181] T. Liu, M. Biesiada, S. Tian and K. Liao, *Robust test of general relativity at the galactic scales by combining strong lensing systems and gravitational wave standard sirens*, Phys. Rev. D **109** (2024) 084074 [2404.05907].

[182] X.-L. Fan, K. Liao, M. Biesiada, A. Piórkowska-Kurpas and Z.-H. Zhu, *Speed of Gravitational Waves from Strongly Lensed Gravitational Waves and Electromagnetic Signals*, Phys. Rev. Lett. **118** (2017) 091102.

[183] J.M. Ezquiaga and M. Zumalacárregui, *Gravitational wave lensing beyond general relativity: Birefringence, echoes, and shadows*, Phys. Rev. D **102** (2020) 124048 [2009.12187].

[184] T. Baker and M. Trodden, *Multimessenger time delays from lensed gravitational waves*, Phys. Rev. D **95** (2017) 063512 [1612.02004].

[185] M. Sereno, P. Jetzer, A. Sesana and M. Volonteri, *Cosmography with strong lensing of LISA gravitational wave sources*, MNRAS **415** (2011) 2773 [1104.1977].

[186] K. Liao, X.-L. Fan, X. Ding, M. Biesiada and Z.-H. Zhu, *Precision cosmology from future lensed gravitational wave and electromagnetic signals*, Nature Communications **8** (2017) 1148 [1703.04151].

[187] S. Jana, S.J. Kapadia, T. Venumadhav and P. Ajith, *Cosmography Using Strongly Lensed Gravitational Waves from Binary Black Holes*, Phys. Rev. Lett. **130** (2023) 261401 [2211.12212].

[188] B. Balick and R.L. Brown, *Intense sub-arcsecond structure in the galactic center.*, ApJ **194** (1974) 265.

[189] R. Schödel, T. Ott, R. Genzel, R. Hofmann, M. Lehnert, A. Eckart et al., *A star in a 15.2-year orbit around the supermassive black hole at the centre of the Milky Way*, Nature **419** (2002) 694 [astro-ph/0210426].

[190] A.M. Ghez, G. Duchêne, K. Matthews, S.D. Hornstein, A. Tanner, J. Larkin et al., *The First Measurement of Spectral Lines in a Short-Period Star Bound to the Galaxy's Central Black Hole: A Paradox of Youth*, ApJ **586** (2003) L127 [astro-ph/0302299].

[191] GRAVITY Collaboration, R. Abuter, A. Amorim, M. Bauböck, J.P. Berger, H. Bonnet et al., *Detection of the Schwarzschild precession in the orbit of the star S2 near the Galactic centre massive black hole*, A&A **636** (2020) L5 [2004.07187].

[192] Event Horizon Telescope Collaboration, K. Akiyama, A. Alberdi, W. Alef, J.C. Algaba, R. Anantua et al., *First Sagittarius A* Event Horizon Telescope Results. I. The Shadow of the Supermassive Black Hole in the Center of the Milky Way*, ApJ **930** (2022) L12.

[193] A. Treves, R. Turolla, S. Zane and M. Colpi, *Isolated Neutron Stars: Accretors and Coolers*, PASP **112** (2000) 297 [astro-ph/9911430].

[194] M. Evans, R.X. Adhikari, C. Afle, S.W. Ballmer, S. Biscoveanu, S. Borhanian et al., *A Horizon Study for Cosmic Explorer: Science, Observatories, and Community*, arXiv e-prints (2021) arXiv:2109.09882 [2109.09882].

[195] R. Abbott, H. Abe, F. Acernese, K. Ackley, N. Adhikari, R.X. Adhikari et al., *Search for continuous gravitational wave emission from the Milky Way center in O3 LIGO-Virgo data*, Phys. Rev. D **106** (2022) 042003 [2204.04523].

[196] J. Aasi, J. Abadie, B.P. Abbott, R. Abbott, T. Abbott, M.R. Abernathy et al., *Directed search for continuous gravitational waves from the Galactic center*, Phys. Rev. D **88** (2013) 102002 [`1309.6221`].

[197] S. Dodelson, *Gravitational Lensing* (2017).

[198] N. Andersson, *Gravitational-Wave Astronomy: Exploring the Dark Side of the Universe* (2019), 10.1093/oso/9780198568032.001.0001/oso-9780198568032.

[199] B.P. Abbott, R. Abbott, T.D. Abbott, M.R. Abernathy, F. Acernese, K. Ackley et al., *Prospects for observing and localizing gravitational-wave transients with Advanced LIGO, Advanced Virgo and KAGRA*, *Living Reviews in Relativity* **21** (2018) 3 [`1304.0670`].

[200] PyCBC, *PyCBC PSD package*, 2022.

[201] K. Liao, M. Biesiada and X.-L. Fan, *The Wave Nature of Continuous Gravitational Waves from Microlensing*, ApJ **875** (2019) 139 [`1903.06612`].

[202] A.G. Suvorov, *Wave-optical Effects in the Microlensing of Continuous Gravitational Waves by Star Clusters*, ApJ **930** (2022) 13 [`2112.01670`].

[203] P. Marchant, K. Breivik, C.P.L. Berry, I. Mandel and S.L. Larson, *Eclipses of continuous gravitational waves as a probe of stellar structure*, Phys. Rev. D **101** (2020) 024039 [`1912.04268`].

[204] J.M. Cordes and T.J.W. Lazio, *Finding Radio Pulsars in and beyond the Galactic Center*, ApJ **475** (1997) 557 [`astro-ph/9608028`].

[205] J.A. Kennea, D.N. Burrows, C. Kouveliotou, D.M. Palmer, E. Göğüş, Y. Kaneko et al., *Swift Discovery of a New Soft Gamma Repeater, SGR J1745-29, near Sagittarius A**, ApJ **770** (2013) L24 [`1305.2128`].

[206] S.E. Gralla and A. Lupsasca, *Lensing by Kerr black holes*, Phys. Rev. D **101** (2020) 044031 [`1910.12873`].

[207] S.U. Islam and S.G. Ghosh, *Strong field gravitational lensing by hairy Kerr black holes*, Phys. Rev. D **103** (2021) 124052 [`2102.08289`].

[208] M. Veale, C.-P. Ma, J.E. Greene, J. Thomas, J.P. Blakeslee, J.L. Walsh et al., *The MASSIVE survey - VIII. Stellar velocity dispersion profiles and environmental dependence of early-type galaxies*, *Monthly Notices of the Royal Astronomical Society* **473** (2018) 5446 [1708.00870].

[209] K.M. Mogotsi and A.B. Romeo, *The stellar velocity dispersion in nearby spirals: radial profiles and correlations*, *Monthly Notices of the Royal Astronomical Society* (2019) .

[210] T. Ren, A. Kwa, M. Kaplinghat and H.-B. Yu, *Reconciling the diversity and uniformity of galactic rotation curves with self-interacting dark matter*, *Phys. Rev. X* **9** (2019) 031020.

[211] N. Bar, K. Blum and C. Sun, *Galactic rotation curves versus ultralight dark matter: A systematic comparison with sparc data*, *Phys. Rev. D* **105** (2022) 083015.

[212] G.O. Ludwig, *Galactic rotation curve and dark matter according to gravitomagnetism*, *European Physical Journal C* **81** (2021) 186.

[213] A.M. Ghez, S. Salim, N.N. Weinberg, J.R. Lu, T. Do, J.K. Dunn et al., *Measuring Distance and Properties of the Milky Way's Central Supermassive Black Hole with Stellar Orbits*, *The Astrophysical Journal* **689** (2008) 1044 [0808.2870].

[214] M. Pitkin, *CWInPy: A Python package for inference with continuous gravitational-wave signals from pulsars*, *Journal of Open Source Software* **7** (2022) 4568.

[215] G. Ashton et al., *BILBY: A user-friendly Bayesian inference library for gravitational-wave astronomy*, *Astrophys. J. Suppl.* **241** (2019) 27 [1811.02042].

[216] M. Pitkin, M. Isi, J. Veitch and G. Woan, *A nested sampling code for targeted searches for continuous gravitational waves from pulsars*, *arXiv e-prints* (2017) arXiv:1705.08978 [1705.08978].

[217] M. Vallisneri, *Use and abuse of the fisher information matrix in the assessment of gravitational-wave parameter-estimation prospects*, *Physical Review D* **77** (2008) .

[218] R. Prix, *Search for continuous gravitational waves: Metric of the multidetector F-statistic*, *Phys. Rev. D* **75** (2007) 023004.

[219] P.R. Brady, T. Creighton, C. Cutler and B.F. Schutz, *Searching for periodic sources with ligo*, *Phys. Rev. D* **57** (1998) 2101.

[220] Y. Hua, K. Wette, S.M. Scott and M.D. Pitkin, *Population synthesis and parameter estimation of neutron stars with continuous gravitational waves and third-generation detectors*, *Monthly Notices of the Royal Astronomical Society* **527** (2023) 10564–10574.

[221] S. Savastano, F. Vernizzi and M. Zumalacárregui, *Through the lens of sgr* a^**: Identifying and resolving strongly lensed continuous gravitational waves beyond the einstein radius*, *Phys. Rev. D* **109** (2024) 024064.

[222] S. Nampalliwar, S. Kumar, K. Jusufi, Q. Wu, M. Jamil and P. Salucci, *Modeling the Sgr A* Black Hole Immersed in a Dark Matter Spike*, *The Astrophysical Journal* **916** (2021) 116 [2103.12439].

[223] S. Suyamprakasam, S. Harikumar, P. Ciecielag, P. Figura, M. Bejger and M. Biesiada, *Microlensing of long-duration gravitational wave signals originating from galactic sources*, 2025.

[224] M. Ajello, A. Albert, W.B. Atwood et al., *Fermi-LAT Observations of High-Energy Gamma-Ray Emission toward the Galactic Center*, *The Astrophysical Journal* **819** (2016) 44 [1511.02938].

[225] M. Di Mauro, *Characteristics of the Galactic Center excess measured with 11 years of Fermi-LAT data*, *Phys. Rev. D.* **103** (2021) 063029 [2101.04694].

[226] HESS Collaboration, A. Abramowski, F. Aharonian et al., *Acceleration of petaelectronvolt protons in the Galactic Centre*, *Nature* **531** (2016) 476 [1603.07730].

[227] A. Albert, B. Anderson, K. Bechtol et al., *Searching for Dark Matter Annihilation in Recently Discovered Milky Way Satellites with Fermi-Lat*, *The Astrophysical Journal* **834** (2017) 110 [1611.03184].

[228] R. Bartels, S. Krishnamurthy and C. Weniger, *Strong Support for the Millisecond Pulsar Origin of the Galactic Center GeV Excess*, *Phys. Rev. Lett.* **116** (2016) 051102 [`1506.05104`].

[229] J.F. Navarro, C.S. Frenk and S.D.M. White, *A Universal Density Profile from Hierarchical Clustering*, ApJ **490** (1997) 493 [`astro-ph/9611107`].

[230] M. Karamazov and D. Heyrovský, *Gravitational Lensing by a Massive Object in a Dark Matter Halo. II. Shear, Phase, and Image Geometry*, ApJ **927** (2022) 101 [`2109.02495`].

[231] G. Pagliaro, M.A. Papa, J. Ming, J. Lian, D. Tsuna, C. Maraston et al., *Continuous Gravitational Waves from Galactic Neutron Stars: Demography, Detectability, and Prospects*, ApJ **952** (2023) 123 [`2303.04714`].

[232] G. Woan, M.D. Pitkin, B. Haskell, D.I. Jones and P.D. Lasky, *Evidence for a Minimum Ellipticity in Millisecond Pulsars*, ApJ **863** (2018) L40 [`1806.02822`].